Measurement of the W Boson Helicity Fractions in $t\bar{t}$ Events at 8 TeV in the Lepton + Jets Channel with the ATLAS Detector

Dissertation

zur Erlangung des mathematisch-naturwissenschaftlichen Doktorgrades
"Doctor rerum naturalium"
der Georg-August-Universität Göttingen

im Promotionsprogramm ProPhys
der Georg-August University School of Science (GAUSS)

vorgelegt von

Mohammad Jawad Kareem

aus Karbala, IRAK

Göttingen, 2017

Betreuungsausschuss

Prof. Dr. Arnulf Quadt
II. Physikalisches Institut, Georg-August-Universität Göttingen

Prof. Dr. Ariane Frey
II. Physikalisches Institut, Georg-August-Universität Göttingen

Prof. Dr. Kevin Kröninger
Lehrstuhl für Experimentelle Physik IV, Technische Universität Dortmund

Mitglieder der Prüfungskommission:

Referent:	Prof. Dr. Arnulf Quadt II. Physikalisches Institut, Georg-August-Universität Göttingen
Koreferentin:	Prof. Dr. Stanley Lai II. Physikalisches Institut, Georg-August-Universität Göttingen

Weitere Mitglieder der Prüfungskommission:

Prof. Dr. Ariane Frey
II. Physikalisches Institut, Georg-August-Universität Göttingen

Prof. Dr. Hans Christian Hofsäss
II. Physikalisches Institut, Georg-August-Universität Göttingen

Prof. Dr. Karl-Henning Rehren
Institut für Theoretische Physik, Georg-August-Universität Göttingen

Jun. Prof. Dr. Steffen Schumann
II. Physikalisches Institut, Georg-August-Universität Göttingen

Tag der mündlichen Prüfung: 20.04.2017

Referenz: II.Physik-UniGö-Diss-2017/01

Measurement of the W boson Helicity Fractions in $t\bar{t}$ Events at 8 TeV in the Lepton+Jets Channel with the ATLAS Detector

Abstract

Precise measurements of the properties of the top quark allow for testing the Standard Model (SM) and can be used to constrain new physics models. The top quark is predicted in the SM to decay almost exclusively to a W boson and b-quark. Thus, studying the Wtb vertex structure at high precision and in detail is motivated.

This thesis presents a measurement of the W boson helicity fractions in top quark decays with $t\bar{t}$ events in the lepton + jets final state using proton-proton collisions at a centre-of-mass energy of $\sqrt{s} = 8$ TeV recorded in 2012 with the ATLAS detector at the LHC. The data sample corresponds to an integrated luminosity of 20.2 fb^{-1}. The angular distribution of two different analysers, the charged lepton and the down-type quark in the W boson rest frame are used to measure the helicity fractions. The most precise measurement is obtained from the leptonic analyser and events which contain at least two b-quark tagged jets. The results of

$$F_0 = 0.709 \pm 0.012 \text{ (stat.+bkg. norm.) } {}^{+0.015}_{-0.014} \text{ (syst.)},$$
$$F_L = 0.299 \pm 0.008 \text{ (stat.+bkg. norm.) } {}^{+0.013}_{-0.012} \text{ (syst.)},$$
$$F_R = -0.008 \pm 0.006 \text{ (stat.+bkg. norm.) } \pm 0.012 \text{ (syst.)},$$

which stand for longitudinal, left- and right-handed W boson helicity fractions respectively, are obtained by performing a combined fit of electron+jets and muon+jets channels to data. The measured helicity fractions are consistent with the Standard Model prediction. As the polarisation state of the W boson in top quark decays is sensitive to the Wtb vertex structure, limits on anomalous Wtb couplings are set.

Post address:
Friedrich-Hund-Platz 1
37077 Göttingen
Germany

II. Physikalisches Institut
Georg-August-Universität Göttingen

April 2017

"Don't hate what you don't know,
for the greater part of knowledge consists of
what you don't know."

Imam Ali, *Nahj al-Balagha*

Contents

1 Preface

The questions such as “who are we?”, “Where do we come from?”, “Where, when, and how, did it all start?”, “And what is the point of it all (if any)?”, have endured since the onset of human consciousness. In order to find answers to these simple but fundamental questions, mankind uses different tools such as science and philosophy as primary sources of knowledge. Natural science as a branch of science that is concerned with describing, predicting and understanding the natural phenomena is based on experimental evidence. Particle physics is known as the fundamental science that creates a foundation for other natural sciences, since it is regarded as the study of the fundamental constituents of the universe and the interactions among them. It plays an essential role to shed light on our understanding of the universe by attempting to address some of those fundamental questions. In this context, the Standard Model (SM) of particle physics is known as the most successful theory ever made, where the vast majority of its predictions is in a good agreement with the experimental measurements. The complete SM took a long time to build; from the discovery of the electron in 1897 by J.J. Thomson [1] until the discovery of the final piece of the puzzle –the Higgs boson– in 2012 [2, 3] by the scientists at the Large Hadron Collider (LHC).

The SM formulation classifies the fundamental particles in groups of leptons and quarks as fermion particles and describes their interactions via the exchange of gauge bosons or force carrier particles. Gravitational, electromagnetic, strong and weak forces are the fundamental interactions that are also known as the four fundamental forces of nature that do not appear to be reducible to more basic interactions. The gravitational force is not formulated in the SM framework, but described by a continuous classical field. The other three forces are modelled by discrete quantum fields, and exhibit a measurable

force carrier as an elementary particle. Therefore, the current SM formulation groups them in one framework. The top quark with a world average mass of 173.34 ± 0.76 GeV [4], known as the heaviest particle predicted by the SM, is the main focus of the research in this thesis. It was discovered in 1995 by the CDF and DØ experiments at the Tevatron [5, 6].

In addition to its large mass close to the electroweak symmetry breaking scale, the top quark has an extremely short lifetime ($\sim 5 \times 10^{-25}$ seconds) preventing it from forming bound states with other quarks, transferring its properties to its decay products. Therefore, it is the only quark that can be studied as a *bare* quark. Having such unique features, measurements of the top quark properties can provide an important tool for testing of the electroweak sector of particle physics. Moreover, the high production rate of the top quarks at the LHC provides the opportunity to conduct precise measurements of the top quark properties. The top quark decays almost exclusively into a W boson and a b-quark, and thus studying the structure and properties of the Wtb vertex is of importance. The properties of the top quark decay vertex are determined by the structure of the weak interaction. In the SM this coupling has a $(V - A)$ structure, where A refers to the axial vector and V to the vector part of the weak coupling. The produced W boson as a product of the top quark decay, carries a polarisation which can be either left-handed, right-handed or longitudinal. The corresponding polarisation fractions also referred to as helicity fractions, are determined by the Wtb vertex structure and the masses of the involved particles. The SM prediction for the W boson helicity fractions at Next-to-Next-to-Leading-Order (NNLO) in QCD is $F_L = 0.311 \pm 0.005$, $F_0 = 0.687 \pm 0.005$, and $F_R = 0.0017 \pm 0.0001$ [7].

By measuring the W boson helicity fractions in top quark decay with high precision, the SM prediction can be tested, and new physics processes which potentially could modify the structure of the top quark decay vertex can be probed. These fractions can be accessed from the decay products of the top quark via the angular distribution of polarisation analysers, i.e. the angle between the momentum direction of the charged lepton (down-type quark) from the decay of the leptonic (hadronic) W boson and the reversed momentum direction of the b-quark from the decay of the top quark in the W boson rest frame. All measurements of the W boson helicity fractions from the ATLAS, CDF, CMS and DØ collaborations performed so far show agreement with the SM prediction within the uncertainties [8–12].

In this thesis, the W boson helicity fractions are measured in the single lepton decay channel of the top quark pair ($t\bar{t}$) events. The measurement is performed via a template

fit technique using angular distribution of the decay products of the reconstructed $t\bar{t}$ candidate events. The full 2012 ATLAS dataset corresponding to an integrated luminosity of 20.2 fb^{-1} of proton-proton (pp) collisions with a centre-of-mass energy of $\sqrt{s} = 8$ TeV is analysed. A kinematic likelihood fit is used to determine the best association of b-jets, light jets, and lepton candidates to the top quark and anti-quark decay hypotheses, considering the momentum imbalance as the presence of a neutrino originating from the leptonically decaying W boson. The analyses from D0 [13] and CMS [14] have performed indirect helicity measurements via the hadronic analyser to distinguish only between longitudinal fraction and right- or left-handed one. In addition to using the classical leptonic analyser, this research is the first attempt to distinguish all three fractions using the hadronic analyser, which is achieved by differentiating between the up-type and down-type quarks corresponding to the jets from the hadronic W boson decay.

The work of this thesis is organised as follows: Chapter 2 introduces the general framework of the Standard Model of particle physics with an emphasis on top quark physics, particularly the theoretical aspects of the top quark decay vertex and the W boson helicity fractions. The most important features of the experimental setup of the LHC machine and the ATLAS detector are briefly summarised in Chapter 3. The reconstruction and identification of physics objects used in this analysis (e.g. tracks, leptons and jets) and their performance are presented in Chapter 4, followed in Chapter 5 by the description of the dataset used for the measurement, Monte Carlo simulated and data-driven models of the signal and background processes. The event selection and reconstruction strategy is discussed in Chapter 6. In Chapter 7, the analysis strategy is introduced where the template fitting method is described in detail. Chapter 8 presents the measurement uncertainty studies where the different sources of systematic uncertainties are discussed. The results of measurement of the helicity fractions, as well as the constraints on the anomalous couplings are presented in Chapter 9. Finally, Chapter 10 concludes the thesis and presents an outlook towards the future measurements and studies about the structure of the Wtb vertex.

The natural units ($\hbar = \mathrm{c} = 1$) are used in this thesis, and masses, energies and momenta are expressed in the units of [eV].

2

Top Quark Physics in the Standard Model

The first section of this chapter presents a general overview of the current SM framework, where the particles and fundamental forces –the fundamental constituents of the universe– and the concept of gauge symmetry within the Quantum Field Theory (QFT) framework are briefly introduced. A short summary about shortcomings of the SM and the searches for new physics Beyond the Standard Model closes the section. More details about the SM can be found in References such as [15, 16]. The discussion in the second section is focused on the physics of the top quark and its properties where the structure of the top quark decay vertex –Wtb– and its impact on the polarisation states of the W boson as a top quark decay product is discussed in detail. The last section in this chapter briefly summarises the results of the previous measurements of the W boson helicity fractions performed by the ATLAS experiment as well as other experiments.

2.1. The Standard Model of Particle Physics

The Standard Model of particle physics was developed to explain how the basic building blocks of matter interact, governed by the fundamental forces. Our best understanding of how these fundamental particles and forces are related to each other is encapsulated in this theory. Developed in the early 1970s, the theory successfully explains almost all experimental results and precisely predicts a wide variety of phenomena. This well-tested physics theory is also known as the most successful theory of particle physics to date.

Depending on the interaction types, the SM classifies the half-integer spin particles –*fermions*– as the constituents of matter in groups of quarks and leptons, each with six types (flavours) forming three generations. These flavours are conventionally

parametrised with flavour *quantum numbers*. On the other hand, the forces are described by integer spin mediator particles –*gauge bosons*– that the interacting fermions exchange. Along with the Higgs boson whose field causes the other elementary particles to acquire their mass, these fermions and bosons are considered to be the building blocks of our universe. A summary table of all elementary particles of the SM and their basic properties is presented in Figure 2.1.

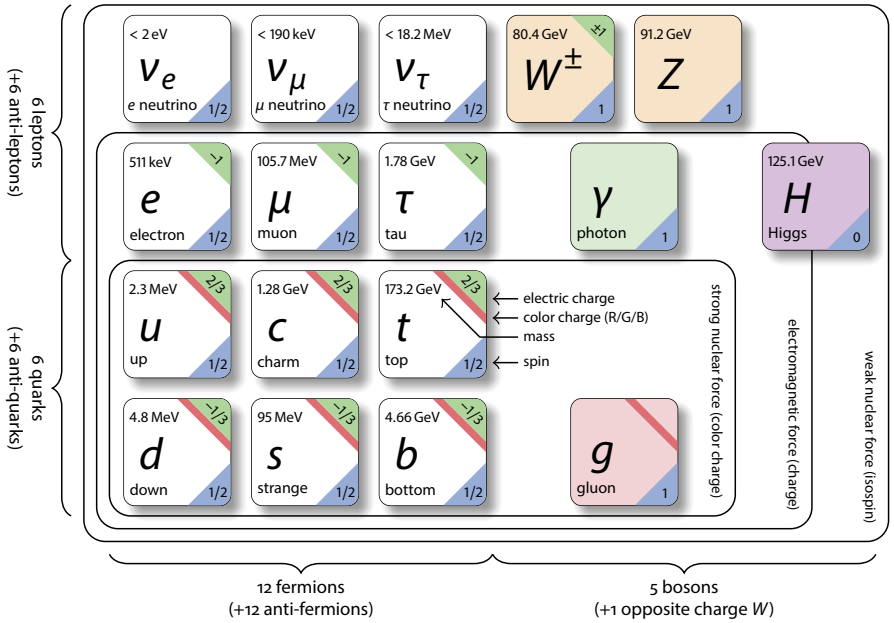

Figure 2.1.: The elementary particles of the Standard Model and some of their basic properties. Numbers are taken from [17].

Leptons consist of two main classes: charged leptons and neutral leptons. Each family (generation) is composed of one charged and one neutral lepton. The first generation is that of electronic leptons, comprising the electron (e^-) and electron neutrino (ν_e); the second is that of muonic leptons, comprising the muon (μ^-) and muon neutrino (ν_μ); and the third is that of tauonic leptons, comprising the tau (τ^-) and the tau neutrino (ν_τ). The higher the generation is, the heavier and more unstable is the lepton. Therefore the heavier leptons, i.e. muons and taus, decay rapidly into lower mass states and can only be produced in high energy collisions such as those involving cosmic rays and those produced in particle accelerators. Leptons do not participate in strong interaction, but they are subject to the other three fundamental interactions: gravitation, electromagnetism (excluding neutrinos, which are electrically neutral), and the weak interaction.

Quarks form the other class of fermions. Unlike leptons, quarks possess *colour charge*, which causes them to engage in the strong interaction in addition to the other interactions. They are the only elementary particles in the SM to experience all four fundamental interactions. *Hadrons* are composite particles made of quarks. The most stable of those are protons and neutrons, the components of atomic nuclei that are made of the first generation quarks, i.e. the up and down quarks. Similar to leptons, the higher the generation level is, the heavier and more unstable is the quark. So the heavier quarks rapidly decay into the up and down quarks. Thus, up and down quarks are generally stable and the most common in the universe, whereas the second generation quarks, the charm and strange and the third generation quarks, the bottom and top quarks can only be produced in high energy collisions. The heavier the particle is, the higher energy of the collision is required to recreate it in the accelerator. The existence of the top quark was foreseen to complete the third generation of quarks as a partner for the b-quark. However, it was only in 1995 at the Tevatron, that the top quark was discovered.

In addition to the formerly described particles, for every particle in the SM, there is a corresponding antiparticle related to the particle by *charge conjugation* that includes more than just electric charge; it inverts all internal quantum numbers such as baryon number, lepton number, etc. The flavour quantum numbers are additive. Hence an antiparticle has flavour equal in magnitude to the particle but opposite in sign. In modern physics, the concept of antiparticle was raised in 1928 by Paul Dirac [18] when the solution of his relativistic version of the Schrödinger wave equation for electrons led to negative energy quantum states. Later in 1932 the antiparticle of the electron -the positron- was discovered by Carl D. Anderson [19] as the first evidence of an antiparticle.

The Standard Model is a quantum field theory, composed of the following fields:

- The fermion field, ψ, which account for matter particles,
- The electroweak boson fields, W_1, W_2, W_3 and B,
- The gluon field, G_a,
- The Higgs field, ϕ.

In addition, the SM is a gauge theory of the symmetry group $SU(3) \otimes SU(2) \otimes U(1)$, where $U(1)$ acts on B and ϕ, $SU(2)$ acts on W and ϕ, and $SU(3)$ acts on G. The *Higgs Mechanism* (see Section 2.1.1) mixes the electroweak massless boson fields W_1, W_2, W_3

and B, creating the following physical observables:

$$\begin{pmatrix} A \\ Z \end{pmatrix} = \begin{pmatrix} \cos\theta_W & \sin\theta_W \\ -\sin\theta_W & \cos\theta_W \end{pmatrix} \times \begin{pmatrix} B \\ W_3 \end{pmatrix}, \tag{2.1}$$

$$W^{\pm} = \frac{1}{\sqrt{2}}(W_1 \mp iW_2), \tag{2.2}$$

where θ_W is the experimentally determined "*weak mixing angle*". A is the massless linear combination (the *photon*) corresponding to the electromagnetic interaction, Z is the orthogonal massive combination (the Z^0) representing the neutral weak interaction, while the combination of the charged states, W_1 and W_2 represent the $W^{\pm}$ particles, corresponding to the charged weak interaction.

The strength of the interaction in the SM is determined by the coupling constant or the gauge coupling parameter. E.g. the electromagnetic coupling constant in terms of the fine-structure constant (α) would be $g_e = \sqrt{4\pi\alpha}$ which is proportional to the fermion bare electric charge. By taking the momentum transferred in collision q into account, one could define an effective charge as a function of q^2 which introduces the concept of the "running coupling constant".

2.1.1. Electroweak Interaction

The electroweak interaction in the SM is the unified description of the electromagnetism and the weak interaction, governed by the $SU(2)_L \otimes U(1)_Y$ symmetry group, where Y refers to the "*weak hypercharge*", the generator of the $U(1)_Y$ and L indicates that the vector bosons (W_1, W_2, W_3) described by $SU(2)$ symmetry group only couple to the left-handed chiral component of the fermions. Although these two interactions appear very different at low energies, the Glashow, Weinberg and Salam (GWS) Model [20–22], formulated them as two different aspects of the same interaction. To understand the methodology of this unification, it is necessary at first to understand the characteristics of each symmetry group separately.

Electromagnetic Interaction

The electromagnetic interaction is mediated by the massless *photon* and is governed by the $U(1)$ gauge symmetry, formulated by the Quantum Electrodynamics (QED) framework of QFT.

For spin-1 fields, one can define the field strength tensor as:

$$F^a_{\mu\nu} = \partial_\mu A^a_\nu - \partial_\nu A^a_\mu + g f^{abc} A^b_\mu A^c_\nu, \tag{2.3}$$

for a gauge field A with coupling constant g. The structure constant, f^{abc} is defined by the commutator $[t_a, t_b] = i f^{abc} t_c$, where t_i are the group generators. For any *Abelian* (commutative) group such as $U(1)$, the structure constant term vanishes and consequently there would be no self-interacting term in the field *Lagrangian*. Therefore, there is no photon-photon interaction in the electromagnetic sector. The gauge self-interaction term (the last term of Equation 2.3) explains the running coupling constant behaviour. It can be shown [16] that the coupling of the electromagnetic interaction increases for larger momentum transfers. The dependence of the coupling constant α to the energy scale in the high energy limit (large Q^2) is given by:

$$\alpha(Q^2) = \frac{\alpha(\mu^2)}{1 - \frac{\alpha(\mu^2)}{3\pi} ln(\frac{Q^2}{\mu^2})}, \tag{2.4}$$

where μ is the renormalisation scale. As seen in Equation 2.4, at high energy, $\alpha(Q^2)$ gets larger and eventually diverges, where perturbation theory is not valid in this regime anymore. However, this occurs at a very high energy scale for QED.

Weak Interaction

In the Standard Model of particle physics, the weak interactions are mediated by the exchange of the massive W and Z bosons. All known fermions interact through the weak interactions. Weak interactions are feeble not because of the coupling constant (which in fact it is nearly five times larger than of the electromagnetic one), but because the mediators are so massive. All particles have a property called weak-isospin T_3, which serves as a quantum number and describes how that particle behaves in the weak interaction. The left-handed fermions have weak-isospin of $T = 1/2$, grouped into doublets with $T_3 = \pm 1/2$ (the third component of T). All particles with same T_3 quantum number behave in a similar way under the weak interaction, e.g. under the charged weak current the up-type quarks (u,c,t) with $T_3 = +1/2$ transform into down-type quarks (d, s, b) with $T_3 = -1/2$ and vice versa, but never decay into a quark with same T_3. This is also true for the left-handed leptons, where the charged leptons with $T_3 = +1/2$ are the doublet partner of their corresponding neutrinos with $T_3 = -1/2$. In this context, the

weak interaction is known as being responsible for radioactive β decay, where e.g. in β^- radiation, a down quark within a neutron is changed into an up quark, converting the neutron to a proton and resulting in the emission of an electron and an electron antineutrino. On the other hand, the right-handed fermions form singlets rather than doublet (have $T = 0$) and do not undergo charged weak interactions involving $W^{\pm}$.

The probability of a transition from one quark i to another quark j (with opposite T_3) under the weak interaction is given by the unitary Cabibbo-Kobayashi-Maskawa (CKM) matrix [23, 24] as:

$$\begin{pmatrix} d' \\ s' \\ b' \end{pmatrix} = \begin{pmatrix} V_{ud} & V_{us} & V_{ub} \\ V_{cd} & V_{cs} & V_{cb} \\ V_{td} & V_{ts} & V_{tb} \end{pmatrix} \begin{pmatrix} d \\ s \\ b \end{pmatrix}. \tag{2.5}$$

Thus, the weak interaction not only changes the quark flavour within each weak-isospin doublet but also across all generations.

Particle transformations or decays via the weak interactions typically occur much slower than the processes involving electromagnetic or strong interactions, i.e. because the large mass-energy of these massive weak force mediators must be borrowed within the Heisenberg time limit for virtual particles, processes mediated by these mediators are both very short range and very slow – particles have to wait a (relatively) long time for such a large amount of energy to become available as a quantum fluctuation within the Heisenberg temporal bounds. Therefore, these type of interactions have relatively smaller phase space. This can explain the dramatic difference between the lifetime of the neutral pion, 10^{-16} seconds, which decays electromagnetically with respect to the lifetime of the charged pion, 10^{-8} seconds, which decays through the weak interaction. Based on which force mediator is involved, the weak interactions are classified as the charged-current, mediated by $W^{\pm}$ or neutral-current interaction mediated by Z.

Another significant difference with respect to the other interactions is the parity violation in the weak interactions. A parity transformation (also called parity inversion) is the flip in the sign of the spatial coordinate system. The concept of the so-called law of *parity conservation* is that the mirror image of any physical process also represents a perfectly possible physical process, which is respected by the gravitational, electromagnetic and the strong interactions was thought to be a universal law. But the discovery in 1957 [25] showed that the weak interaction violates the parity. Later, Feynman and Gell-Mann [26] proposed that the charged weak interaction is of the form Vector – Axial

vector $(V-A)$, i.e. the coupling of quarks and leptons to $W^{\pm}$ is a universal form of

$$\frac{-ig_w}{2\sqrt{2}}\gamma^{\mu}(1-\gamma^5), \tag{2.6}$$

which is the coupling that governs the top quark decay vertex as well (see Section 2.2.2).

Electroweak Unification

The structural difference between the electromagnetic and weak formalism is that the former contains purely vectorial (γ^{μ}), whereas the latter contain vector and axial vector components, i.e. the $W^{\pm}$ coupling is "maximally" mixed V–A, $\gamma^{\mu}(1-\gamma^5)$ as mentioned earlier in this section, and consequently the weak interaction couples to left-handed particles but the electromagnetic interaction couples to both types. The mathematical trick to unify these two different looking formalisms is to convert the V–A to pure vectorial type which couples only to left-handed particles. The second issue toward the unification is that unlike the massless electromagnetic mediator, the weak mediators are so heavy, where the solution was provided by Weinberg and Salam in the form of the Higgs Mechanism.

Electroweak Spontaneous Symmetry Breaking and Higgs Mechanism

The gauge invariance property of the SM, which is an essential requirement for a renormalisable theory[1], implies massless gauge bosons and fermions, in contrast to the experimentally observed massive weak gauge bosons $W^{\pm}$ [27, 28] and Z [29, 30]. This issue is solved by introducing the *Higgs Mechanism* by three independent groups in 1964: by Brout and Englert [31], Higgs [32], and by Guralnik, Hagen and Kibble [33], which is able to explain mass generation without "breaking" gauge theory. As a consequence, a new field –the Higgs field, is added to the SM Lagrangian.

The Electroweak Spontaneous Symmetry Breaking (EWSSB) occurs when there are multiple ground states in the potential energy of the Lagrangian. According to the Feynman calculus which is a perturbation procedure, the field is treated as fluctuation around the ground state. To set up the Feynman formalism, one is obliged to select one of these ground states and reformulate the symmetric Lagrangian which is invariant in that field (ϕ) based on the selected ground state. That spoils the original symmetry, i.e.

[1] In a renormalisable theory, the cancellation of all infinities takes place among only a finite number of interactions.

the true symmetry of the system is concealed due to an arbitrary choice of a particular (asymmetrical) ground state.

A simple Higgs model composed of two complex scalar fields in the form of a weak-isospin doublet:

$$\phi = \begin{pmatrix} \phi^+ \\ \phi^0 \end{pmatrix} = \frac{1}{\sqrt{2}} \begin{pmatrix} \phi_1 + i\phi_2 \\ \phi_3 + i\phi_4 \end{pmatrix}, \tag{2.7}$$

where ϕ^+ and ϕ^0 are charged and neutral scalar fields. The corresponding Lagrangian with a potential energy function that could serve as a spontaneously broken continuous symmetry as shown in Figure 2.2, which also keeps renormalisability, can be written as

$$\mathscr{L}_{Higgs} = \frac{1}{2}(\partial_\mu \phi)^*(\partial^\mu \phi) - \mathscr{U}(\phi), \tag{2.8}$$

with a potential term (Higgs potential) of

$$\mathscr{U}(\phi) = -\mu^2(\phi^*\phi) + \lambda(\phi^*\phi)^2. \tag{2.9}$$

In the case of negative λ, then $\mathscr{U}(\phi)$ will not have any stable minima. Therefore, it is required to have $\lambda > 0$ to form a stable vacuum. For $\mu^2 < 0$, the potential energy ground states lie on a circle in the complex ϕ plane given by:

$$\phi^*\phi_{min} = -\frac{\mu^2}{2\lambda} = \frac{\nu^2}{2}, \tag{2.10}$$

where ν is defined as the vacuum expectation value of the Higgs field. As mentioned earlier, to follow the Feynman formalism, a particular ground state should be "chosen", which breaks the symmetry of the Lagrangian in Equation 2.8. To keep the photon massless the neutral scalar field is expanded around the chosen ground state. Thus, the weak-isospin doublet defined in Equation 2.7 can be rewritten as:

$$\phi = \frac{1}{\sqrt{2}} \begin{pmatrix} \phi_1 + i\phi_2 \\ \nu + h(x) + i\phi_4 \end{pmatrix}. \tag{2.11}$$

Substituting ϕ into the Higgs Lagrangian, extra unwanted fields with a massless particle, known as "Goldstone bosons" appear. To eliminate these particles and without loss

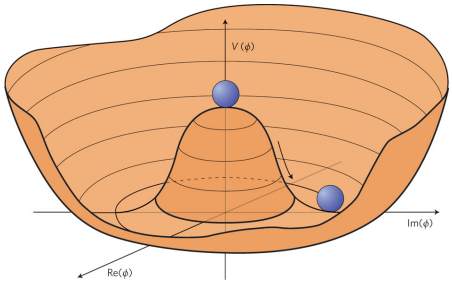

Figure 2.2.: The Higgs potential.

of generality, the ϕ doublet can be written in a unitary gauge as:

$$\phi = \frac{1}{\sqrt{2}} \begin{pmatrix} 0 \\ \nu + h(x) \end{pmatrix}, \tag{2.12}$$

and the mass terms of the Lagrangian correspond to the weak gauge bosons can be written in terms of the Higgs field vacuum expectation value as:

$$m_W = \frac{1}{2} g_2 \nu, \tag{2.13}$$

$$m_Z = \frac{1}{2} \nu \sqrt{g_1^2 + g_2^2}, \tag{2.14}$$

where g_1 and g_2 are the coupling strength of the $U(1)$ and $SU(2)$ symmetry groups respectively. Having g_2 and the W boson mass measured experimentally, the vacuum expectation value is determined to be $\nu = 246$ GeV. This gauge transformation has absorbed the extra degree of freedom from the Goldstone boson and transformed the massless vector field (with two degrees of freedom of transverse polarisations) to acquire a mass and a third polarisation state.

The Higgs mechanism as the result of spontaneous symmetry breaking in this local gauge-invariant condition is responsible for the mass of the weak interaction gauge bosons ($W^{\pm}$ and Z).

In addition, in the SM, the Higgs field is also responsible for the fermions to acquire masses proportional to the vacuum expectation value of the Higgs field as

$$m_f = \frac{y_f}{\sqrt{2}} \nu, \tag{2.15}$$

where y_f is known as "Yukawa coupling" of the fermions to the Higgs field.

2.1.2. Strong Interaction

The strong nuclear force or the strong interaction is mediated by the exchange of massless particles called *gluons* that act between quarks, antiquarks, and other gluons. Gluons are thought to interact with quarks and other gluons via a charge called "*colour charge*". Colour charge is analogous to electromagnetic charge, but it comes in three types ($\pm$ red, $\pm$ green, $\pm$ blue) rather than one, results in a different type of force, with different rules of behaviour. These rules are detailed in the theory of Quantum Chromodynamics (QCD), which is the theory of quark-gluon interactions.

Unlike QED, QCD is mathematically a non-Abelian gauge theory based on a local gauge symmetry group called $SU(3)$, and therefore the self-interacting term of the Lagrangian implies the existance of gluon-gluon interactions. However, the quark-gluon interaction which could be considered as the analogous QED lepton-photon interaction term has a similar effect on the strong coupling constant (increasing coupling strength in short distance or high energy), the additional ingredient has an opposite influence, resulting in a kind of competition between the quark and gluon polarisation diagrams. The winner in this competition depends on the number of flavours (f) and colours (n), where the critical parameter turns out to be $a \equiv 2f - 11n$ [15].

In the SM, $f = 6$ and $n = 3$, so $a = -21$, and the QCD coupling decreases in short distance (or in higher energies), which is known as "*asymptotic freedom*". In this regime quarks interact weakly enough that they can be considered as free particles inside the hadrons, which allows to perform perturbative calculations. On the other hand, as the distance increases (or in lower energies), another distinction between QED and QCD arises, which is that no free particle carrying colour charge, i.e. the quarks are confined in colourless bound states of two quarks (mesons) or three quarks (baryons). Thus, the "*colour confinement*" can be described qualitatively as the increase of the potential energy as the quarks are pulled further apart in a way that the applied energy for separation is enough to create a pair of quark-antiquark. Because of this phenomenon and in the case of enough initial energy, a spray of particles is produced, which is observed and classified as a *jet*. In Chapter 4, the experimental methods of jet identification are explained in detail. By applying similar arguments as those applied to QED and adding the gluon-

gluon self-interaction term, the analogous equation to Equation 2.4 results in:

$$\alpha_s(Q^2) = \frac{4\pi}{\beta_0 \ln(Q^2/\Lambda_{QCD})}, \tag{2.16}$$

where $\beta_0 = 11 - \frac{2}{3}n_f$ and Λ_{QCD} stands for the energy scale characterising the confinement of quarks in QCD with an experimentally measured value of ≈ 200 MeV [34].

As seen in this Equation (2.16), the coupling constant diverges in the low energy limit. On the other hand, at high Q^2 where the coupling constant of QCD becomes small, the perturbative methods become valid. Technically the separation of the long distance (low Q^2) from the short distance (high Q^2) is called "*factorisation*". This technique allows perturbative QCD (pQCD) and phenomenological methods to be applied to the high and low Q^2 components simultaneously.

2.1.3. The Standard Model Limitations and Search for New Physics

Despite being a successful theory of particle physics, the SM is not perfect. Failures of the SM could be classified in groups of phenomena and the experimental results that the SM cannot explain. The fundamental non-explained phenomena can be summarised as:

- Dark matter and dark energy: Cosmological observations[2] [35] indicate that the Standard Model explains only about 5% of the entire mass–energy of the observable universe. The rest is composed of about 26% *dark matter*, which would behave like ordinary matter, but interacts weakly[3] (if at all) with the SM fields, and (69%) *dark energy*, a constant energy density for the vacuum. Yet, the SM does not provide any fundamental particles that could be considered as dark matter candidates. Attempts to explain dark energy in terms of vacuum energy of the standard model results in a mismatch of more than 100 orders of magnitude [36].

- Matter-antimatter asymmetry: is the imbalance between the matter and antimatter in the observable universe. It is believed that the *Big-Bang* should have produced equal amounts of matter and antimatter. Therefore, there must be some physical laws that do not apply equally to matter and antimatter and allow the matter to be produced more commonly than antimatter in conditions immediately after the Big-Bang. These processes are known as charge-parity (CP) violating processes.

[2] Studies of motion of galaxies show that the total kinetic energy is much greater than of what explained via the visible matter. Also, galactic rotation curves, which illustrate the velocity of rotation versus the distance from the galactic centre, show the excess velocity.

[3] Known also as weakly interacting massive particles (*WIMPs*)

The predicted CP processes in the current version of the SM is too insignificant to be able to explain this huge asymmetry. Hence, most of the theoretical and experimental efforts in this sector involve a modification of the SM to allow the CP violating processes to explain the matter-antimatter asymmetry.

- Neutrino oscillations: predicted by Bruno Pontecorvo in 1957 [37] and observed by a multitude of experiments with different neutrino sources such as solar, atmospheric, reactor and beam (via particle accelerator) neutrino, the created neutrino with a specific flavour is measured later with a different flavour, where the probability of measuring a specific flavour varies periodically as it propagates through space. This phenomenon implies that the neutrino has a non-zero mass. The efforts to apply a modification to the SM to include a mass term lead to some other theoretical issues such as the question if neutrinos should be considered as *Dirac* or *Majorana* particles.

The SM also suffers from shortcomings such as not being able to accommodate the gravity. Currently, there is no known way of describing general relativity within quantum field theory.

The *hierarchy* problem is another unaddressed issue, whereby the mass of the Higgs boson acquire very large quantum corrections, thus the Higgs bare mass must be fine-tuned in a way that almost cancels these quantum corrections, which is not natural. There are also other types of hierarchy problems in the SM such as the fermion mass hierarchy and the hierarchy problem due to the large discrepancy between aspects of the weak and gravitational force, whereby the weak force is about 10^{32} times stronger than gravity.

Extensions to the Standard Model

The Supersymmetry (SUSY) could be considered as one of the most promising extensions of the SM. It adds another class of symmetries to the SM Lagrangian. Such a symmetry predicts the existence of supersymmetric particles (*s–particles*). Each particle in the SM would have a *superpartner* whose spin differs by 1/2 from the ordinary particle, i.e. for each fermion (boson) of the SM there is a boson (fermion) superpartner, which is predicted to be much heavier than its ordinary partner that the available collision energy of the current particle colliders may not be enough to create them. These superpartners would allow the unification of the electroweak and the strong interaction at a certain energy scale. In addition, this model provides a dark matter candidate, called *neutralino*.

In a theory with perfectly "unbroken" supersymmetry, each pair of superpartners would have the same mass as the ordinary particle. Thus, since no superpartners have been observed, if supersymmetry exists, the symmetry must be spontaneously broken and the superpartners got different mass. The simplest formalism of spontaneously broken supersymmetry is the so-called Minimal Supersymmetric Standard Model (MSSM), which is one of the best-studied candidates for physics beyond the Standard Model [38].

2.2. Top Quark Physics

After the discovery of the b-quark in 1977 by the CDF and DØ experiments at Fermilab as the first observed quark of the third generation, searches started in order to find its weak-isospin partner with charge $Q = +2/3$ and $T_3 = +1/2$. Being unexpectedly heavy, it was only in 1995 when the CDF and DØ experiments announced its discovery [5, 6]. The top quark is known as the heaviest particle in the SM. At the LHC, the top quark is produced in pairs through the strong interaction and individually through electroweak processes via proton-proton collisions.

With a current world average mass[4] of 173.34 ± 0.76 GeV [4] close to the electroweak symmetry breaking scale, it is the only quark that can decay into a real W boson and b-quark. Equation 2.15 predicts the top quark Yukawa coupling to the Higgs boson to be close to unity. Precise measurements of the top quark properties (mass, width, production cross section, decay branching ratios, spin polarisation, couplings, etc.) can provide an important tool in terms of tests of the SM.

2.2.1. Top Quark Production

At the LHC, top quarks are produced dominantly in pairs through the strong interaction via quark-antiquark annihilation (Figure 2.3a) and gluon-gluon fusion (Figures 2.3b and 2.3c). Due to the asymptotic freedom, the hadron constituent (partons), are effectively free particles inside the hadron. Therefore, the high energy hadron-hadron collisions are effectively collisions between the proton constituents, i.e. quarks and gluons, each carrying a certain fraction x of the initial momenta of the initial hadron.

[4]The average result from the ATLAS, CDF, CMS and DØ measurements

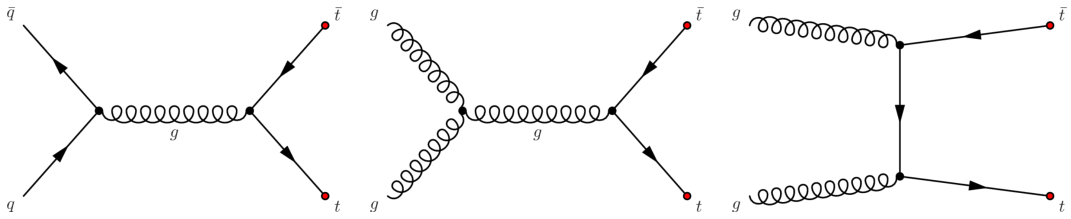

Figure 2.3.: Top quark pair production via the strong interaction through (a): quark anti-quark annihilation, and (b)-(c): gluon-gluon fusion.

Top Quark Pair Production

The QCD factorisation theorem [39] separates the inclusive cross section of the $t\bar{t}$ production into two parts: short-distance effect corresponds to partonic (hard scattering) cross section ($\hat{\sigma}$), which is calculable using perturbative QCD, and long-distance effect corresponds to the probability for finding a parton with a certain longitudinal momentum fraction x_i of the initial hadron momentum at factorisation scale μ_F inside the hadron, ($f(x, \mu_F)$). The latter quantity which is also known as the *Probability Density Function* (PDF) can not be predicted by the QCD and must be measured experimentally. Its evolution is governed by the *DGLAP* evolution equation [40–42], i.e. given the distribution in the initial energy scale μ_0^2, the equation predicts the distribution at the final energy scale μ^2. Figures 2.4a and 2.4b show the PDF distributions for the CT10 PDF set [43] at $\mu_F^2 = 10$ GeV^2 and 100 GeV^2, respectively.

The inclusive cross section for $t\bar{t}$ production at centre-of-mass energy $\sqrt{s}$ can be therefore expressed as:

$$\sigma_{q\bar{q}\to t\bar{t}}(s, m_t^2) = \sum_{i,j} \int dx_1 dx_2 f_i(x_1, \mu_F^2) f_j(x_2, \mu_F^2) \hat{\sigma}_{ij\to t\bar{t}}(\hat{s}, m_t^2, \mu_F^2, \mu_R^2), \tag{2.17}$$

where $\hat{s} = x_i x_j s$ is the effective centre-of-mass energy of the parton-parton collision. For $t\bar{t}$ production it is required that $\hat{s} \geq 4m_t^2$.

Unlike top quark pair production via $p\bar{p}$ collisions at the Tevatron where $\simeq 85\%$ is produced via the quark-antiquark annihilation process due to the dominant valence quark PDFs at $\sqrt{s} = 1.96$ TeV, in pp collisions at the LHC, where the antiquarks are only available as sea quarks, gluon-gluon fusion production mechanism is dominant by $\simeq 80\%$

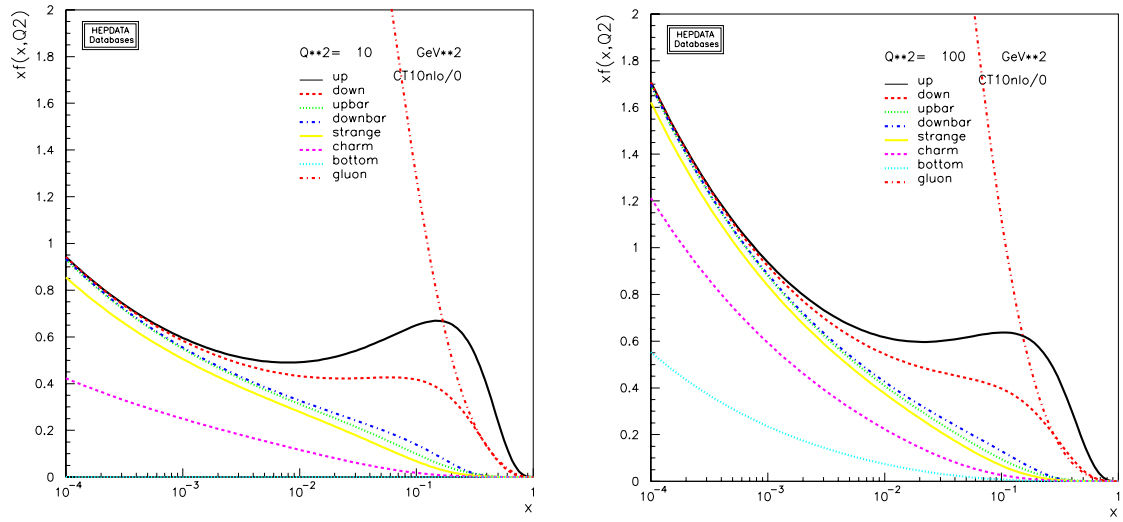

(a) (b)

Figure 2.4.: The Q^2 dependence of the $xf(x, Q^2)$ as given by the CT10 PDF set [43] at Q^2=10 GeV^2 (left) and Q^2=100 GeV^2 (right)

at $\sqrt{s} = 7 - 8$ TeV.

The theoretical calculation of the top quark pair production cross section performed at NNLO in QCD including resummation of Next-to-Next-to-Leading-Logarithmic (NNLL) soft gluon terms for pp collisions at centre-of-mass energy $\sqrt{s} = 8$ TeV assuming $\mu_F = \mu_R = m_t = 172.5$ GeV and using the CT10 PDF set [44–49], and yields a $t\bar{t}$ cross section of:

$$\sigma_{t\bar{t}}^{NNLO+NNLL} = 252.89\ ^{+6.39}_{-8.64}(\text{scale})\ ^{+7.58}_{-7.33}(m_t) \pm 11.67\ (\text{PDF} + \alpha_s)\ \text{pb}.$$

The uncertainty of the theoretical calculation is due to the uncertainties of the input parameters. The scale uncertainty is derived by considering a factor of 2 and 0.5 of the nominal value. The uncertainty due to the assumed top quark mass is evaluated by varying the mass by ±1 GeV. The PDF and α_s uncertainty is calculated using three different PDF sets (CT10 NNLO, MSTW2008 68% CL NNLO [50, 51] and NNPDF2.3 5f FFN [52]).

At the LHC, the combined ATLAS and CMS $t\bar{t}$ cross section measurement at the centre-of-mass energy $\sqrt{s} = 8$ TeV [53] yields:

$$\sigma_{t\bar{t}}^{meas.} = 241.5 \pm 1.4\ (\text{stat.}) \pm 5.7\ (\text{syst.}) \pm 6.2\ (\text{lumi.})\ \text{pb},$$

where the obtained experimental precision is better than the theoretical calculation.

Single Top Quark Production

At hadron colliders, top quarks are also produced individually through electroweak processes (Figure 2.5) via s- and t-channel or in association with a W boson (Wt-channel). Due to different final states, the single-top quark production channels can be measured individually. Separate measurements of the s- and t-channel processes provide sensitivity to physics beyond the Standard Model [54].

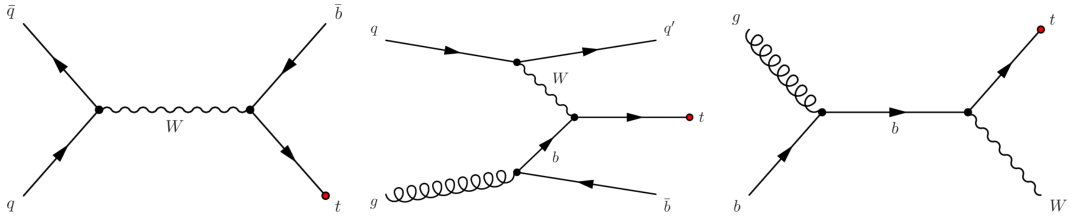

Figure 2.5.: Single top quark production via electroweak interactions through (a) s-channel, (b) t-channel and (c) in association with a W boson as Wt-channel.

Figure 2.6 compares the top quark production cross sections as pair and single quarks as a function of the centre-of-mass energy at the LHC using the MCFM Monte Carlo program [55].

2.2.2. Top Quark Decay

The top quark decays via the weak interaction mechanism into a W boson and a down-type quark (down, strange, or bottom). Due to its extremely short lifetime ($\sim 10^{-25}$ seconds), the top quark decays before hadronisation can occur. As a result, it passes its intrinsic properties such as spin, charge, etc. to its decay products, providing a unique opportunity to study the behaviour of a "bare" quark.

The probability of the top quark decay into a W boson and a certain down-type quark (d, s or b) is proportional to the corresponding CKM matrix element squared, $|V_{ti}|^2$ (Equation 2.5), where i refers to any of down-type quarks. Since $|V_{tb}| \gg |V_{td}|$, $|V_{ts}|$, it decays almost always into a W boson and a b-quark. Thus, the final state of the $t\bar{t}$ decay is classified by the W boson decay modes, which can either decay leptonically into a charged lepton (antilepton) and its corresponding antineutrino (neutrino), or hadronically into

an up-type quark (antiquark) and a down-type antiquark (quark), as summarised in Table 2.1. Therefore, the top quark decay channels are classified as:

- **all-hadronic**: If both W bosons decay through the hadronic channel. The event's final state includes six jets of which two originate from a b-quark.
- **lepton+jets**: If one W boson decays through the hadronic channel and the other one through the leptonic channel. The event's final state includes four jets (two of them originate from a b-quark), one charged lepton and missing transverse momentum corresponding to the undetectable neutrino.
- **dileptonic**: If both W bosons decay through the leptonic channel. The event's final state includes two b-quark jets, two leptons with opposite electric charge and a large missing transverse energy corresponds to the two undetectable neutrinos.

From the experimental point of view, although the all-hadronic channel has the highest branching ratio $\sim 46\%$ compared to other channels, it is the most difficult channel for an analysis due to the very high QCD multijet backgrounds. On the other hand, the dileptonic channel has a very clean final state signature leading to a high $t\bar{t}$ purity but has the lowest branching ratio.

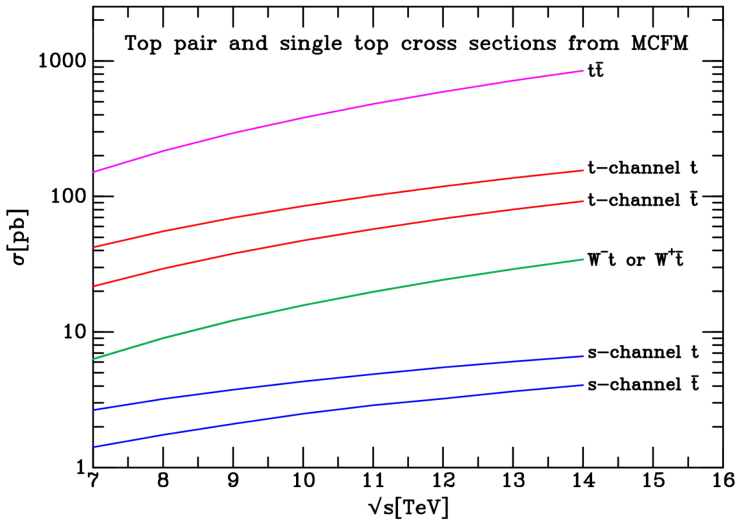

Figure 2.6.: The $t\bar{t}$ and single top quark cross section as a function of the centre-of-mass energy of the collision, calculated at NLO QCD [55].

Decay channel	Branching ratio [%]
$W \to q\bar{q}'$	67.60±0.27
$W \to e\bar{\nu}_e$	10.75±0.13
$W \to \mu\bar{\nu}_\mu$	10.57±0.15
$W \to \tau\bar{\nu}_\tau$	11.25±0.20
$\tau \to e\bar{\nu}_e\nu_\tau$	17.83±0.04
$\tau \to \mu\bar{\nu}_\mu\nu_\tau$	17.41±0.04

Table 2.1.: Branching ratios of the W boson and leptonic τ-lepton decays [56].

The analysis presented in this thesis is performed in the lepton+jets channel. This channel has a reasonable branching ratio of $\sim 43.8\%$ (considering all decays) or $\sim 35.3\%$ if only the electron or muon are considered (including the leptonic tau decay). It Requires exactly one isolated lepton in the final state and leads to lower backgrounds compared to the all-hadronic channel. Only events including an electron or muon in the final state are considered in this channel since a tau lepton cannot be considered as a final state particle due to its very short lifetime. Therefore, events with hadronically decaying tau leptons are not classified in the lepton+jets channel.

Figure 2.7 compares the different decay channels.

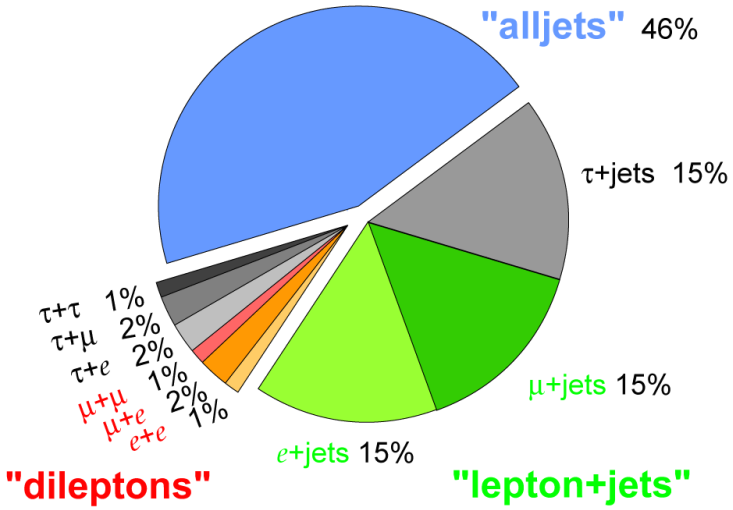

Figure 2.7.: The $t\bar{t}$ decay channel branching ratios at Born level.

2.2.3. The W Boson Polarisation in $t\bar{t}$ Decays

As discussed earlier in this section, the top quark decays before hadronisation, passing its properties such as spin, polarisation and charge information to the decay products. The top quark decays almost exclusively into a W boson and a b-quark. The purpose of this research is to studying the structure of decay vertex, Wtb through the measurement of the corresponding W boson polarisation. The Lagrangian of the top quark decay vertex is extended via the effective field theory approach by a minimum number of four couplings to the most general form as [57]:

$$\mathscr{L}_{Wtb} = -\frac{g}{\sqrt{2}}\bar{b}\gamma^{\mu}(V_L P_L + V_R P_R)tW_{\mu}^{-} - \frac{g}{\sqrt{2}}\bar{b}\frac{i\sigma^{\mu\nu}q_{\nu}}{m_W}(g_L P_L + g_R P_R)tW_{\mu}^{-} + h.c. \quad (2.18)$$

In this equation g is the weak coupling constant. The W boson mass and its four-momentum are presented by m_W and q_ν respectively, and $P_{\mathrm{L,R}}$ are the left- and right-handed chirality operators. The constants $V_{\mathrm{L,R}}$ and $g_{\mathrm{L,R}}$ are the left- and right-handed vector and tensor couplings, respectively, which are expressed in effective operators, introduced in [58].

Given the $V-A$ structure of the Wtb vertex (see Section 2.1.1) in the SM, only the left-handed vector coupling (V_L) contributes to the Lagrangian in Equation 2.18, which is equal to the V_{tb} element of the quark-mixing (CKM) matrix. The other couplings, which are known as *anomalous couplings* have no contribution at tree level. However, some Beyond Standard Model (BSM) physics processes could alter the top quark decay mechanism by allowing contributions from anomalous couplings in the Wtb Lagrangian. This alternation in the top quark decay vertex due to those models has a direct impact on the corresponding W boson polarisation (helicity fractions). The contributions that the W boson helicity fractions in top quark decay receive from some physics processes beyond the Standard Model are detailed in Section 2.2.4.

The W boson in the top quark rest frame is produced with left-handed, longitudinal, or right-handed polarisation as illustrated in Figure 2.8. The SM calculation for the W boson helicity fractions at NNLO in QCD, including the finite b-quark mass and electroweak effects, are $F_L = 0.311 \pm 0.005$, $F_0 = 0.687 \pm 0.005$, and $F_R = 0.0017 \pm 0.0001$ [7] for a b-quark mass $m_b = 4.8$ GeV and a top quark mass $m_t = 172.8 \pm 1.3$ GeV, where F_L, F_0 and F_R present the left-handed, longitudinal and right-handed helicity fractions, respectively. The theoretical precision of those fractions is comparable to the contributions from the mentioned new physics processes. Therefore, probing the

Wtb vertex is of importance in a search for new physics processes and to test the SM prediction.

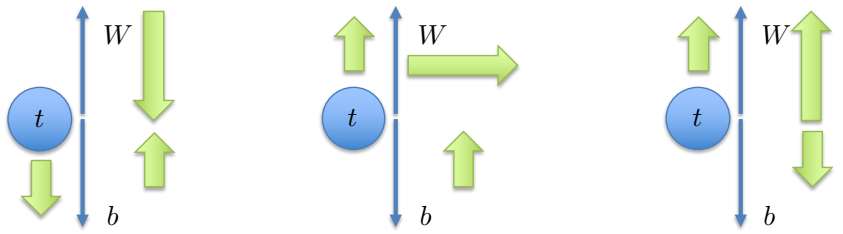

Figure 2.8.: In the decay of the top quark into a W boson and a b-quark in the top quark rest frame, the W boson helicity orientation could be: left-handed (a), longitudinal (b) or right-handed (c). The narrow (thick) arrows present the momentum (spin) of the particles.

2.2.4. BSM Effects on the Helicity Fractions

As mentioned earlier in this section, some BSM physics processes alter the top quark decay mechanism by allowing the contributions from anomalous couplings in the Wtb Lagrangian [59]. The explicit relation between those helicity fractions and the anomalous couplings are expressed analytically in [57]. In the following, some of the popular BSM models which have impact on the W boson helicity fractions in the top quark decay are introduced.

Minimal Supersymmetric Standard Model (MSSM)

In the framework of the MSSM, the supersymmetric contributions to the W boson helicity fractions arise from the one-loop corrections to the total width of $t \to bW$ when the top quark decays to lighter supersymmetric particles. The dominant corrections are the SUSY electroweak (SUSY-EW) correction, due to the interactions of charginos or neutralinos, and the SUSY-QCD correction, due to the interactions of gluinos. Detailed calculations are given in [60].

Two-Higgs-doublet model:

The two-Higgs-doublet model (2HDM) predicts the existence of five physical Higgs bosons: two neutral scalar (h^0, H^0), one pseudo-scalar (A^0) and two charged Higgs

bosons ($H^{\pm}$) [61]. In this model, the contributions to the W boson helicity fractions are arising from the decay of top quark to light charged Higgs ($t \to bH^{+}$). The free parameters of the 2HDM model are the masses of the Higgs bosons, $\tan\beta = \frac{\nu_1}{\nu_2}$ (the ratio of the vacuum expectation values of the two Higgs doublets) and the mixing angle α of the two CP-even neutral Higgs bosons. A study in [62] probed the impact of this model on the helicity fractions by varying the parameters within their current allowed ranges. Figure 2.9 shows $\Delta F_{0,R}/F_{0,R}$ as a function of $\tan\beta$, where

$$\frac{\Delta F_{0,R}}{F_{0,R}} = \frac{F_{0,R}^{2HDM} - F_{0,R}^{SM}}{F_{0,R}^{SM}}. \tag{2.19}$$

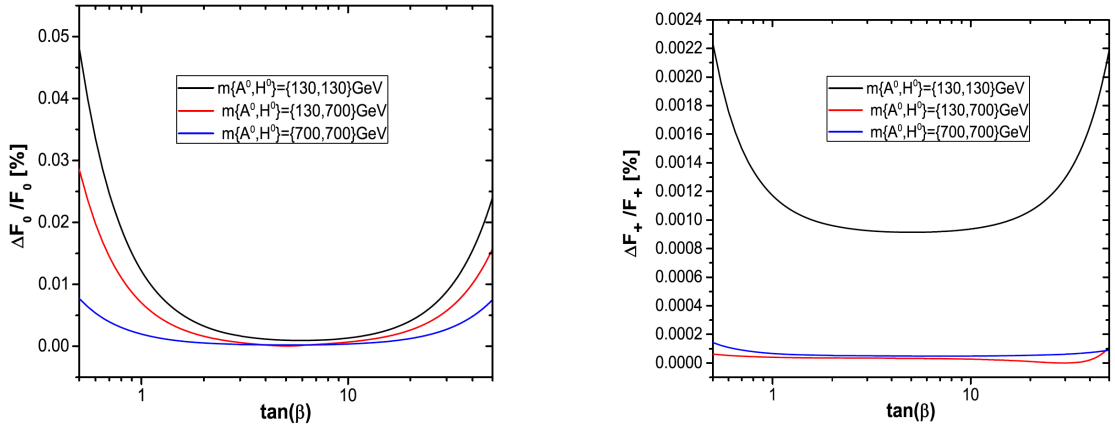

(a) (b)

Figure 2.9.: The impact of varying $\tan\beta$ of the 2HDM model on the longitudinal (a) and right-handed (b)) helicity fractions with respect to the Standard Model expectations. Other parameters of the model are fixed to the indicated values [62].

The maximum contributions to F_0 and F_R are 0.05 % and 0.002 %, respectively, which arise at low $\tan\beta$ values.

Top-colour assisted technicolour:

The topcolour-assisted technicolour (TC2) model predicts the existence of three Pseudo-Goldstone Bosons in a few-hundred-GeV region, so called top-pions (Π_t^0,$\Pi_t^{\pm}$) and one top Higgs (H_t^0) [63, 64]. The free parameters of the model are the masses of new predicted particles and their couplings. A study in [62] probed the impact of this model on the

helicity fractions by varying those parameters within their current limits. Figure 2.10 shows the variation of the right-handed helicity fraction with respect to the Standard Model ($\frac{\Delta F_R}{F_R} = \frac{F_R^{TC2} - F_R^{SM}}{F_R^{SM}}$) as a function of the top quark condensate value, f_π.

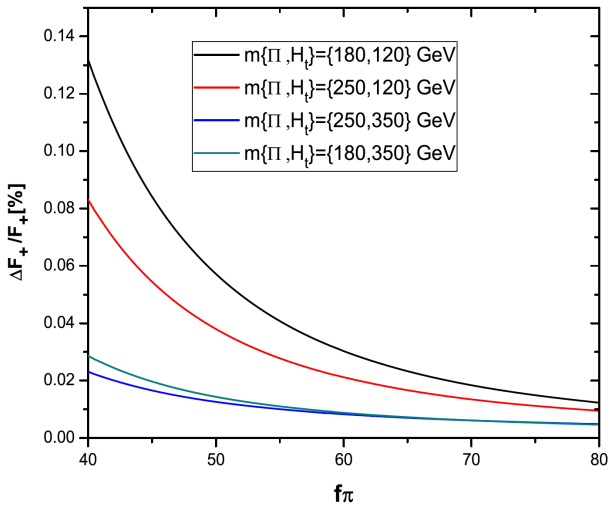

Figure 2.10.: The impact of varying the top quark condensate value, f_π of the TC2 model on the right-handed helicity fraction with respect to the Standard Model expectations. Other parameters of the model are fixed to the indicated values [62].

The maximum contribution on F_R due to the TC2 model is < 0.15 %.

2.2.5. Measurement of the W boson Polarisation

The Sensitive Observable

The helicity fractions are extracted directly from the measurements of the angular distribution of the decay products of the top quark. The angle θ^* is defined as the angle between the momentum direction of the charged lepton (down-type quark) from the leptonic (hadronic) W boson decay and the reversed momentum direction of the b-quark from the decay of the top quark, both boosted into the W boson rest frame, as shown in Figure 2.11. The differential cross section with respect to these analysers has a dependence on the helicity fractions, given by:

$$\frac{1}{N}\frac{dN}{d\cos\theta^*} = \frac{3}{8}(1-\cos\theta^*)^2 F_L + \frac{3}{4}\sin^2\theta^* F_0 + \frac{3}{8}(1+\cos\theta^*)^2 F_R, \qquad (2.20)$$

where $F_L+F_0+F_R = 1$. Figure 2.12 shows the $\cos\theta^*$ distribution for the left-handed (long dashed line), longitudinal (short dashed line) and right-handed (dotted line) W boson helicity along with the corresponding SM prediction (solid line).

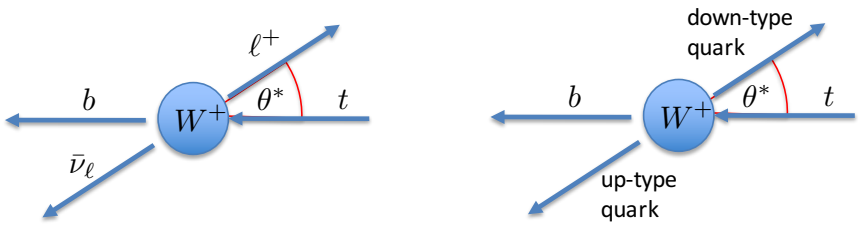

(a) (b)

Figure 2.11.: The leptonic (a) (hadronic (b)) analyser is defined as the angle between the charged lepton (down-type quark) and the negative direction of the b-quark in the W boson rest frame.

Approaches to Measuring the Helicity Fractions

A straightforward approach to measuring the helicity fractions is directly using the shape of the angular distribution of θ^* via a template fit method, which is used as the default analysis strategy in this research. The helicity fractions, F_{i} are extracted via a fit of the reconstructed $\cos\theta^*$ distribution of the $t\bar{t}$ candidate events measured in data. Details are given in Chapter 7.

Alternatively, a simplified approach of angular asymmetry is also possible for the extraction of those fractions [65, 66], by defining the angular asymmetry as:

$$A_z = \frac{N(\cos\theta^* > z) - N(\cos\theta^* < z)}{N(\cos\theta^* > z) + N(\cos\theta^* < z)}, \tag{2.21}$$

for any fixed z in $[-1, 1]$. Choosing $z = 0$, the forward-backward (FB) asymmetry, A_{FB}, is related to the helicity fractions by:

$$A_{FB} = \frac{3}{4}[F_R - F_L]. \tag{2.22}$$

Defining two other asymmetries, $A_\pm$ via choosing $z = \pm(1 - 2^{2/3})$ and $\beta = 2^{2/3} - 1$, and considering $\sum_i F_i = 1$, the full relation between these asymmetries and the helicity

fractions are:

$$
\begin{aligned}
F_0 &= -\frac{1+\beta}{1-\beta} + \frac{A_+ - A_-}{3\beta(1-\beta)}, \\
F_L &= \frac{1}{1-\beta} - \frac{A_+ - \beta A_-}{3\beta(1-\beta^2)}, \\
F_R &= \frac{1}{1-\beta} + \frac{A_- - \beta A_+}{3\beta(1-\beta^2)}.
\end{aligned}
\tag{2.23}
$$

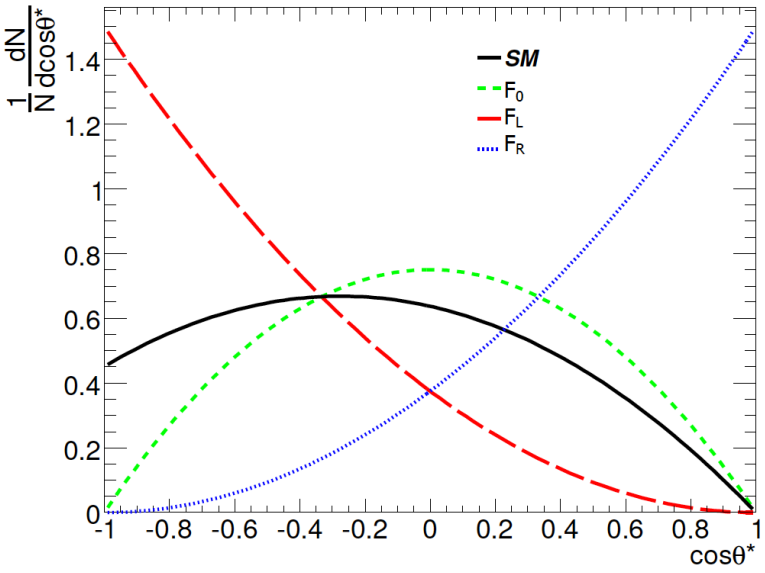

Figure 2.12.: The $\cos\theta^*$ distribution in arbitrary units. The red long dashed-line, blue dotted-line and green dashed-line represent the left-handed, right-handed and longitudinal W boson polarisation state. The black solid line refers to the corresponding SM prediction.

Recent Measurements of the W Boson Polarisation in $t\bar{t}$ Decay

The W boson polarisation in top quark decay had been measured by the CDF and DØ experiments at the Tevatron and by the ATLAS and CMS experiments at the LHC in both lepton+jets and dilepton final state channels. The results of these measurements are summarised in Table 2.2.

Experiment	$\sqrt{s}$ [TeV]	Lumi. [fb^{-1}]	Channel	Fraction	F $\pm$(stat.) $\pm$(syst.)	Ref.
CMS	8	19.8	l+jets	F_0 F_R	0.681 $\pm$ 0.012 $\pm$ 0.023 -0.004 $\pm$ 0.005 $\pm$ 0.014	[12]
ATLAS+CMS	7	2.2	l+jets & dilepton	F_0 F_R	0.626 $\pm$ 0.034 $\pm$ 0.048 0.015 $\pm$ 0.034(stat.+syst)	[67]
ATLAS comb.	7	1.04	l+jets & dilepton	F_0 F_R	0.67 $\pm$ 0.03 $\pm$ 0.06 0.01 $\pm$ 0.01 $\pm$ 0.04	[11]
CMS	7	5.0	l+jets	F_0 F_R	0.682 $\pm$ 0.030 $\pm$ 0.033 0.008 $\pm$ 0.012 $\pm$ 0.014	[14]
CDF+DØ	1.96	2.7-5.4	l+jets & dilepton	F_0 F_R	0.722 $\pm$ 0.062 $\pm$ 0.052 -0.033 $\pm$ 0.034 $\pm$ 0.031	[68]

Table 2.2.: Summary of the previous W boson helicity measurements performed by CDF and DØ at the Tevatron and ATLAS and CMS at the LHC in the lepton+jets and dilepton channels

3

The ATLAS Experiment at the LHC

Due to the very small cross section of proton–proton collision, in each bunch crossing only a tiny fraction of the particles actually collide at the LHC. Having a reasonable amount of statistics is crucial for precision measurements or the observation of very rare events.

The particle accelerators are either linear or circular and regardless of the accelerator type, the particles are pushed with an electric-field wave. However, each type has some advantages and limitations. For instance, in circular colliders the bunch of particles travel around in opposite directions, and can be collided over and over, providing a high rate of collisions. In addition to the higher rate of collision, the particles in a circular accelerator obtain multiple kicks of energy each time round without having to be of tremendous length as the linear accelerators. On the other hand, in circular colliders, the energy of the collision is limited due to losses from *synchrotron radiation* which is proportional to $1/m^4$, where m is the mass of the accelerated particle, and to the $1/R$ bending radius. Due to the former limitation, it is extremely challenging to achieve high energy collisions via light particles such as electrons compared to hadrons.

The required energy to create a pair of top quarks is $\sqrt{s} = 2m_t$. Accessing this amount of energy is only possible via hadron colliders, in particular, the Tevatron and the LHC via proton (anti)-proton collisions. In this thesis, the data of proton-proton collisions collected by the ATLAS detector at the LHC are analysed. In the first section of this chapter, a general overview of the LHC is given. A brief description of the ATLAS detector and its most important subcomponents will follow. Finally, the chapter is closed by data taking conditions at $\sqrt{s} = 8$ TeV.

3.1. The Large Hadron Collider

The Large Hadron Collider [69] at the Conseil Européen pour la Recherche Nucléaire (CERN) near Geneva, is the largest and most powerful hadron collider ever constructed. It lies in a tunnel 27 kilometres in circumference and on average 100 metres underground. The LHC was built between 1998 and 2008 with four crossing points around the ring, which host seven detectors, each designed for certain kinds of research. ALICE [70], ATLAS [71], CMS [72] and LHCb [73] are the four major experiments housed in IP1 (ATLAS), IP2 (ALICE), IP5 (CMS) and IP8 (LHCb). LHCf [74], MoEDAL [75] and TOTEM [76] are smaller special–purpose experiments that share the the same cavern with the sATLAS, LHCb and CMS experiments, respectively.

The ATLAS and CMS experiments with a large solid angle coverage are designed to be general-purpose detectors. Mainly they are designed to allow testing of different theoretical models of particle physics predictions that might become detectable in the high energy collisions. Investigating the missing piece of the Standard Model at the time of construction, the Higgs boson, searching for Dark Matter candidates and new particles predicted by supersymmetry and addressing other open questions of the SM are the most important goals of these experiments.

The ALICE experiment is optimised to study heavy-ion collisions[1] at a centre-of-mass energy of 2.76 TeV per nucleon pair. This condition with such high temperature and energy density is suitable to study the signature of the *quark–gluon plasma*. The LHCb experiment is a specialised b-physics experiment. It focuses on the studies of CP violation in the hadrons containing b-quarks, as a key phenomenon to understand the matter–antimatter asymmetry in the Universe. In addition to the main experiments, there are three smaller special-purpose experiments at the LHC: The TOTEM detector is designed to study the total cross section, elastic scattering, and diffractive processes. The MoEDAL experiment designed with prime goal of search for the magnetic monopole (MM) or dyon and other highly ionising stable massive particles (SMPs) and pseudo-stable massive particles. And the LHCf experiment purpose is to study the particles produced in the forward region of collisions, i.e. in the line of proton beams.

Unlike the Tevatron accelerator which requires one beam–pipe to accelerate the proton and antiproton in opposite directions, there are two adjacent parallel beam–pipes in the LHC, intersecting at four points. 1,232 superconducting dipole magnets are used to keep

[1] The LHC mostly collides protons but it also collides proton-lead ions and lead-lead ions for some short periods (typically one month per year) to an in-depth look at the physics of the quark/gluon plasma.

the beam of particles on the circular path. Additionally, 392 quadrupole magnets are utilised to keep the beam focused by squeezing it vertically or horizontally, to increase the probability of interaction where the two beams cross. Higher multipole orders magnets are also used to correct smaller imperfections in the field geometry and to stabilise the beam.

Approximately 96 tonnes of liquid Helium are used in order to keep those magnets at their operating temperature of $\sim$ 1.9 K. Technically, rather than having a continuous beam of particles, the particles are bunched together and the interactions between the two beams take place at discrete intervals, typically every 25 ns, i.e. in a bunch collision rate of 40 MHz. In the full operation, the LHC is designed to accelerate 2808 bunches, each containing about 10^{11} particles, achieving an instantaneous luminosity of $\mathcal{L} = 10^{34}\text{cm}^{-2}\text{s}^{-1}$. However, in the run I, the LHC operated with 50 ns bunch spacing (1380 bunches). The first research run at the LHC took place from March 2010 to February 2013 at a centre-of-mass energy of collision of $\sqrt{s} = 7$ TeV, followed by a raise to $\sqrt{s} = 8$ TeV in 2012, before the official end of run I data taking period and the first long shutdown for the planned upgrades. The collisions restarted on May 2015 with a centre-of-mass energy of $\sqrt{s} = 13$ TeV, presenting the world's highest energy of collisions ever achieved. The next long shutdown and upgrades are supposed to take place at 2018-2019, before a further increase of the energy of collisions to $\sqrt{s} = 14$ TeV and luminosity of $\mathcal{L} \sim 2 \times 10^{34}\text{cm}^{-2}\text{s}^{-1}$ in the third data taking period. The next upgrade phase is scheduled to further increase the luminosity up to $\mathcal{L} \sim 5 \times 10^{34}\text{cm}^{-2}\text{s}^{-1}$ in the year 2022 and planned to operate the High Luminosity-LHC (HL-LHC) to collect 3,000 fb^{-1} of data by $\sim$2035.

To make a high energy proton-proton collision in the main ring of the LHC, the particle undergoes a pre-acceleration chain to successively gain energy. At first, the protons from the ionised hydrogen gas are accelerated to 50 MeV in the linear accelerator LINAC2 before being injected into the Proton-Synchrotron Booster (PSB). Then the protons are accelerated to 1.4 GeV to be injected into the 628 m ring of the Proton-Syncrotron (PS), where it accelerates them up to 26 GeV. As the final injector for the main LHC ring, the Super-Proton-Syncrotron (SPS)[2], a 6.9 km in circumference circular accelerator increases the energy of the protons to 450 GeV. In the main ring, the protons are accelerated to the maximum target energy and collide in the four intersection points. Figure 3.1 schematically shows the full system of acceleration chain in details.

[2]From 1981 to 1984, the SPS operated as proton – antiproton collider and provided data for the UA1 and UA2 experiments, where the W and Z bosons were discovered [27–30]

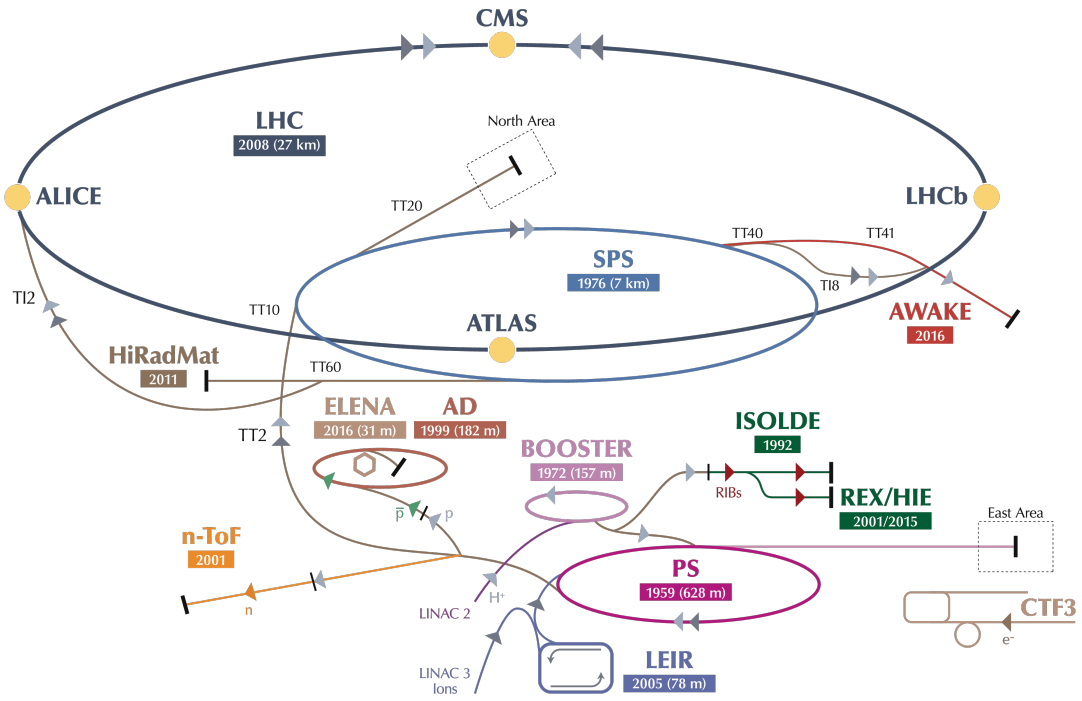

Figure 3.1.: CERN accelerator complex [77].

3.2. The ATLAS Detector

The ATLAS (A Toroidal LHC ApparatuS) detector [71] is one of the four major detector experiments at the LHC. With almost full solid angle (4π) coverage, it is designed as a general-purpose detector. It has approximately a cylindrical geometry with the constituents aligned in a typical onionskin structure. ATLAS is 44 metres long, 25 metres in diameter, and weighs about 7,000 tonnes. It is composed of four major parts: Magnet Systems, Inner Detector, calorimeters and the Muon Spectrometer. Figure 3.2 sketches an overview of the ATLAS detector with its components.

These sub–detector components are complementary: Particles emerging from the collisions will first interact with the Inner Detector (ID) system. It tracks charged particles and allows to measure their momentum precisely. In the electromagnetic and hadronic calorimeters, the majority of the particles deposit their entire energy and stop. Hence the particle's energy can be determined by measuring the amount of energy deposition in the corresponding hit cells. The muon system makes additional measurements of muons

which do not stop in the calorimeters. The magnet systems bend the path of charged particles in the ID and the Muon Spectrometer via the strong magnetic field, allowing for the charge and momenta measurement via the particle's track curvature. The neutrino interacts only via the weak interaction. Thus, it is the only stable particle in the SM that cannot be detected directly, traversing the whole detector system without any interaction. However, it can by detected indirectly by measuring the momentum imbalance among the other detected particles in each event via the conservation of energy and momentum laws. Figure 3.3 summarises the basics of the particle identification based on each particle characteristics.

Geometry and Coordinate System

The typical coordinate system used in ATLAS is a right-handed cartesian coordinate system (x, y, z), where the beam direction is along the z-axis and the x–y plane is transverse to the beam direction. The positive x-axis direction points from the interaction point to the centre of the LHC ring and the positive y–axis direction points upwards. The corresponding transformation to the spherical coordinate system (r,θ, ϕ) is straightforward

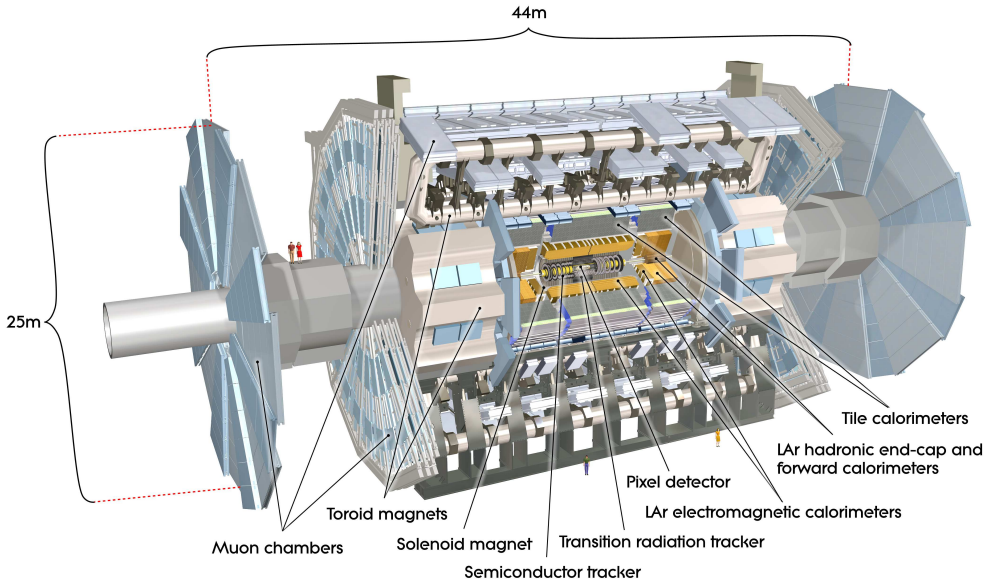

Figure 3.2.: Cut-away view of the ATLAS detector. The dimensions of the detector are 25 m in height and 44 m in length. The overall weight of the detector is approximately 7000 tonnes. [71].

and defined as:

- The azimuthal angle ϕ lies in the x–y-plane.
- The polar angle θ lies in the r–z-plane, where $r = \sqrt{x^2 + y^2}$.

For highly relativistic particles, i.e. $E \gg m$, it is more convenient to use the pseudo–rapidity defined as:

$$\eta = -\ln[\tan(\frac{\theta}{2})], \tag{3.1}$$

rather than the polar angle θ, since its difference ($\Delta\eta$) is an invariant quantity with respect to Lorentz boosts along the beam axis[3]. In the pp collision, the initial momentum of the colliding partons is an unknown fraction of the proton's momentum. However, due to the momentum conservation, the momentum balance of all outgoing particles of an event in the transverse plane must be zero. Thus, the transverse momentum p_{T} of a

[3]Rapidity difference is also an invariant quantity with respect to Lorentz boosts along the beam axis. The only problem with it, is that it is hard to measure for highly relativistic particles, since it needs the energy and the total momentum of the particle. Technically, at high values of the rapidity, due to the large z component of the momentum, the beam axis prevents the precise measurement of the total momentum.

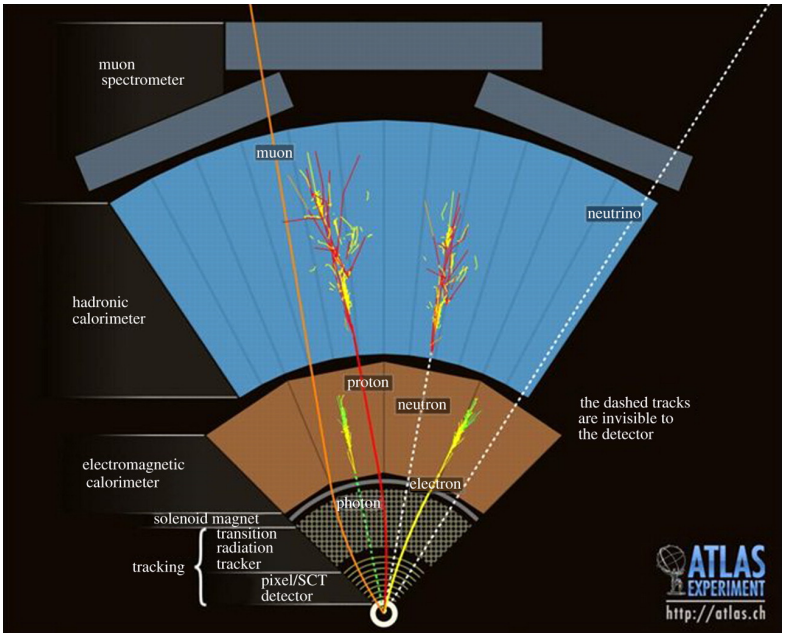

Figure 3.3.: Different patterns of energy deposits allows the identification of different types of particles produced in collisions.

particle is an interesting quantity and defined in both cartesian and spherical coordinate systems as:

$$p_{\mathrm{T}} = \sqrt{p_x^2 + p_y^2} = |p| \sin\theta, \tag{3.2}$$

where p_x and p_y are the momentum components in the x- and y- directions and $|p|$ is the absolute value of the momentum.

The analysed data in this thesis was collected by the ATLAS detector in 2012 in a centre-of-mass energy of $\sqrt{s} = 8$ TeV, and corresponds to an integrated luminosity of 20.2 fb^{-1}. In the following subsections, more details of each sub-detector component and trigger systems are discussed.

3.2.1. Magnet System

ATLAS utilises a unique hybrid system of four large superconducting magnets, a solenoid, a barrel toroid and two end-cap toroids. The central solenoid with a coil mass of 5.4 tonnes and stored energy of 40 MJ is aligned on the beam axis which provides a 2 T axial magnetic field for the Inner Detector. The barrel toroid and two end-cap toroids provide 0.5 T and 1 T toroidal magnetic fields for the muon detectors in the central and end-cap regions, respectively, as schematically shown in Figure 3.4. The barrel toroid consists of eight coils encased in individual racetrack-shaped, stainless-steel vacuum vessels. The magnetic field produced by the barrel toroid is filling the cylindrical volume surrounding the calorimeters and both end-cap toroids. The end-cap toroids generate the magnetic field required for optimising the bending power in the end-cap regions of the muon spectrometer system.

The whole magnetic system is 22 m in diameter and 26 m in length, with a stored energy of 1.6 GJ. In order to keep the magnets superconducting, both systems are cooled down to $\sim$ 4.5 K via liquid Helium. The complete details about the specifications and main parameters of the systems are given in [71].

3.2.2. Inner Detector

The ATLAS Inner Detector begins only 5 centimetres away from the beam–pipe, and it is the closest detection system to the interaction point. Its basic function is to track charged particles. The magnetic field surrounds the entire Inner Detector and bends the path of charged particles. Hence, reconstructing the ionisation path reveals detailed information about the types of the particles and their momentum. The ATLAS ID tracks the charged particles via utilising three different technologies based on the fact

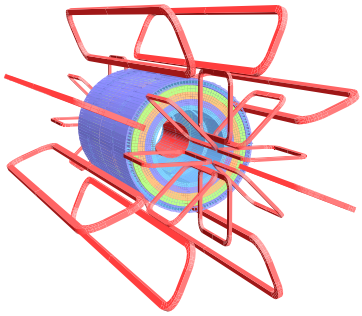

Figure 3.4.: The ATLAS magnet system [71].

that the charged particles create electron-hole pairs while passing through the medium. Therefore, by collecting the produced electrons as signals in discrete plates, the particle is traced. Figure 3.5 sketches the Inner Detector components in detail, which cover a range of $|\eta| < 2.0$.

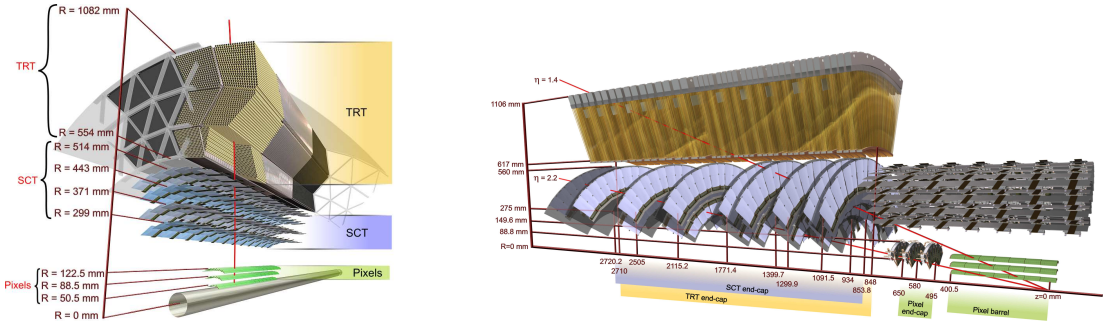

(a) (b)

Figure 3.5.: Cut-away view of the ATLAS Inner Detector barrel (a) and end-cap (b) [71].

The ATLAS ID consists of three independent but complementary subsystems:

Pixel Detector

The Pixel Detector as the innermost component of the ID is based on the silicon sensor technology. It is composed of 1,744 modules arranged in three barrel layers and three disc layers on each end-cap and provides the highest resolution in the ID. On each module there are 16 front-end chips (FE) that control 46,080 readout channels connected to the

pixels of size 50×400 μm^2, making about 80.4 million readout channels in all layers[4]. In addition to the high-precision measurement of the impact parameter of the tracks, the pixel detector plays a crucial role in the identification of secondary vertices caused by the heavy flavour decays, which is critical for b-jet tagging (see Section 4.5.2).

During the first LHC long shutdown the ATLAS beam–pipe was replaced with a new smaller radius beam–pipe at a radius of 3.3 cm with an additional layer of pixel sensors directly attached to it. This additional layer is expected to significantly improve the reconstruction of the secondary vertices and thus it is called *Insertable B-layer* (IBL). In order to cope with the high radiation and particle occupancy in this layer, improved readout chips and new silicon sensor technologies (thin planar sensors and 3D double sided sensors) are utilised [78][5].

Semi-Conductor Tracker

The Semi-Conductor Tracker (SCT) detector surrounding the Pixel Detector, is another silicon-based detector, but consists of silicon *micro-strips* rather than pixels, each 80 μm wide and about 12 cm long. The SCT is composed of four double layers of silicon strips in the barrel and nine disks for each end-cap (3100 modules in total) resulting in about 6.3 million readout channels. In order to reduce the thermal noise and to obtain an optimal functionality, both the Pixel Detector and the SCT are cooled down to -7°C.

Transition Radiation Tracker

The Transition Radiation Tracker (TRT) is the outermost component of the Inner Detector, which surrounds the SCT. The transition radiation is electromagnetic radiation emitted when a charged particle passes through inhomogeneous media, such as a boundary between two media with different dielectric constants. Rather than the silicon technology, the TRT uses straw drift tubes of 4 mm diameter filled with Xe/ CO_2/O_2 gaseous mixture to track the charged particles. A thin gold-plated tungsten wire is housed inside each tube to drift the free electrons that are created via the ionisation process when the charged particle passes through the gas tubes. The spaces between the straws are filled with polymer fibres (barrel) and foils (end-caps), which provide transition radiation

[4] About 10% of the pixels are of size 50×600 μm^2 located in the regions at the front-end chips on a module.

[5] The analysed data in this thesis is taken before inserting the IBL.

to identify electrons from pions[6]. With an average of 36 hits per track with transverse momentum $p_T > 0.5$ GeV, except in the barrel-end-cap transition region $0.8 < |\eta| < 1.0$ which is 22 hits, the TRT provides continuous tracking and improved momentum resolution.

The combination of those systems provides precise track and vertex reconstruction, and high precision in both $r - \phi$ and z coordinates.

3.2.3. Calorimeter System

The ATLAS Calorimeter system is located outside the solenoidal magnet that surrounds the ID. It consists of an inner electromagnetic (EM) and an outer hadronic calorimeter as shown in Figure 3.6. As the name indicates, its purpose is to measure the energy of particles. The principle of calorimeters is based on total absorption of the energy.

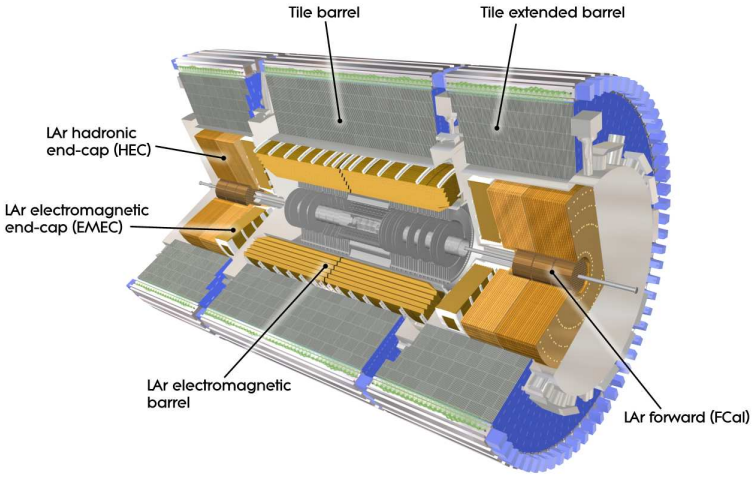

Figure 3.6.: Cut-away view of the ATLAS calorimeter system [71].

The electrons (positrons) lose energy due to the emission of photons (*Bremsstrahlung*) and photons are losing energy via e^+e^- pair production mechanism. In case that the created particles have enough energy, they can radiate photons, photons produce more e^+e^- pairs and this sequence is goes on until the energy drops below the critical energy where at this level, the cascade ends quickly by classic absorption of energy. This mechanism generates a large shower of particles in the detector. The distance X_0 that the initial

[6]Electrons and pions emit a different amount of transition radiation when traversing material with different dielectric constants.

particle travels until its energy decreased by a factor of $1/e$ is defined as *radiation length*, and depends on the medium that it is travelling in. In order to avoid any punch-through effects and to ensure that all particles (except neutrinos and muons) get absorbed in the calorimeter system, the material and thickness of the calorimeter system should be chosen carefully to be able to stop particles with an energy of several hundred GeV.

The hadronic particles undergo different processes to lose energy in the calorimeter. Basically, a hadron loses energy due to interactions with nuclei, e.g. excitation and breaking up of nuclei. In addition, in a hadron shower, a part of the energy is converted to EM shower, via $\pi^0 \to \gamma\gamma$. The corresponding term for radiation length for hadronic particles is called *nuclear interaction length*, λ_I, and it is typically larger than X_0. The hadronic shower is also much broader than the EM shower.

The muon is the only detectable particle that is able to pass through the calorimeter systems, depositing a very small fraction of its energy. Due to its heavy mass with respect to the electron, in typical energies at collider experiment, a muon cannot radiate enough energy via the Bremsstrahlung process[7]. Therefore, it does not produce electromagnetic showers and acts as *minimum ionising particles* (MIPs).

Typically the calorimeters are constructed either in homogeneous type or in sampling type. In the homogenous type, the absorber and detector material is the same. It has a good energy resolution, but it has a limited spatial resolution. On the other hand, in the sampling type, the absorber (passive) and detector (active) materials are arranged in separated layers. The energy deposit in the sampling calorimeter is not equal to the measured energy. Thus, it has a limited energy resolution but good spatial resolution. The ATLAS calorimeters are of sampling type.

The energy resolution of a calorimeter is expressed as:

$$\frac{\sigma_E}{E} = \sqrt{\frac{a^2}{E} + \frac{b^2}{E^2} + c^2}, \tag{3.3}$$

where a is the coefficient of the sampling term, representing the statistical shower development, b accounts for electronic noise, radioactivity and pile up which is known as noise term and c is a constant quality factor term to account for inhomogeneities, non-linearities and bad cell intercalibration.

[7] At energies above ~ 500 GeV the Bremsstrahlung process become significant.

The Electromagnetic Calorimeter

The ATLAS Electromagnetic Calorimeter (ECal) is a high granularity Liquid-Argon (LAr) sampling calorimeter with excellent performance in terms of energy and position resolution. It has accordion-shaped Kapton electrodes, which provide complete ϕ symmetry, and use lead and stainless steel as passive material and covers a pseudorapidity range of $|\eta| < 3.2$. The total thickness of the ECal is $22 < X_0 < 30$ radiation lengths in the barrel and $24 < X_0 < 33$ in the end-caps.

The ECal is divided into a barrel part ($|\eta| < 1.475$) and two end-cap parts ($1.375 < |\eta| < 3.2$). The barrel component is composed of two identical half-barrels, separated by a small gap (4 mm) at $z = 0$. The end-cap parts are also divided into outer ($1.375 < |\eta| < 2.5$) and inner ($2.5 < |\eta| < 3.2$) coaxial wheels. In total the ECal uses about 202,000 readout channels [71].

The Hadronic Calorimeter

The Hadronic Calorimeter (HCal) is composed of three main parts: The Tile calorimeter in the barrel region, hadronic end-cap calorimeter (HEC) and forward calorimeter (FCal). The Tile calorimeter [79] is a steel (absorber)/plastic scintillator (detector) sampling calorimeter, located in the region $|\eta| < 1.7$ and surrounds the ECal. It is divided into central and two extended barrels. In order to measure the energy deposition, the corresponding scintillator light is passed through wavelength shifting fibres to photomultipliers. The HEC is a copper (absorber)/liquid-Argon (detector) sampling calorimeter with a flat-plate design. It is composed of two cylindrical wheels in each end-cap cryostat (HEC1 and HEC2) and covers the range of $1.5 < |\eta| < 3.2$. The last component of the hadronic calorimeters system is the forward calorimeter, which is housed in the same cryostats as the end-cap calorimeters. It covers the range of $3.1 < |\eta| < 4.9$ and is designed to minimise energy losses in cracks between the calorimeter systems and to reduce the amount of backgrounds reaching the muon system. The FCal is also a sampling calorimeter using liquid-Argon as the active material with copper (electromagnetic part) and tungsten (hadronic part) as absorbers. The minimum HCal thickness at $\eta = 0$ is 9.7 interaction lengths (λ_I) and ($10\lambda_I$ in the end-cap).

3.2.4. Muon Spectrometer

The Muon Spectrometer (MS) is the outermost system of the ATLAS detector. It is an extremely large tracking system, instrumented with a dedicated trigger system and high-

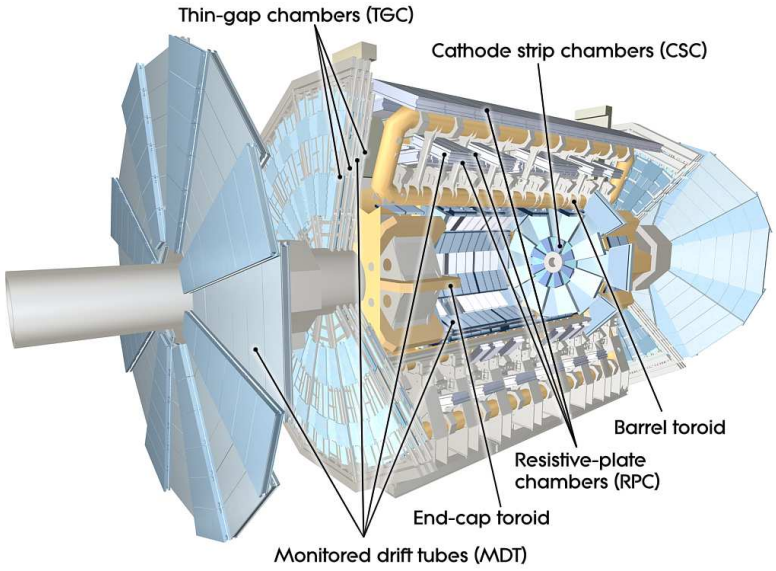

Figure 3.7.: Cut-away view of the ATLAS muon system [71].

precision tracking chambers. It is immersed in the magnetic field of the large barrel toroid ($|\eta| < 1.4$) and the two smaller end-cap magnets inserted into both ends of the barrel toroid ($1.6 < |\eta| < 2.7$). In the transition range of $1.4 < |\eta| < 1.6$, the magnetic deflection is provided by a combination of barrel and end-cap fields. The barrel chambers are arranged in three cylindrical layers around the beam axis. In the end-cap and transition regions, the plane chambers are organised also in three layers, perpendicular to the beam. An overview of the muon system with its different components and the location of the air-core toroid magnets is presented in Figure 3.7.

In both barrel and end-cap regions, a precision measurement of the track coordinates is provided by Monitored Drift Tubes (MDTs). The MDT system is composed of 1088 chambers arranged in 3-8 layers [71]. The Aluminium cylinders filled with a mixture of Ar/CO_2 gas and host a central Tungsten-Rhenium anode to collect the free electrons produced via the ionisation process by the passing muon. At the end-cap region, where higher particle flux is expected, in addition to the MDTs, the multi-wire Cathode Strip Chambers (CSCs) with higher granularity and shorter readout time are used in the innermost plane.

The Resistive Plate Chambers (RPCs) and Thin Gap Chambers are used for triggering purpose in the barrel and end-cap regions respectively. Both of these systems benefit from

fast readouts. Hence, they also provide additional tracking information.

The muon track reconstruction algorithm uses the information from both ID and MS to make a combined muon track.

The MS is designed to measure muon momenta between 3 GeV and 3 TeV with good momentum resolution and charge identification. The design muon momentum resolution, σ_{p_T}/p_T is about 10% for 1 TeV muons and about 3% for 10-200 GeV muons [80].

3.2.5. Trigger System and Data Acquisition

As mentioned earlier in this chapter, the interaction between the two beams is designed (in 2012 data taking) to take place every 25 (50) ns, i.e. in a bunch collision rate of 40 (20) MHz, leading to a huge amount of data, which is technically impossible to handle. However, this huge collision rate is dominated by events involving only QCD processes, which do not needed to be recorded at such a high rate. On the other hand, the interesting processes have well-known signatures such as energetic leptons or jets or large transverse momentum imbalance. In order to reduce the total data flow without losing interesting physics processes, the Trigger and Data Acquisition (TDAQ) system is designed to select those rare events with high efficiency and reduces the event rate to approximately 200 Hz, for an average event size of approximately 1.3 Megabytes to be permanently stored [80].

The ATLAS trigger system consists of three levels of event selection: the hardware-based Level-1 (L1) and a software-based High-Level Trigger (HLT) which is composed of Level-2 (L2), and Event Filter (EF). A block diagram of the trigger and data acquisition systems is shown in Figure 3.8.

The L1 trigger selects events with high p_T muons, electrons/photons, jets, and hadronically decaying τ leptons and events with large transverse momentum imbalance. The event rate passing L1 is reduced to $\sim$ 75 kHz. Since every 25 ns (50 ns in run I), L1 needs to make a decision and this decision must reach the front-end electronics within 2.5 μs after the bunch-crossing, the hardware is located close to the detector. L1 decision relies on the fast MS triggers (RPC and TGC) and calorimeters, e.g. for an identified muon via MS triggers, L1 estimates the momentum via look-up tables and makes the appropriate decision, without accessing the track information. In case that L1 accepts an event, it fires a Region of Interest (ROI) signal to the L2 trigger.

The L2 trigger is then restricted to looking at the data within the ROI. It has access to information from all detector components including the tracking systems. With an average event processing time of $\sim$ 40 ms, it runs simple reconstruction algorithms,

performs precise p_{T} measurements and requires isolation criteria for leptons, reducing the event rate to below 3.5 kHz.

The last triggering step is done via EF, which uses offline analysis procedures such as track and vertex reconstruction, on fully-built events. It uses all available information to further decrease the event rate to about 200 Hz with an average event processing time of ~ 4 s [71]. Events passing the EF are stored permanently on local storage disks to be used for offline analyses.

3.3. ATLAS Performance in Run 1

The first physics data delivered to the ATLAS experiment in 2010 was at the centre-of-mass energy of $\sqrt{s} = 7$ TeV. ATLAS recorded 5.08 fb^{-1} out of 5.46 fb^{-1} collision data delivered by the LHC by end of 2011, with an instantaneous luminosity of 3.7×10^{33} cm^{-2}s^{-1}, where 4.57 fb^{-1} ($\sim 90\%$) passed the ATLAS quality criteria for physics analyses. In 2012 the centre-of-mass energy of collisions increased to $\sqrt{s} = 8$ TeV, where 22.8 fb^{-1} of data delivered by the LHC, 21.3 fb^{-1} of which was recorded by ATLAS and 20.3 fb^{-1} ($\sim 95\%$) fulfilled the ATLAS quality criteria for physics analyses[8]. Figure 3.9a

[8] A newer calibration study in [81] has re-evaluated the delivered data as 21.7 fb^{-1}, of which 20.2 fb^{-1} pass the good quality conditions for physics analysis.

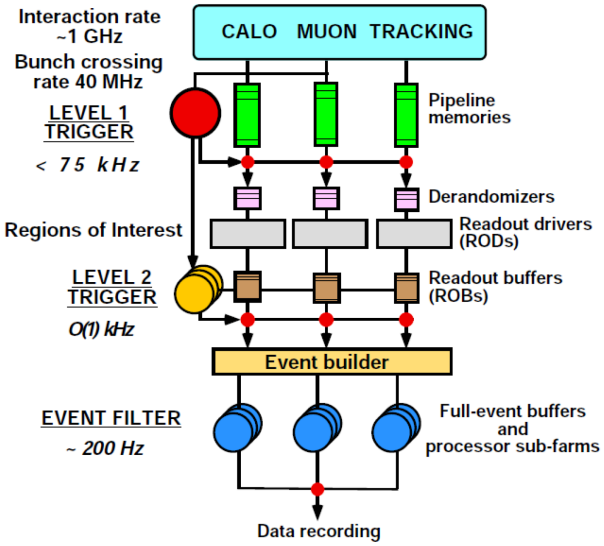

Figure 3.8.: Block diagram of the ATLAS trigger and data acquisition systems [80].

shows the data taking efficiency by comparing the delivered data by the LHC, recorded by ATLAS and certified as good quality data for physics analysis as a function of the running time during the Run 1 of the LHC [82].

The instantaneous luminosity of 2012 data increased by about factor of two (3.7×10^{33} cm^{-2}s^{-1}) with respect to 2011. This is followed by an increase in the number of interactions per bunch crossing in addition to the collision of interest, causing pile-up background. The pile-up background affects physics object reconstruction, which has a direct impact on the performance. Figure 3.9b shows the luminosity-weighted distribution of the mean number of interactions per bunch crossing for the 2011 and 2012 data taking periods. The mean number of interactions per bunch crossing is calculated from the instantaneous luminosity per bunch as:

$$\mu = \frac{\mathcal{L}_{bunch} \times \sigma_{inel}}{f_r}. \tag{3.4}$$

In Equation 3.4, $\mathcal{L}_{bunch}$ refers to the instantaneous luminosity per bunch, σ_{inel} is the inelastic cross section which is taken to be 71.5 mb (73 mb) for 7 TeV (8 TeV), and f_r is the LHC revolution frequency equal to 11.2455 kHz [83].

In next chapter, the ATLAS optimisation efforts to reduce the dependency of the reconstruction performance to pile-up effects are discussed in more details.

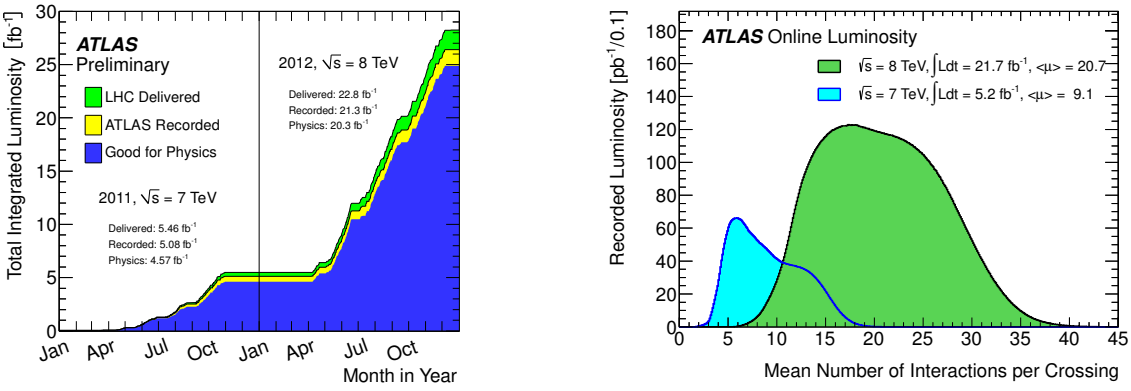

(a) (b)

Figure 3.9.: The comparison of cumulative luminosity delivered, recorded and certified as good quality for physics analysis (a) and the luminosity-weighted distribution of the mean number of interactions per crossing (b) for 2011 and 2012 data [82].

Subdetector	Number of Channels	Operational Fraction
Pixels	80 M	95.0%
SCT Silicon Strips	6.3 M	99.3%
TRT Transition Radiation Tracker	350 k	97.5%
LAr EM Calorimeter	170 k	99.9%
Tile calorimeter	9800	98.3%
Hadronic endcap LAr calorimeter	5600	99.6%
Forward LAr calorimeter	3500	99.8%
LVL1 Calo trigger	7160	100%
LVL1 Muon RPC trigger	370 k	100%
LVL1 Muon TGC trigger	320 k	100%
MDT Muon Drift Tubes	350 k	99.7%
CSC Cathode Strip Chambers	31 k	96.0%
RPC Barrel Muon Chambers	370 k	97.1%
TGC Endcap Muon Chambers	320 k	98.2%

Table 3.1.: The operational fraction of each of the ATLAS sub-detectors [84].

An overview of the ATLAS detector performance for the 2012 data taking period is presented in Table 3.1, which gives the operational fraction of each of the ATLAS sub-detectors. During Run I of the LHC, the ATLAS detector achieved the fraction of operational channels of $> 95\%$.

4

Object Definition

Carrying out a complete physics analysis requires several processes to be performed to convert the electrical signals, i.e. electrical currents and voltages, measured in different sub-detectors to sensible physics information. This information is used in the particle's tracks and energy deposition reconstruction, which is in turn used to reconstruct various physics objects. These physics objects can be described at different levels which are sketched in Figure 4.1.

As mentioned in Section 2.2.1, the high energy proton-proton collision is effectively a parton-parton collision. The first level of this interaction which is indeed the hard interaction process is called *parton level*. The final state of the hard process contains quarks and gluons which undergo the so-called hadronization process due to the colour confinement phenomenon (see Section 2.1.2). The electrons and photons in addition to the secondary particles produced via the hadronization process produce the particle shower, which is detectable in both tracking and calorimetry systems of the detector. This level is called the *particle level*. The interaction between these particles and the different sub-detector components forms the *detector level* which is also known as *reconstruction level*.

The reconstruction level is visualised by the experiments performed at the LHC via using the collision *event display* to trace the paths of particles produced in a collision. The event display is very helpful in visualising specific physical processes and for checking that the detector and software function properly. Figure 4.2 presents a $t\bar{t}$ candidate event in the ATLAS event display. The physics objects of interests are shown in colours.

The measurement of the W boson polarisation discussed in this thesis is performed by selecting events containing one electron or muon, jets and missing transverse momentum,

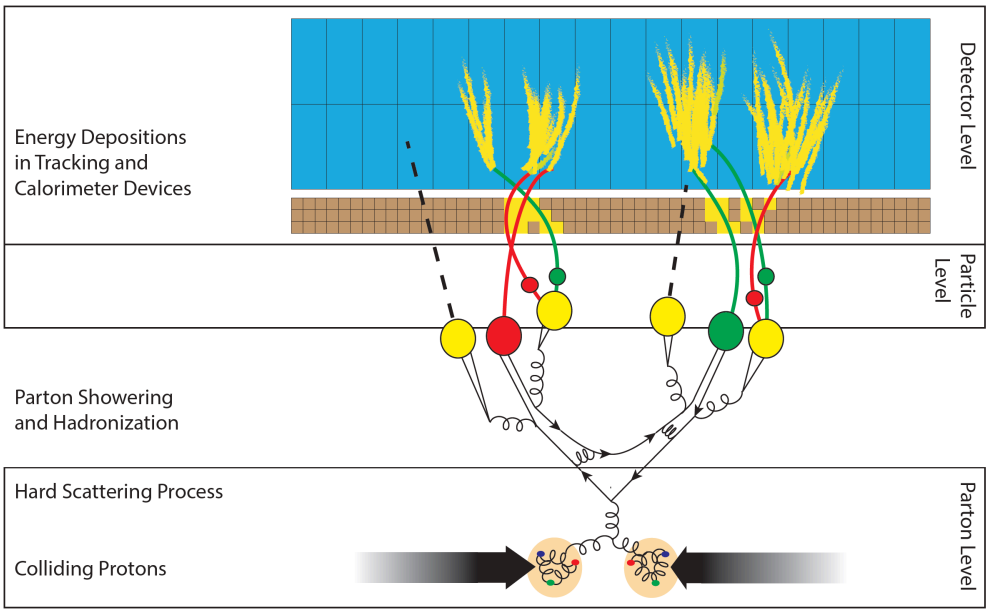

Figure 4.1.: Illustration of a particle detection process and the different levels of object descriptions.

due to the presence of a neutrino from the leptonic decay mode of one of the W bosons in the final state. In this chapter the identification and reconstruction of those objects are discussed.

4.1. Reconstruction of Tracks and Vertices

As discussed in Section 3.2.2, the Inner Detector's basic function is to track the charged particles. A track of a particle moving through the barrel would typically have 3 pixel, 8 SCT and more than 30 TRT straw hits. The tracks are reconstructed within the ID acceptance of $|\eta| < 2.5$ and full ϕ coverage. An *inside-out* pattern recognition is utilized by creating 3d space points from the silicon seeds of both Pixel and SCT detectors. Those seeds are then used to construct roads which contain hits by moving towards the outer edge of the silicon detectors and extends the probe to include the TRT hits. An *outer-in* tracking is also preformed in order to account for tracks from secondary interactions, starting from the TRT track segment seed and moves inwards. The collection of hits is

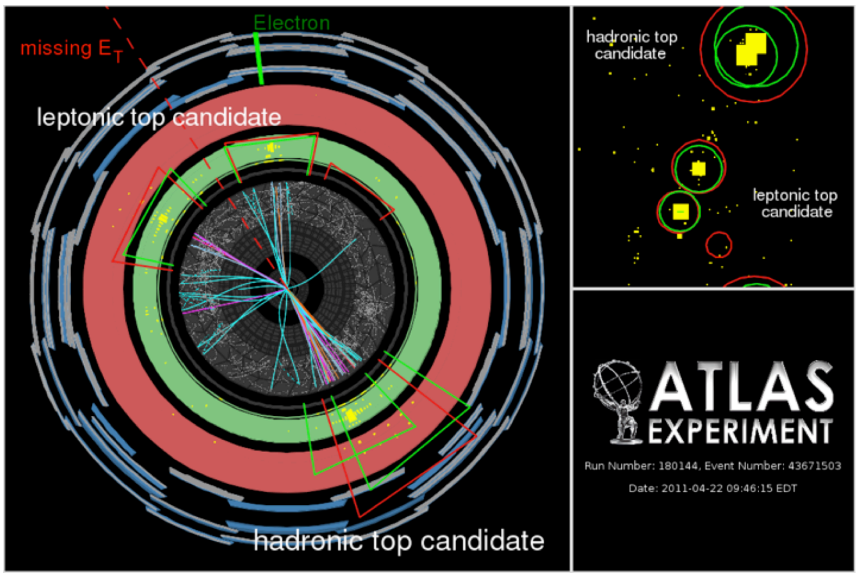

Figure 4.2.: A $t\bar{t}$ candidate event in the ATLAS event display is presented. The left panel displays a transverse view of the charged particle tracks and calorimeter energy deposits. In the upper part of the panel, a leptonic top quark candidate formed by an electron identified as the orange upward-pointing track associated to the green cluster around 12 o'clock, missing transverse momentum presented as a red dashed line at 11 o'clock, and a jet corresponding to the b-quark at 10 o'clock. In the lower part of the panel a hadronic top quark candidate formed by three jets is identified at 5 o'clock [86].

fit via the χ^2 technique to obtain the final track parameters [87].

The magnet systems bend the path of charged particles. The circular trajectory of the projected track into the transverse plane can be uniquely described by three parameters: the transverse momentum, p_{T}, the transverse impact parameter d_0 and the azimuthal angle, ϕ_0, which are described via Figure 4.3.

The high rate of collisions increases the amount of extra collisions in addition to the collision of interest which in turn increases the ID occupancy and an increased rate of fake tracks. However, ATLAS developed a robust track reconstruction configuration using more stringent hit requirements [88].

The ATLAS primary vertex reconstruction [89] uses the reconstructed track's data via

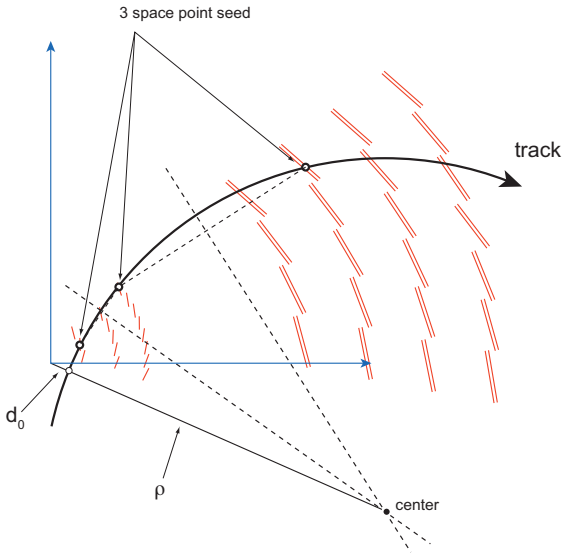

Figure 4.3.: A sketch of the technique used to estimate the track parameters of the seeds.

an iterative algorithm in a χ^2-based vertex fit. The primary vertex spatial resolution is measured to be ~ 23 μm in the transverse plane and ~ 40 μ along the beam axis. The vertex reconstruction efficiency is about 95% for non-diffractive events.

4.2. Electrons

The electron as a charged lepton of the first generation in the family of leptons, typically leaves a track in the ID, develops an Electro-Magnetic (EM) shower in the ECal (and to a lesser extent, in the HCal) through its interaction with the lead absorbers. Thus, it is absorbed by losing its entire energy in the calorimeter systems. Hence, the combination of the data from the ID and the calorimeter systems is used to identify and measure the energy of the electron candidate. The electron candidates [90] are reconstructed from energy deposits (clusters) in the ECal that are associated to reconstructed tracks in the ID. They are required to have $p_{\mathrm{T}} > 25$ GeV and $|\eta_{\mathrm{cluster}}| < 2.47$ (where $|\eta_{\mathrm{cluster}}|$ is the pseudorapidity of the calorimeter cluster associated with the electron candidate). Due to the low reconstruction efficiency and poor resolution, candidates in the calorimetry transition region between barrel and end-cap (*crack region*), $1.37 < |\eta_{\mathrm{cluster}}| < 1.52$, are excluded.

A cut-based classification using information of both ID and calorimeter systems is

utilised for electron selection and the rejection of jets misidentified as electrons. In this analysis, three classification types of *loose*, *medium* and *tight* are used, in which the *tight* selection is a subset of *medium* and *loose*, and *medium* is a subset of *loose*. With increasing tightness, the selection efficiency decreases while the purity increases. Figure 4.4 compares the efficiency of different classification types as a function of the number of reconstructed primary vertices measured in the 2011 and 2012 data. The efficiency variation below 4% from 1 to 30 vertices in 2012 data measurement shows the robustness of the reconstruction algorithm developed for 8 TeV data. In this analysis, all candidate electrons are required to pass the `tight++`[1] ID requirement.

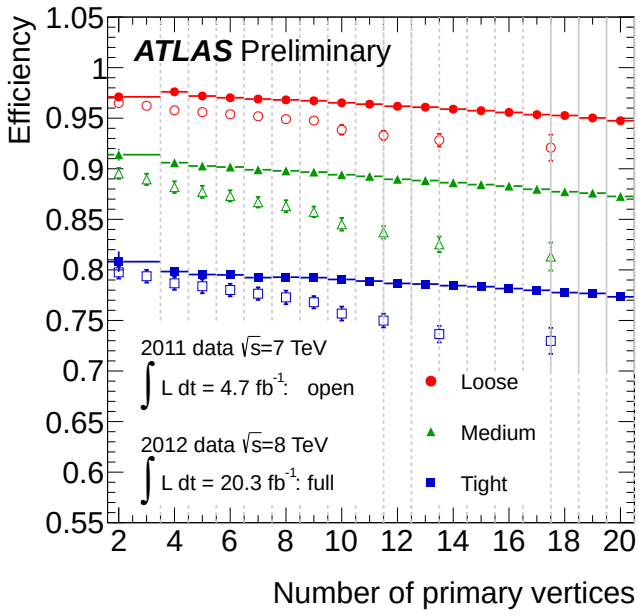

Figure 4.4.: Identification efficiency in data for the various cut-based selections measured with 2011 and 2012 data as a function of the number of reconstructed primary vertices [91].

In order to reduce the background from non-prompt electrons, i.e. from decays of hadrons (including heavy flavour) produced in jets, electron candidates are also required to be isolated. Two different η -dependent isolation criteria are applied. First is the sum

[1] In 2011, the performance of the classification was improved by loosening cuts on existing variables and introducing additional variables. In addition, in 2012 due to higher instantaneous luminosity and higher pile-up condition the cuts on the sensitive variables to the pile-up effect are loosened, while being tightened on the others, in order to keep the effect/background rejection roughly constant. Therefore the classification types are updated accordingly as ++ version of the original types.

of all tracks with transverse momentum, $p_{\mathrm{T}} > 400$ MeV, around the electron within a cone of radius $\Delta R \equiv \sqrt{(\Delta\eta)^2 + (\Delta\phi)^2} = 0.3$ referred to as `PtCone30`, in the ID. The second is the transverse energy deposited around the calorimeter cells associated to the electron, within a cone of radius $\Delta R = 0.2$ referred to as `EtCone20`. The sum of energy deposited around the cells corresponding to the electron cluster is corrected for leakage from the electron cluster itself. In each isolation criterion, the electron contribution is excluded from the cone. The transverse energy is defined with respect to the cluster energy and pseudorapidity as:

$$E_T = \frac{E_{\mathrm{cluster}}}{\cosh \eta_{\mathrm{track}}}. \tag{4.1}$$

These criteria are optimised to achieve a uniform isolation efficiency of 90%, independent of the electron p_{T}. The efficiency is estimated via a *tag-and-probe* method [91]. Lastly, the longitudinal impact parameter of the electron track with respect to the selected event primary vertex, z_0, is required to be less than 2 mm.

A calibration scheme via a multivariate algorithm based on the full detector simulation is used to correct (calibrate) the cluster energy of the electron. The correction is performed to account for the energy lost in the material upstream of the calorimeter, the energy leakage to the neighbouring cells around the main cluster and the energy lost beyond ECal. Details about the electron energy calibration methods are given in [92].

4.3. Muons

As a charged lepton of the second generation in the lepton family, the muon leaves a track in the ID. Unlike the electron, it acts as a minimum ionizing particle. Thus, a muon deposits a tiny fraction of its energy in both ECal and HCal and reaches the Muon Spectrometer, to leave a track in the outer part of the detector.

The reconstruction of muon candidates is based on the track segments of the muon spectrometer and the reconstructed tracks in the ID. At first, the tracks in the MS are reconstructed by scanning the chambers for local track segments and combining information of all layers. The muon track is obtained when a MS track matches a reconstructed track in the ID via a global fit. The final candidates are required to satisfy $p_{\mathrm{T}} > 25$ GeV and $|\eta| < 2.5$. They are referred to as *combined* muons, which are used in this analysis. The algorithm for combined muons exhibit the highest resolution and purity compared to the other reconstruction algorithms such as *Stand-Alone* (SA),

Segment-tagged (ST) and *Calorimeter-tagged* (CaloTag) muons, yields a reconstruction and identification efficiency of $\sim 99\%$, independent of η and p_{T}. The muon momentum scale and resolution are calibrated using data from $Z \to \mu^+\mu^-$, $\Upsilon \to \mu^+\mu^-$ and $J/\psi \to \mu^+\mu^-$ decays via the tag-and-probe technique [93]. Figure 4.5 shows the reconstruction efficiency of various muon reconstruction algorithms as a function of p_{T} and η obtained for 2012 data.

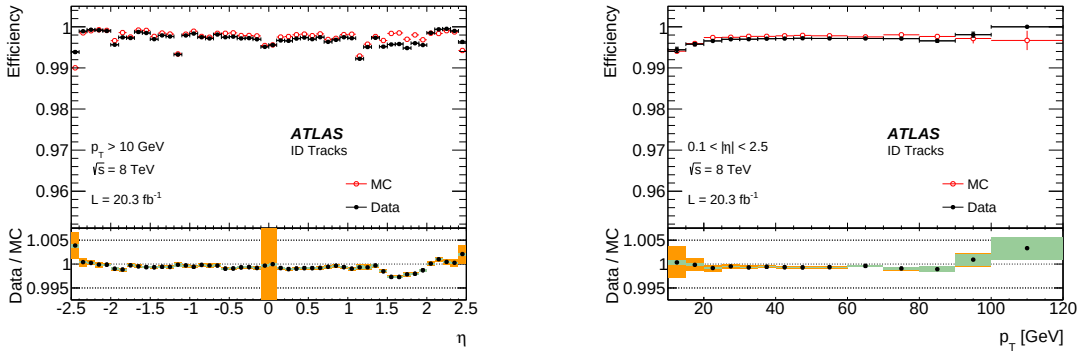

(a) (b)

Figure 4.5.: ID muon reconstruction efficiency as a function of η (a) and p_{T} (b) measured in $Z \to \mu^+\mu^-$ events for muons with $p_{\mathrm{T}} > 10$ GeV. The error bars on the efficiencies indicate the statistical uncertainty. The panel at the bottom shows the ratio between the measured and predicted efficiencies. The green areas depict the pure statistical uncertainty, while the orange areas also include systematic uncertainties [93].

Additionally, muons are required to satisfy a geometrical separation of $\Delta R > 0.4$ from any selected jet to reduce background from non-prompt muons. A $\sim 97\%$ efficient p_{T}-dependent track-based isolation requirement is also applied as a scalar sum of the track p_{T} in a cone of variable radius $\Delta R < 10\ \mathrm{GeV}/p_{\mathrm{T}}^{\mu}$ around the muon (excluding the muon track itself), which must be less than 5% of the muon p_{T} [94]. The muon hit pattern in the Inner Detector has to be consistent with a well-reconstructed track. Analogous to the electrons, the longitudinal impact parameter of the muon track with respect to the primary vertex, z_0, is required to be less than 2 mm.

4.4. τ-leptons

As the charged lepton of the third generation in leptons family, the τ-lepton has a short lifetime of $\sim 2.9 \times 10^{-13}$ seconds, which is way shorter than the time required to traverse the detector. Thus it is not considered as a final state particle. τ-leptons decay either hadronically into pion(s)/kaon(s) and a τ-neutrino in approximately 65% of the time, or leptonically as $\tau \to e\bar{\nu_e}\nu_\tau$ or $\tau \to \mu\bar{\nu_\mu}\nu_\tau$ in about 35% of time (See Table 2.1).

In this analysis, the τ-leptons are not reconstructed, but the leptonically decaying τ-lepton is considered in the signal events since it has same final state signature as of the decay of the W boson into electron or muon.

4.5. Jets

Jets are collimated streams of energetic hadrons and other particles produced by the hadronization of quarks or gluons, which are the dominant final state objects in the high energy hadron collisions. Jets are key ingredients in the analysis of many physics processes at the LHC. The produced particles leave tracks in the ID and deposit energy in ECal and HCal depending on the particle's type and energy. This collimated energy is reconstructed via various techniques and identified as jet. Different jet types depend on the various objects used as inputs into the reconstruction. Typically they are categorized as:

- particle (truth) jets: reconstructed via Monte Carlo (MC) truth stable particles[2],
- track-jets: reconstructed particle tracks in the ID which originate from the primary vertex,
- topo-clusters: reconstructed by using topological calorimeter clusters, and
- calorimeter-tower jets: built from calorimeter towers[3].

In this analysis, the jets are reconstructed from groups of calorimeter cells known as topological clusters [71], via the energy deposition in the calorimeter systems. Firstly, the algorithm finds a seed cell that contains a significant signal above noise which is required to be $S/N \geq 4$. Then it scans the surrounding volume for other cells with $S/N \geq 2$ and

[2]Final state particles with life time longer than 10 ps, excluding muons and neutrinos.
[3]The calorimeter is segmented into towers that are read-out independently. Each tower has an ECal followed by an HCal calorimeter.

adds them to the developing cluster. In addition to the electronic noise, the effect from pile-up jets is also considered as another source of noise, which is significantly larger than the electronic noise in the forward region of the calorimeter and comparable or smaller in the other regions.

Prior to jet reconstruction, the topo-clusters have to be calibrated. The first calibration stage is called EM scale, where the energy deposition due to the electromagnetic particle showers is considered. In this stage the energy is corrected for *in-time* and *out-of-time* pile-up effects as well as for an η-dependence due to inhomogeneous detector instrumentation. Secondly, the calorimeter response to hadrons is corrected via a local topo-cluster weighting (LCW) calibration scheme [95, 96], which is applied to correct the topological cluster energies for the effects of non-compensation, dead material and out-of-cluster leakage. The corrections are obtained from simulations of charged and neutral particles.

Finally, jets are reconstructed using a jet clustering algorithm. The commonly used algorithm in ATLAS is the anti-k_t algorithm [97–99] with a radius parameter $R = 0.4$. In brief, the algorithm calculates the distance d_{ij} between the clusters i and j and recombines them if $d_{ij} \leq R$ via the four-momentum sum to produce massive jets. The distance between two clusters is defined as:

$$d_{ij} = min(p_{T,i}^{2p}, p_{T,j}^{2p}) \frac{\Delta R_{ij}^2}{R^2}, \qquad \Delta R_{ij} = \sqrt{(y_i - y_j)^2 + (\phi_i - \phi_j)^2}, \tag{4.2}$$

where y represents the cluster's rapidity and p is the algorithm parameter which is equal to -1 for anti-k_t algorithm [97]. This algorithm results in almost perfect circular jets with radius R around the hardest cluster. Therefore, the soft clusters (particles) do not modify the shape of the jet, i.e. it satisfies the *infra-red and collinear safety* (IRC) condition [100]. Figure 4.6 displays the anti-k_t algorithm graphically.

Given that the reconstructed jet contains hadrons, the jet energy has to be calibrated to the hadronic scale. Monte Carlo simulations are used to estimate the jet energy scale (JES) via calculating the jet response as $R_{\mathrm{EM}}^{\mathrm{jet}} = E_{\mathrm{EM}}^{\mathrm{jet}} / E_{\mathrm{truth}}^{\mathrm{jet}}$ as function of jet p_{T} and η. This calibration level is known as *EM+JES calibration* [101]. Figure 4.7 shows the average energy response which is the inverse of the jet energy scale calibration as a function of η.

Finally, a further calibration is derived using in-situ techniques and is applied only to data [102].

After energy calibration, jets are required to have $p_{\mathrm{T}} > 25$ GeV and $|\eta| < 2.5$. During

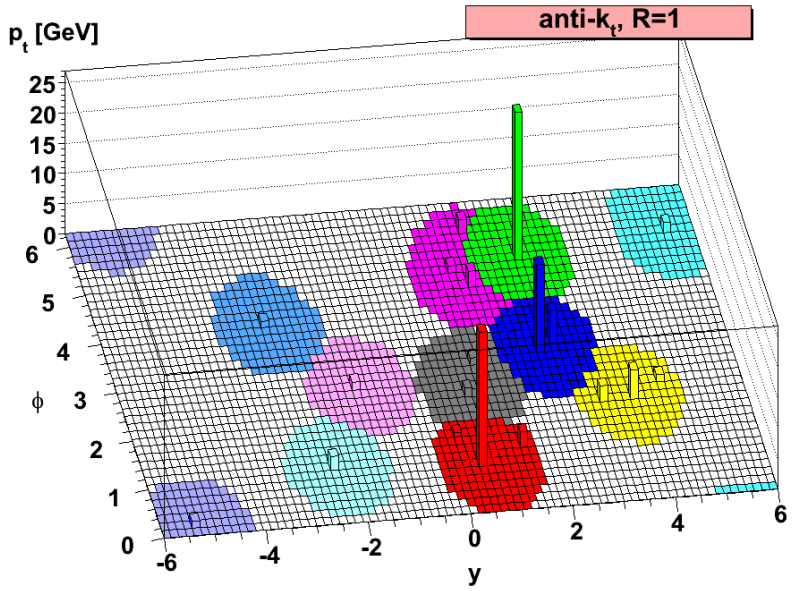

Figure 4.6.: A sample parton-level event with many random soft emissions, clustered with the anti-k_t algorithm [97].

jet reconstruction, no distinction is made between identified electrons and jet energy deposits. For jets within $\Delta R < 0.2$ of selected electrons, the single closest jet is discarded to avoid double-counting of electrons as jets. After this removal procedure, electrons within $\Delta R < 0.4$ of all remaining jets are removed.

To avoid selecting jets from secondary pp interactions, a selection on the so-called *jet vertex fraction* (JVF) variable (See section 4.5.1) above 0.5 is applied to jets with $p_{\mathrm{T}} < 50$ GeV and $|\eta| < 2.4$. This requirement ensures that at least 50% of the sum of the p_{T} of tracks with $p_{\mathrm{T}} > 1$ GeV associated with a jet comes from tracks compatible with originating from the primary vertex.

Jets are identified as originating from the hadronization of a b-quark (b-tagged) via an algorithm using multivariate techniques [103] to combine information from the impact parameters of displaced tracks as well as topological properties of secondary and tertiary decay vertices reconstructed within the jet (see Section 4.5.2). The working point used for this search corresponds to 70% efficiency to tag a b-quark jet, with a light jet rejection factor of ∼130 and a charm jet rejection factor of 5, as determined for b-tagged jets with $p_{\mathrm{T}} > 20$ GeV and $|\eta| < 2.5$ in simulated $t\bar{t}$ events. The simulated b-tagging

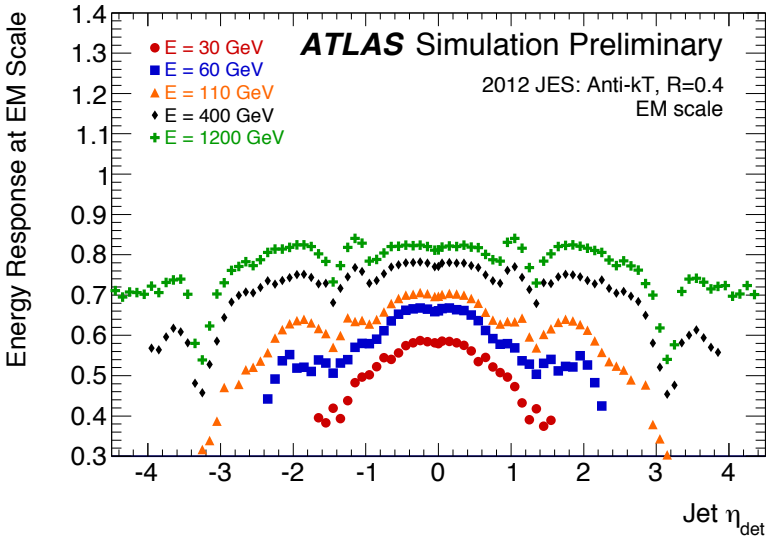

Figure 4.7.: Energy response as a function of η_{det} (the η of the jet relative to the geometric centre of the detector for EM scale anti-k_t R=0.4 jets before calibration [101].

efficiency is corrected to that measured in data using a $t\bar{t}$ PDF[4] calibration method [104]. This calibration uses a combinatorial likelihood to measure b-tagging efficiency in a data sample of dileptonic $t\bar{t}$ events and helps to reduce b-tagging uncertainties by considering correlations between the measured jets.

4.5.1. Jet Vertex Fraction

The additional pp interactions within one bunch crossing (in-time) and within the next or previous bunch crossing (out-of-time) pile-up have a strong effect on the measurement of the jet energy and the missing transverse momentum. Therefore, it is crucial to decrease this effect by proper cuts on the pile-up jets and/or estimate this contribution and apply proper corrections on the measured object's properties. The *Jet Vertex Fraction* (JVF) is a variable that quantifies the probability for each jet to come from a specific vertex [105]. Figure 4.8 sketches an example of two jets with different vertex origins, where a track originating from one jet contributes to the reconstruction of the other jet.

[4]Probability Density Function for the b-tagging discriminant

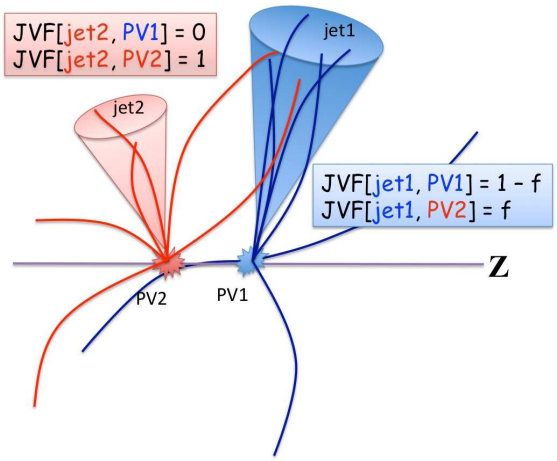

Figure 4.8.: Schematic representation of the JVF definition.

To calculate the JVF probability, a cone of ΔR =0.4 around each jet is defined,

$$\mathrm{JVF}(\mathrm{jet}_i, \mathrm{PV}_j) = \frac{\sum_k p_\mathrm{T}(\mathrm{track}_k^{\mathrm{jet}_i}, \mathrm{PV}_j)}{\sum_n \sum_l p_\mathrm{T}(\mathrm{track}_l^{\mathrm{jet}_i}, \mathrm{PV}_n)}, \tag{4.3}$$

where k runs over all tracks originating from PV_i that are matched to the jet_i, n represents all primary vertices in the event, while l runs over all tracks originating from PV_n that are matched to the jet_i. Only those with $p_\mathrm{T} > 500$ MeV are considered in this calculation. However, the JVF could be defined for any jet, it is calculated with respect to the event hard-scatter vertex[5] and can be used to select jets that most likely originate from that vertex.

The JVF distributions for hard-scatter jets and the jets originating from pile-up are compared in Figure 4.9. JVF=0(1) corresponds to a jet with all tracks originating from pile-up vertices (hard-scatter primary vertex), while JVF=-1 is assigned to calorimeter jets without associated tracks.

4.5.2. *b*-flavour Identification

The identification of jets originating from b-quark is known as b-tagging. It is an important task for a multitude of physics analyses, such as top-quark precision measurements and the measurements of the Higgs boson. The final state of the presented analysis

[5]It is the primary vertex with the highest $\sum_{\mathrm{tracks}}(p_T)^2$, which is measured to be correct in 98% of time in $Z(\rightarrow \ell^+\ell^-)$+1-jet events [105].

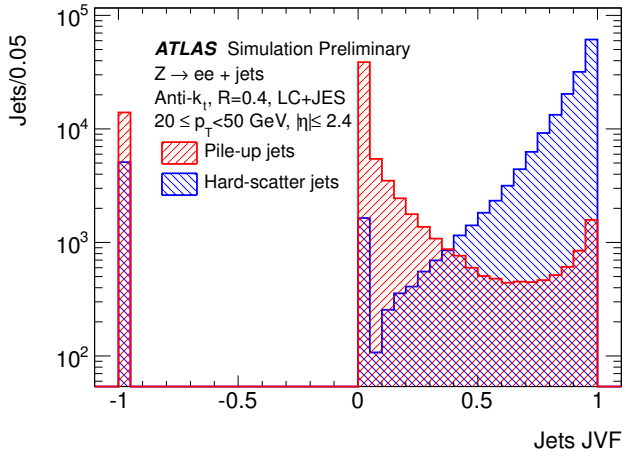

Figure 4.9.: JVF distributions for hard-scatter (blue) and pile-up (red) jets with $20 \leq p_{\mathrm{T}} < 50$ GeV and $|\eta| < 2.5$ in simulated Z+jets events. Using JVF directly as a discriminating variable provides a way to separate both classes of jets [105].

contains two b-quarks from the decay of the top quarks. The b-jet identification in this analysis is of paramount importance and helps to reduce the combinatorial backgrounds and increases the purity of the selected sample.

The hadrons containing a b-quark have a lifetime of $\mathcal{O}(1$ ps) [56], which is a sufficient time for them to travel some distance from the primary vertex (about 0.5 mm), forming a secondary decay vertex. The other feature of the B-hadrons is that the b-quark is much more massive than anything it decays into. Thus, its decay products have higher transverse momenta[6] compared to other light-quark jets, which leads to a wider jet. These features of the b-jet are sketched in Figure 4.10.

In this regard, various algorithms such as `SV1`, `IP3D` and `JetFitter` [106] developed using different techniques, which are mainly based on the reconstruction of the secondary vertex or the presence of tracks with large impact parameters, or utilisation of multivariate discriminants to make maximal use of the available information. The b-tagging algorithms provide *b-tag weights* (1–D discriminants) for all jets, where typically a higher b-tag weight indicates a larger probability that the jet originates from a b-quark. Therefore, the cut on this value is associated with purity and efficiency, which refer to the fraction of true b-tagged jets in the selected sample and the probability of tagging a

[6] Transverse momentum with respect to the b-quark direction. It should not be mixed up with the typical transverse momentum which is measured with respect to the beam axis.

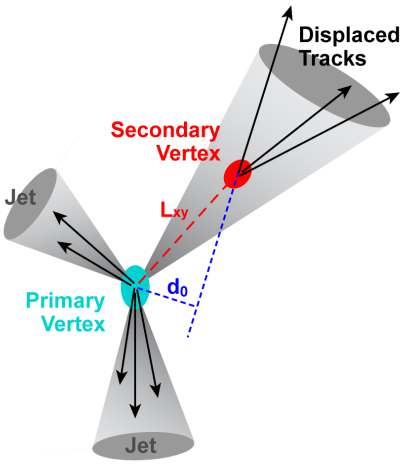

Figure 4.10.: b-jet identification using secondary vertex reconstruction technique.

true b-jet, respectively.

The most typical b-tagging algorithm used in ATLAS is the multivariate algorithm MV1 [107], which combines the output weights of the `JetFitter`, `IP3D` and `SV1` algorithms in a neural network. Figure 4.11 presents a study performed with 7 TeV data, showing the light-jet and c-jet rejection as a function of b-jet efficiency, for different b-tagging algorithms. The MV1 algorithm provides the best light-jet rejection. The 70% working point corresponding to 70% b-tagging efficiency is chosen for this analysis. It provides a light-jet (c-jet) rejection factor of ∼130 (5).

In order to reduce the discrepancy between the Monte Carlo and data, the efficiencies for b-tagging, c-tagging and mistag rate are calibrated via enriched data samples in b-jets, c-jets and light-jets respectively [107–109]. A $t\bar{t}$ data sample in the dilepton channel is used for b-jet calibration. The results are obtained as scale factors (SFs) as shown in Figure 4.12.

4.6. Missing Transverse Momentum

The transverse component of the total transverse momentum of the colliding protons is assumed to be equal to zero. Thus, the vector sum of the transverse momenta of the final state particles is expected to be equal to zero, by momentum conservation. The undetectable particles such as neutrinos in the final state lead to an imbalance of the vectorial momentum sum in the transverse plane with respect to the beam axis. Hence

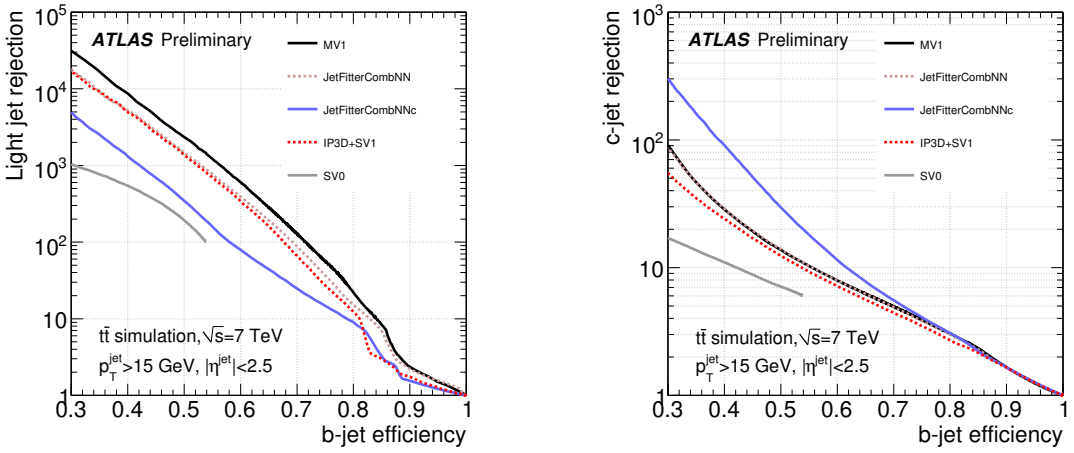

(a) (b)

Figure 4.11.: Light-jet (a) and c-jetp_{T} (b) rejection as a function of the b-tag efficiency for the b-tagging algorithms calibrated based on simulated $t\bar{t}$ events [107].

those particles can be detected (reconstructed) indirectly via the conservation laws.

The $E_{\mathrm{T}}^{\mathrm{miss}}$ is obtained from the negative vectorial sum of all final state reconstructed and calibrated objects in the collision, by taking the muon momenta and the unassociated objects into account. In this analysis, the missing transverse momentum ($E_{\mathrm{T}}^{\mathrm{miss}}$) is used to estimate the transverse momentum of a neutrino originating from the decay of the W boson in the $t\bar{t}$ final state.

There are several issues needed to be considered in the $E_{\mathrm{T}}^{\mathrm{miss}}$ reconstruction, such as dead regions of the calorimeter, noise and existence of particles from cosmic-rays (basically muons). Track information is used in order to estimate the low-p_{T} particles that are missed in the calorimeter systems. The $E_{\mathrm{T}}^{\mathrm{miss}}$ is reconstructed by first matching each calorimeter energy cluster with either a reconstructed lepton or jet. The energy depositions not associated with any of those objects are considered as unassociated (*Cell-Out term*) cells [110]. The remaining unassociated clusters are then calibrated for energy losses in un-instrumented regions and for different responses of the calorimeters to electromagnetic and hadronic shower components. This calibration scheme is similar to that

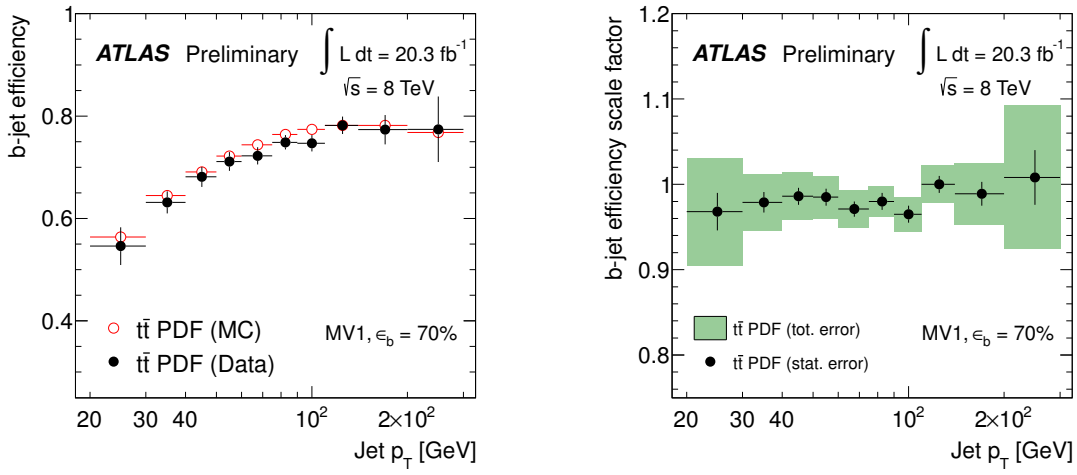

(a) (b)

Figure 4.12.: The (a) b-jet efficiencies and (b) b-jet efficiency scale factors obtained from the combination of the four channels ($e\mu$ and $e^+e^-/\mu^+\mu^-$ channels in the two- and three-jet bins) for the MV1 b-tagging tool at the 70% b-jet efficiency working point. For (a) the error bars on the data points represent the total statistical and systematic uncertainties. For (b) both statistical only (black lines) and total errors (green shaded region) are shown [104].

described in Ref. [111]. Therefore, the x- and y- components of the $E_{\mathrm{T}}^{\mathrm{miss}}$ are defined as:

$$E_{x(y)}^{\mathrm{miss}} = E_{x(y)}^{\mathrm{miss,\ electron}} + E_{x(y)}^{\mathrm{miss,\ jets}} + E_{x(y)}^{\mathrm{miss,softjets}} + E_{x(y)}^{\mathrm{miss}\ ,\mu} + E_{x(y)}^{\mathrm{miss,\ Cell\text{-}Out}}, \tag{4.4}$$

where the additional *softjets* term refers to a contribution from jets with $p_{\mathrm{T}} < 20$ GeV.

The magnitude of the transverse momentum would be:

$$E_{\mathrm{T}}^{\mathrm{miss}} = \sqrt{(E_x^{\mathrm{miss}})^2 + (E_y^{\mathrm{miss}})^2}. \tag{4.5}$$

The muon typically traverses the detector and leaves a minimum ionising energy in the calorimeter systems. For isolated muons (see Section 4.3) this energy is added to the Cell-Out term, otherwise, it is added to the jets term.

5 Data Sample, Signal and Background Modelling

In order to carry out a successful discovery or a precision measurement analysis, it is essential to compare the analysed data with a simulation based on the best understanding of the physics processes of the signal and background events and the detector response.

In this chapter, at first, the 2012 data and the corresponding data taking conditions are briefly discussed. The concepts of event simulation as well as the Monte Carlo samples used for simulating the signal and background processes follow. Controlling and modelling of background processes such as multijet processes with jets misidentified as leptons or non-prompt leptons from hadron decays are accompanied by theoretical and technical difficulties. Therefore, a brief introduction to the *Matrix Method* as a data-driven approach to estimate such backgrounds is given before closing this chapter.

5.1. Event Simulation

The full simulation of a hadron-hadron collision can be divided into several definite stages by applying the factorisation theorem (see Section 2.1.2). These stages are sketched in Figure 5.1 and summarised as the following:

- **Hard Collision (Scattering)**: indicated as a red blob, it is the primary interaction between the partons which obeys the perturbative calculation, based on a *matrix element*, and describes the physics process. Any event simulation starts with the computation of the hard scattering cross section at a given order in perturbation theory. POWHEG [112–114] and SHERPA [115] are typical event generators used frequently in ATLAS and the former is the chosen generator for the $t\bar{t}$ signal events in this thesis.

- **Parton Showers**: are process independent higher-order real-emission corrections to the hard scattering. In this stage, the created coloured partons are linked to colour-neutral hadrons (represented by light green blobs). PYTHIA [116], HERWIG [117] and SHERPA are the most typical parton shower MC event generators.
- **Hadronisation**: known also as jet fragmentation, is the transformation of partons in the shower into colour-neutral final state particles (indicated as dark green blob). This process suffers from frame dependence and collinear unsafety. String and cluster models are the two most typical hadronisation models used today [118], which are implemented by PYTHIA and HERWIG respectively.
- **Underlying Event**: The remnant partons of the colliding hadrons which do not contribute to the main hard scattering may produce secondary hard or semi-hard interactions (indicated as a purple blob). It is the effect of re-scattering and the exchange of multiple partons between the initial state protons. These processes are described by phenomenological models.
- **Soft Photon Radiation**: known also as QED Bremsstrahlung, occurs at any stage (shown via yellow lines).

Finally, the interaction of particles with the detector is simulated via the GEANT4 toolkit [119]. In the final stage of an event simulation, the event is processed through the same reconstruction software as the data.

5.2. Data Sample

The data analysed for the W boson helicity measurement was collected during the LHC Run I by the ATLAS detector in 2012 at a centre-of-mass energy of $\sqrt{s} = 8$ TeV. As illustrated in Figure 3.9a, a total amount of 22.8 fb^{-1} of data was delivered by the LHC, 21.3 fb^{-1} of which was recorded by ATLAS. An amount of 20.2 fb^{-1} ($\sim 95\%$) of the recorded data fulfilled the quality criteria corresponding to fully operational detector and stable beam conditions are used in this analysis. The data was collected with a bunch spacing of 50 ns and a maximum number of bunches per beam of 1380.

The recorded data is divided into several periods, referring to definite time intervals, depending on different detector and beam conditions. The first quality control is performed online at the time of data taking via the *data quality monitoring* shifter in the ATLAS control room [120]. At this stage, an automatic system called *Data Quality Monitoring Framework* (DQMF) checks about 50,000 online histograms every few minutes and an

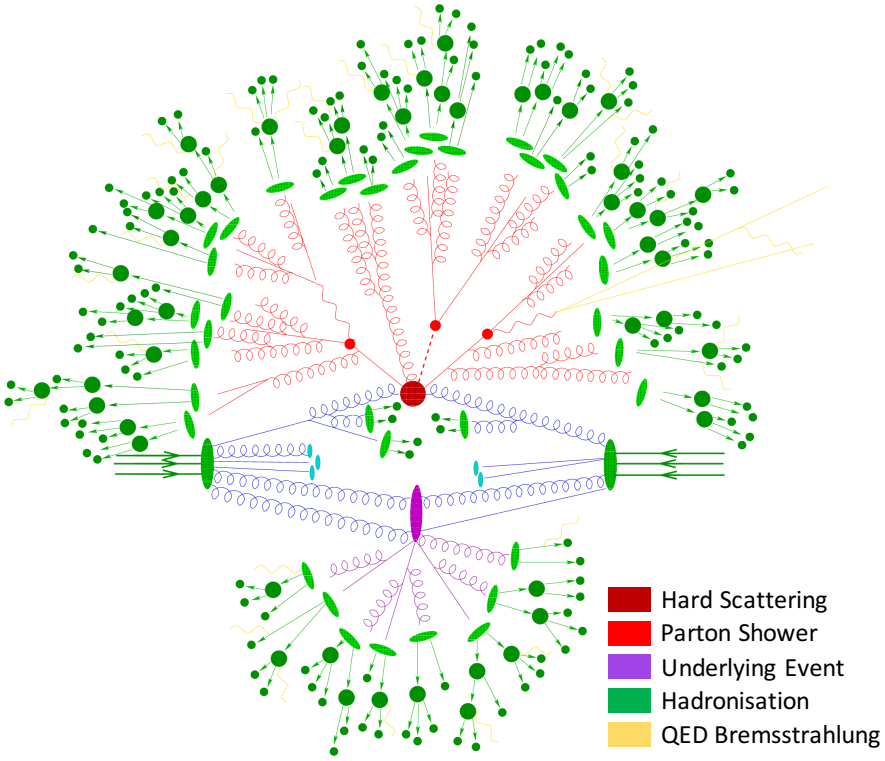

Figure 5.1.: Sketch of a hadron-hadron collision as simulated by a Monte-Carlo event generator. (Online version in colour)

automatic Data Quality (DQ) assessment is made per histogram (DQ result) [121]. The shifter also periodically checks the luminosity and beam conditions, trigger rates, data acquisition and processing chain, and documents every alarm, error or issue for further evaluation. After calibration and additional checks by each detector expert offline, the data qualified for physics analysis is collected in the so-called *Good Run List* (GRL).

5.3. Signal Monte Carlo Samples

The signal sample of $t\bar{t}$ is generated using the POWHEG-BOX NLO event generator [112–114] with the CT10 Parton Distribution Functions (PDF) set [122]. The event generator is interfaced to PYTHIA 6.425 [116] (referred to as the POWHEG+PYTHIA sample) to model the showering and hadronisation, with the CTEQ6L1 PDF set [123]. In addition, a set of tuned parameters called the PERUGIA2011C tune [124] is applied for the modelling of the underlying event. The model parameter h_{damp} is set to the top quark mass

(m_t), which controls the matrix element to parton shower matching in POWHEG-BOX and effectively regulates the amount of high-p_{T} radiation.

The generated sample is normalised to the theoretical cross section calculation performed at NNLO in QCD that includes resummation of NNLL soft gluon terms with `top++2.0` [44–49] yielding $\sigma(t\bar{t}) = 253^{+13}_{-15}$ pb for $\sqrt{s} = 8$ TeV.

Alternative signal samples with different event generators, parton showers and normalisation and factorisation scales are considered to assess the impact of those choices on the measurement. Details about the alternative samples and the uncertainty estimation procedure are given in Section 8.2.4.

5.4. Background Monte Carlo Samples

Selected $t\bar{t}$ events in the lepton+jets channel are accompanied by several background processes that need to be taken into account in the analysis.

W/Z+jets

The production of a W boson with additional jets, where the W boson decays into a charged lepton and its corresponding neutrino, mimics the final state of the signal event. It is considered as the dominant background process for $t\bar{t}$ events. Similarly, the production of the Z boson with additional jets, where the Z boson decays into two charged leptons, can fake the signal event, in case one lepton fails the reconstruction or selection criteria.

Events with a W or Z boson produced in association with jets are generated at $\sqrt{s} = 8$ TeV using the ALPGEN v2.14 [125] Leading Order (LO) generator and the CTEQ6L1 PDF set. Parton shower and fragmentation are modelled with PYTHIA 6.425 for W+jets and Z+jets production.

The W+jets samples are generated with up to five additional partons, separately for W+light jets, $Wb\bar{b}$+jets, $Wc\bar{c}$+jets, and Wc+jets. The overlap between $WQ\bar{Q}$ ($Q = b, c$) events generated from the matrix element calculation and those generated from parton-shower evolution in the W+light jet samples is avoided via an algorithm based on the angular separation between the extra heavy quarks: if $\Delta R(Q, \bar{Q}) > 0.4$, the matrix-element prediction is used, otherwise the parton-shower prediction is used. To avoid double-counting of partonic configurations generated by both the matrix-element calculation and the parton-shower evolution, a parton-jet matching scheme "MLM match-

Sample	Generator	PDF	Shower	Normalization
$t\bar{t}$ + jets	PowHeg	CT10	Pythia 6.425	NNLO+NNLL [138, 139]
W + jets	Alpgen	CTEQ6L1	Pythia 6.426	data-driven [140]
Z + jets	Alpgen	CTEQ6L1	Pythia 6.426	NLO [141]
Single top (s-channel, Wt)	PowHeg	CT10	Pythia 6.426	aNNLO [142–144]
Single top (t-channel)	PowHeg	CT10	Pythia 6.427	aNNLO [142–144]
Diboson	Sherpa	CT10	Sherpa	NLO [145]

Table 5.1.: A summary of basic generator parameters used to simulate various processes.

ing" [126] is employed.

In a similar manner, the Z+jets background is generated with up to five additional partons separated in different parton flavours and is normalised to the inclusive NNLO theoretical cross section [127].

Single top quark

Single top quark processes for the t-channel, s-channel and Wt associated production are also simulated with POWHEG-BOX [128, 129] using the CT10 PDF set. The samples are interfaced to PYTHIA 6.425 with the CTEQ6L1 PDF set and tune PERUGIA2011C for underlying events. Overlaps between the $t\bar{t}$ and Wt final states are removed [130]. The single top quark samples are normalised using the approximate NNLO theoretical cross-sections [131–133] calculated with the MSTW2008 NNLO PDF set [134, 135]. All $t\bar{t}$ and single top samples are generated assuming a top quark mass of 172.5 GeV, compatible with the ATLAS measurement of $m_t = 172.84 \pm 0.70$ GeV [136].

Diboson

Diboson samples ($WW/WZ/ZZ$+jets) are generated using the SHERPA event generator with the CT10 PDF set. The events are generated with massive b- and c-quarks and with up to three additional partons in the hard process and are normalised to their NLO theoretical cross sections [137].

Finally, all MC samples include multiple pp interactions to simulate the pile-up effect and are processed through a simulation of the detector geometry and response using GEANT4 toolkit. Simulated events are corrected so that the object identification efficiencies, energy scales and energy resolutions match those determined in data control samples. Table 5.1 provides a summary of basic parameters of the MC samples used in this analysis.

5.5. Data Driven Background Estimates

5.5.1. Misidentified Lepton Background

The lepton+jets channel criteria require exactly one isolated high-p_{T} electron or muon in the event's topology. The background sources mentioned in the previous section produce prompt leptons and can pass the selection criteria once accompanied by some jets in the final state.

One the other hand, in multijet processes, there are non-prompt leptons that originate from jets. The lepton isolation requirement is applied to reject the events with those non-prompt leptons, but in some cases they can pass the isolation criteria. The electron can also be faked by a photon or a neutral pion. The multijet processes have a high production cross section and are dominant in hadron collision experiments. Therefore, the *fake leptons* background estimation is of importance.

The MC simulation of the multijet processes has a very large uncertainty. Therefore, this source of background events is estimated using a data-driven approach, called "matrix method".

Matrix Method

The matrix method is based on the measurement of lepton selection efficiencies via two categories of events using *loose* and *tight* lepton selection requirements (see Section 4.2 and 4.3). The tight lepton selection is the same as the one used for the lepton selection in this analysis. The loose definition requires looser criteria in the lepton selection. Thus, the tight leptons are a subset of the loose ones. In each subset of selected data, both real and fake leptons exist. Therefore, one could write the number of leptons in each category as:

$$\begin{aligned} N^{loose} &= N^{\mathrm{loose}}_{\mathrm{real}} + N^{\mathrm{loose}}_{\mathrm{fake}}, \\ N^{tight} &= N^{\mathrm{tight}}_{\mathrm{real}} + N^{\mathrm{tight}}_{\mathrm{fake}}. \end{aligned} \tag{5.1}$$

The probabilities of a real lepton in the loose category to pass the tight criteria ($\varepsilon_{\mathrm{real}}$) and of a fake lepton in the loose category to pass the tight criteria ($\varepsilon_{\mathrm{fake}}$) are defined as:

$$\varepsilon_{\mathrm{real}} = \frac{N^{\mathrm{tight}}_{\mathrm{real}}}{N^{\mathrm{loose}}_{\mathrm{real}}}, \qquad \varepsilon_{\mathrm{fake}} = \frac{N^{\mathrm{tight}}_{\mathrm{fake}}}{N^{\mathrm{loose}}_{\mathrm{fake}}} \tag{5.2}$$

By substituting Equation 5.2 in 5.1, the number of fake leptons in the tight selection is obtained in terms of the real and fake efficiencies as:

$$N_{\text{fake}}^{\text{tight}} = \frac{\varepsilon_{\text{fake}}}{\varepsilon_{\text{real}} - \varepsilon_{\text{fake}}}(\varepsilon_{\text{real}} N^{\text{loose}} - N^{\text{tight}}), \tag{5.3}$$

where the $\varepsilon_{\text{real}}$ and $\varepsilon_{\text{fake}}$ are obtained for e+jets and μ+jets samples, individually. The $\varepsilon_{\text{real}}$ efficiencies are measured using the tag-and-probe method from the $Z \to e^+e^-$ and $Z \to \mu^+\mu^-$ control regions, while the $\varepsilon_{\text{fake}}$ efficiencies are measured in data samples dominated by non-prompt and fake lepton background events. The details of this efficiency measurement are given in [146].

The method of calculating those efficiencies implies that they depend on lepton kinematics and event characteristics. Hence, in order to correctly account for this, an event weight (ω_i) defined as in the following, is applied to the events:

$$\omega_i = \frac{\varepsilon_{\text{fake}}}{\varepsilon_{\text{fake}} - \varepsilon_{\text{real}}}(\varepsilon_{\text{real}} - \delta_i), \quad \text{where} \quad \delta_i = \begin{cases} 1 & \text{if event } i \text{ passes the tight selection} \\ 0 & \text{otherwise} \end{cases}. \tag{5.4}$$

Therefore, the misidentified lepton background estimate in a given bin of the final observable, which is the $\cos\theta^*$ in this analysis (see Section 2.2.3) is given by the sum of ω_i over all events in that bin.

5.5.2. W+jets Normalisation

The predictions of normalisation and flavour composition of the W+jets background are affected by large uncertainties. Thus, a data-driven technique is employed to estimate the inclusive normalisation and the heavy-flavour composition of the corresponding processes. The approach is based on the fact that the $W^{\pm}$ boson production is charge-asymmetric at a pp collider. The W boson charge asymmetry depends on the flavour composition of the sample. Thus, correction factors estimated from data are used to rescale the fractions of $Wb\bar{b}/c\bar{c}$+jets, Wc+jets and W+light jets events in the MC samples introduced in Section 5.4: $K_{bb} = K_{cc} = 1.50 \pm 0.11$ (stat. + syst.), $K_c = 1.07 \pm 0.27$ (stat. + syst.) and $K_{\text{light}} = 0.80 \pm 0.04$ (stat. + syst.). The method and factors are derived in [140].

6

Event Selection and Reconstruction

The characteristics of the event selection in the lepton+jets final state topology of the $t\bar{t}$ system is discussed in this chapter. The event selection aims at a reduction of the non-$t\bar{t}$ background processes that were discussed in the previous Chapter. The selection cuts are applied on both simulation and data, and the expected number of events is compared to the observation. To test the goodness of modelling the signal and background processes, the data/prediction distributions of several variables of interest are compared in Section 6.1.1.

In order to obtain the angular distribution of the lepton (down-type quark) in the W boson rest frame, and measure the W boson polarisation, the $t\bar{t}$ event must be fully reconstructed. Therefore, the kinematic likelihood fit as the chosen reconstruction method for this analysis is introduced in Section 6.2.1. The method used to differentiate between the decay products of the hadronically decaying W boson, i.e. the two light jets, is discussed in detail in Section 6.2.2. To increase the reconstruction efficiency, different jet input options to the reconstruction algorithm are considered. The study is summarised in Section 6.2.3. Finally, in addition to the standard selection cuts, a reconstruction quality criterion is studied to increase the purity of correctly reconstructed events. The details are given in 6.2.4.

6.1. Event Selection

The lepton+jets final state topology of the $t\bar{t}$ system is characterised by an isolated high-p_{T} electron or muon, at least four jets and missing transverse momentum due to the undetected neutrino. Events are selected from the data collected in stable beam

conditions which pass certain quality requirements, identified as qualified data for physics analysis and listed in the ATLAS 8 TeV Good Run List as discussed in Section 5.2. The corresponding integrated luminosity is 20.2 fb^{-1}.

The selected events are required to pass a single electron or muon trigger and to have at least one primary collision vertex with at least five associated tracks with $p_{\mathrm{T}} > 400$ MeV. If more than one primary vertex is reconstructed, the one with the largest scalar sum of transverse momenta is selected as the hard-scattering vertex. The event is discarded if any jet with $p_{\mathrm{T}} > 20$ GeV is independently identified as out-of-time pile-up from a previous pp collision or as calorimeter noise [147].

In order to select events from $t\bar{t}$ decays in the lepton+jets channel, events are required to have exactly one reconstructed electron or muon with $p_{\mathrm{T}} > 25$ GeV and at least four jets satisfying the quality and kinematic criteria discussed in Section 4.5. For both electron and muon channels, the selected lepton is required to match ($\Delta R < 0.15$) the lepton reconstructed by the high-level trigger. The selected events are separated into two orthogonal b-tag regions: one with exactly one b-tag and one with two or more b-tags. Therefore, the data sample is split into four channels with respect to the lepton flavour and the b-jet multiplicity: "e+jets, 1 b-tag", "e+jets, ≥ 2 b-tags", "μ+jets, 1 b-tag" and "μ+jets, ≥ 2 b-tags".

For events with one b-tag, $E_{\mathrm{T}}^{\mathrm{miss}}$ is required to be larger than 20 GeV and the sum of $E_{\mathrm{T}}^{\mathrm{miss}}$ and transverse mass of the leptonically decaying W boson, $m_T(W)$, is required to be larger than 60 GeV in order to suppress multijet background. For the higher b-tag multiplicity region the background from multijet production is very small. Thus, no requirements on the $E_{\mathrm{T}}^{\mathrm{miss}}$ or transverse mass of the W boson are applied for the inclusive region with 2 or more b-tags.

6.1.1. Data/Prediction Comparison

Event yields for both lepton channels and b-tag regions are shown in Table 6.1. Cutting on the log likelihood as a reconstruction quality criterion (discussed in Section 6.2.4) significantly reduces background contributions and improves the data/prediction agreement. Studies of the dependence of the sensitivity of the W boson helicity measurement on a likelihood cut are presented in Sec. 6.2.4.

Plots showing data/prediction comparisons after event selection and log likelihood cut for both lepton channels and b-tag regions are shown in Figures 6.1-6.4. A good agreement between the observation and prediction is obtained. Control plots for the prefit $\cos\theta^*$

e+jets	No LH Cut		log LH>-48	
Sample	1 b-tag	≥ 2 b-tags	1 b-tag	≥ 2 b-tags
$t\bar{t}$	69900 ± 4500	74500 ± 4800	36500 ± 2300	36000 ± 2300
Single top	5600 ± 900	3700 ± 630	200 ± 340	974 ± 170
W + light	2500 ± 130	100 ± 10	600 ± 30	24 ± 1
W + c	4500 ± 1100	270 ± 60	1210 ± 300	54 ± 13
W + bb/cc	12000 ± 800	2900 ± 130	2730 ± 190	538 ± 38
Z + jets	3850 ± 1800	1300 ± 620	1200 ± 580	330 ± 160
Diboson	800 ± 400	175 ± 85	220 ± 100	33 ± 16
Fake leptons	6900 ± 2000	2100 ± 600	2270 ± 680	450 ± 130
Total expected	105900 ± 5600	84900 ± 4900	46700 ± 2500	38400 ± 2300
Observed	102591	89414	45246	40045

μ+jets	No LH Cut		log LH>-48	
Sample	1 b-tag	≥ 2 b-tags	1 b-tag	≥ 2 b-tags
$t\bar{t}$	87400 ± 5600	92300 ± 6000	43600 ± 2803	42600 ± 2700
Single top	6700 ± 1100	4500 ± 760	2330 ± 400	1100 ± 190
W + light	3300 ± 200	180 ± 10	760 ± 40	45 ± 2
W + c	5600 ± 1400	330 ± 80	1440 ± 360	50 ± 10
W + bb/cc	16400 ± 1100	4100 ± 190	3520 ± 250	780 ± 55
Z + jets	2400 ± 1200	750 ± 360	610 ± 290	160 ± 75
Diboson	900 ± 450	200 ± 90	210 ± 100	40 ± 20
Fake leptons	5300 ± 1600	1500 ± 400	1750 ± 520	320 ± 100
Total expected	128000 ± 6400	103800 ± 6000	54200 ± 2900	45100 ± 2800
Observed	126333	108131	53747	46048

Table 6.1.: Event yields in the electron (top) and muon channel (bottom) with 1 b-tag and ≥ 2 b-tags after event selection. Uncertainties in the normalisation of each sample include systematic uncertainties for the data-driven backgrounds (W+jets and fake leptons) and theory uncertainties for the $t\bar{t}$ signal and the other background sources. The last two columns refer to the yields after applying the cut on the reconstruction likelihood. Details are given in Section 6.2.4

distributions obtained from both leptonic and hadronic analysers (see Section 2.2.5) are shown in Figure 6.5 for both $\geq$ 2 b-tags and 1 b-tag regions. The uncertainties on the prediction are given by considering the theoretical uncertainties on the calculated cross sections for the MC driven backgrounds and the normalisation uncertainty on the multijet background, in addition to the statistical uncertainties due to the limited number of events in the simulated samples.

The difference between the distributions of the leptonic and hadronic analysers in Figure 6.5 is caused by the fact that for the events with $\cos\theta^* \sim -1$, where the charged lepton (down-type quark) is emitted parallel to the b-jet, some events fail the selection criteria due to the lepton p_{T} and lepton isolation requirements. This affects the leptonic branch more than the hadronic one since in the latter the lepton is not used in the $\cos\theta^*$ construction. The other source of difference between the shapes is observed for the events with $\cos\theta^* \sim +1$ where the neutrino (up-type quark) and b-jet are parallel and emitted backward with respect to its mother particle, i.e. the W boson. Here the $E_{\mathrm{T}}^{\mathrm{miss}}$ cut causes some events to fail the selection criteria in the 1 b-tag region, but there is no such effect on the hadronic side. Finally, the hadronic distribution of $\cos\theta^*$ in the 1 b-tag region suffers from a mismatch of up/down-type quarks due to extra jet emission which results in the double peak structure.

6.2. Event Reconstruction

A correct assignment of the final state objects from the $t\bar{t}$ decay to the partons/lepton is necessary to measure the W boson helicity fractions. In this regard, a kinematic likelihood fit is used to determine the best association of b-jets, light jets, and a lepton candidate to the top quark and antiquark decay hypotheses, considering the momentum imbalance due to the undetected neutrino originating from the leptonically decaying W boson.

This section details the method of the kinematic fitting as well as its extensions that use information beyond object kinematics in order to produce the final jet assignments. A number of different jet input configurations are studied in order to determine the optimal setup to increase the reconstruction efficiency.

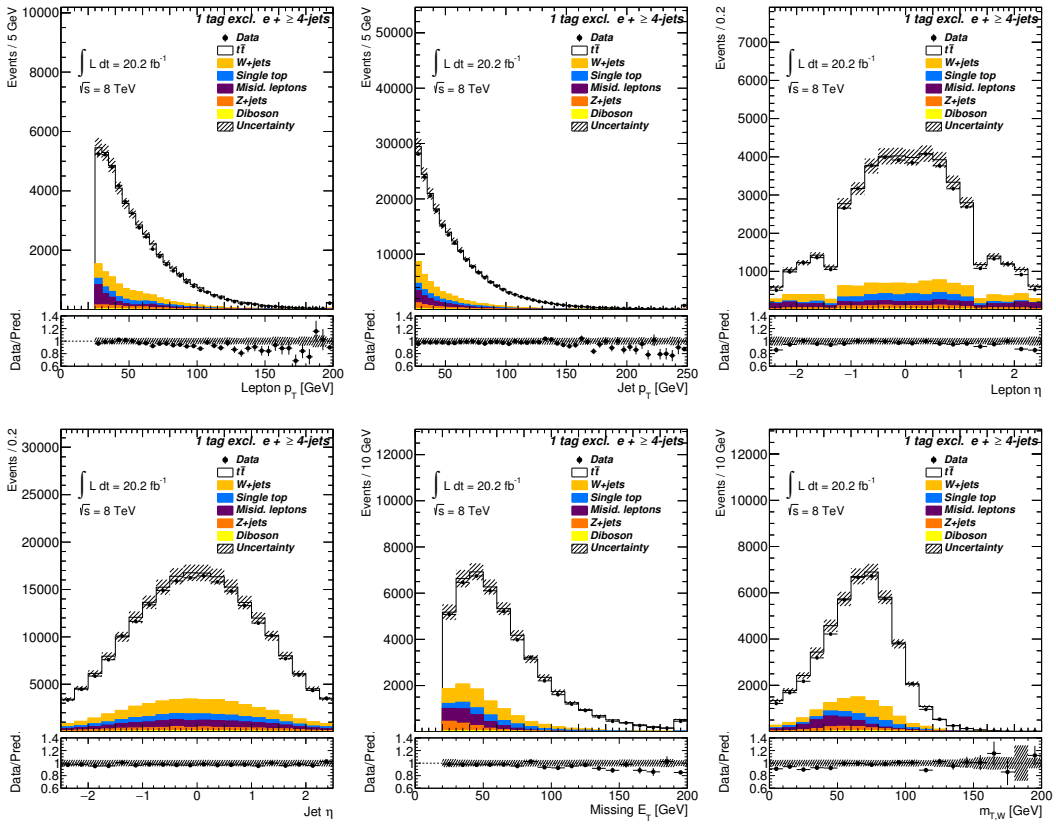

Figure 6.1.: Data/prediction comparison after event selection for reconstructed objects (lepton, jets, neutrino) in the electron channel with 1 b-tag. The displayed uncertainties represent the Monte Carlo statistical uncertainty as well as the background normalisation uncertainties.

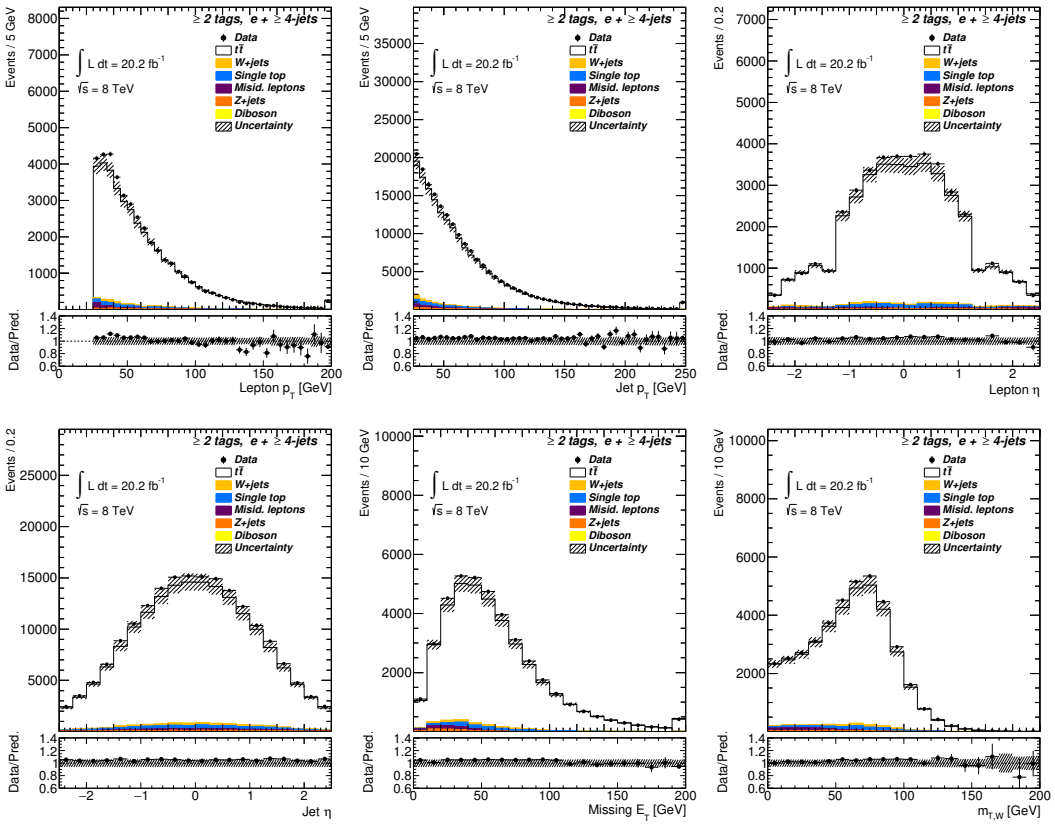

Figure 6.2.: Data/prediction comparison after event selection for reconstructed objects (lepton, jets, neutrino) in the electron channel with ≥ 2 b-tags. The displayed uncertainties represent the Monte Carlo statistical uncertainty as well as the background normalisation uncertainties.

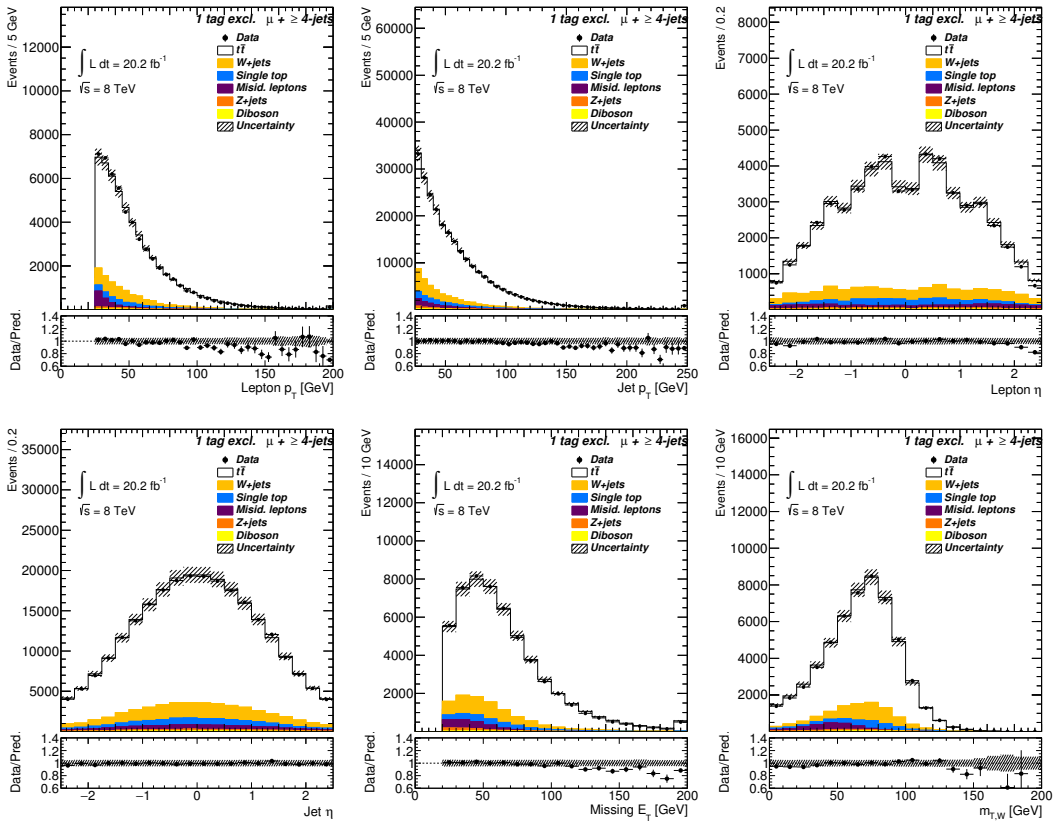

Figure 6.3.: Data/prediction comparison after event selection for reconstructed objects (lepton, jets, neutrino) in the muon channel with 1 b-tag. The displayed uncertainties represent the Monte Carlo statistical uncertainty as well as the background normalisation uncertainties.

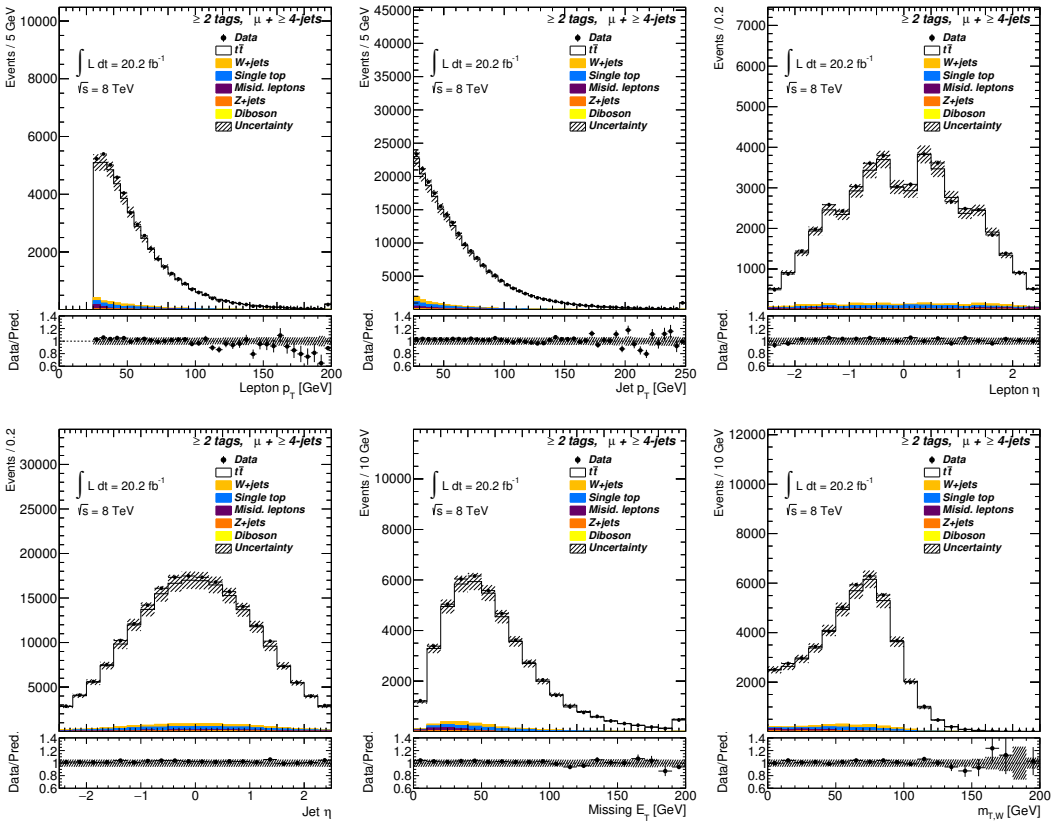

Figure 6.4.: Data/prediction comparison after event selection for reconstructed objects (lepton, jets, neutrino) in the muon channel with ≥ 2 b-tags. The displayed uncertainties represent the Monte Carlo statistical uncertainty as well as the background normalisation uncertainties.

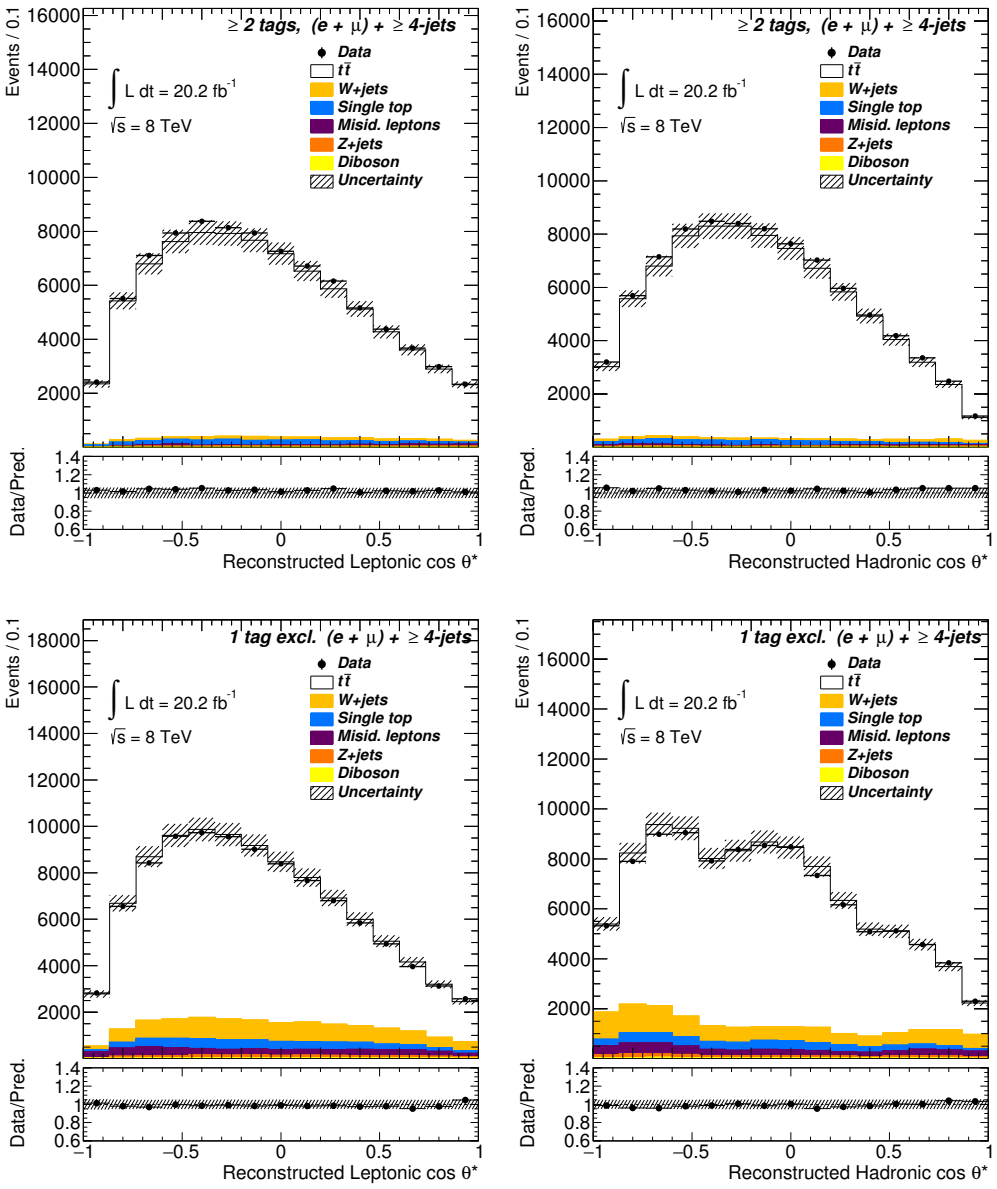

Figure 6.5.: Data/prediction comparison for combined electron and muon channels after event selection and the likelihood cut for leptonic and hadronic $\cos\theta^*$ distribution with ≥ 2 b-tags (top) and 1 b-tag (bottom). The displayed uncertainties represent the Monte Carlo statistical uncertainty as well as the background normalisation uncertainties.

6.2.1. Kinematic Likelihood Fitting

The selected events are reconstructed using a kinematic likelihood package (`KLFitter`) [148] based on the *Bayesian Analysis Toolkit* (BAT) [149]. The `KLFitter` uses the $t\bar{t}$ decay topology as an input model with the m_t and m_W mass constraints on composite objects built from the input lepton, $E_{\mathrm{T}}^{\mathrm{miss}}$, and jets to map the input objects to leading order partons and lepton from the $t\bar{t}$ decay.

Since the detector has a limited energy/momentum resolution, the energy/momentum of the input objects is allowed to vary within the corresponding detector resolutions, while the coordinate information of these objects is assumed to be measured precisely. This information is incorporated by the so-called *transfer functions* (TF), which describe the probability of detecting a final state object with energy E^{meas} originating from LO parton/lepton with true energy E. Separate TFs are derived for electrons, muons, light jets, b-jets, and $E_{\mathrm{T}}^{\mathrm{miss}}$ in different η ranges. The final two and three-body masses are evaluated with Breit-Wigner distributions using top quark and W boson masses fixed to $m_t = 172.5$ GeV and $m_W = 80.2$ GeV. The likelihood is defined as:

$$\mathscr{L} = BW(m_{q1q2q3}|m_t\Gamma_t) \cdot BW(m_{q1q2}|m_W\Gamma_W) \cdot BW(m_{q4\ell\nu}|m_t\Gamma_t) \cdot BW(m_{\ell\nu}|m_W\Gamma_W)$$
$$\prod_{i=1}^{4} W_{jet}(E_i^{meas}|E_i) \cdot W_{\ell}(E_{\ell}^{meas}|E_{\ell}) \cdot W_{miss}(E_x^{miss}|p_x^{\nu}) \cdot W_{miss}(E_y^{miss}|p_y^{\nu}), \tag{6.1}$$

where $W_i(E_x^{meas}|E_i)$ are the transfer functions, E_x^{meas} is the measured energy of a reconstructed object x, E_i is the 'true' energy of the corresponding parton i, and the $BW(m_{ij(k)}|m_Y\Gamma_Y)$ are the Breit-Wigner functions used to evaluate the mass of composite reconstructed particles with respect to a set mass and width of particle Y. The in-depth discussion about the construction and use of the transfer functions is follows.

Permuting the jets in an event through all positions in the model hypothesis yields different likelihood values for each permutation. To increase the reconstruction efficiency[1] of the `KLFitter`, the likelihood of a given permutation is extended to an *event probability* by adding additional information such as b-tagging and kinematic differences between types of light jets. This extension is discussed in details in Section 6.2.2. After the calculation of the likelihood (and/or event probability) of each permutation, the permutation with the highest event probability defines the reconstructed event and chosen for

[1] The ratio of the correctly reconstructed events (all four jets match their corresponding partons) to all selected events

measuring the angles to extract the W boson helicity fractions.

Reconstructed distributions from the leading permutation after applying the log likelihood cut of >-48 are shown in Figs 6.6–6.9, where good agreement between data and prediction is observed in all channels.

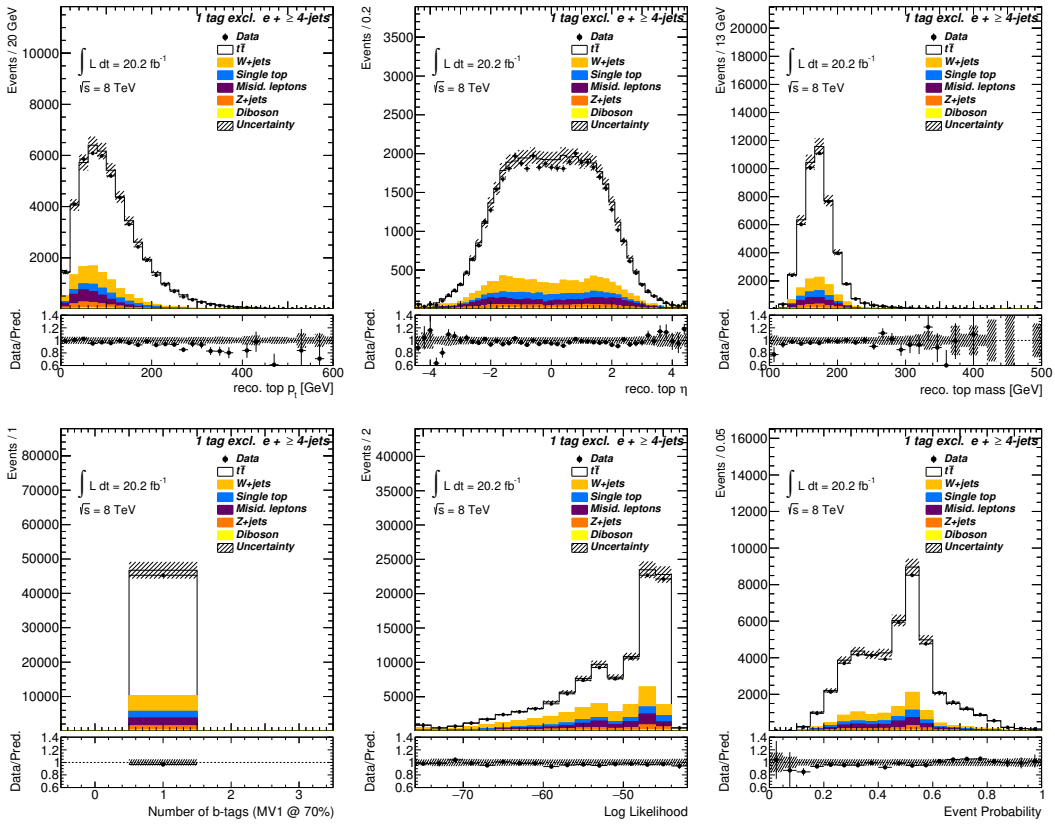

Figure 6.6.: Plots showing selected top quark kinematics, the log likelihood, and the event probability distributions of the leading permutation (ranked by event probability) in the electron channel with 1 b-tag. All plots except for the log likelihood are shown after the log LH > -48 cut. The displayed uncertainties represent the Monte Carlo statistical uncertainty as well as the background normalisation uncertainties.

Transfer Functions

The transfer functions are obtained from $t\bar{t}$ events simulated with MC@NLO [150, 151], to map the energies and momenta of the final state objects at the detector level to the parton level energy at LO MC simulation. The final state objects at parton/lepton

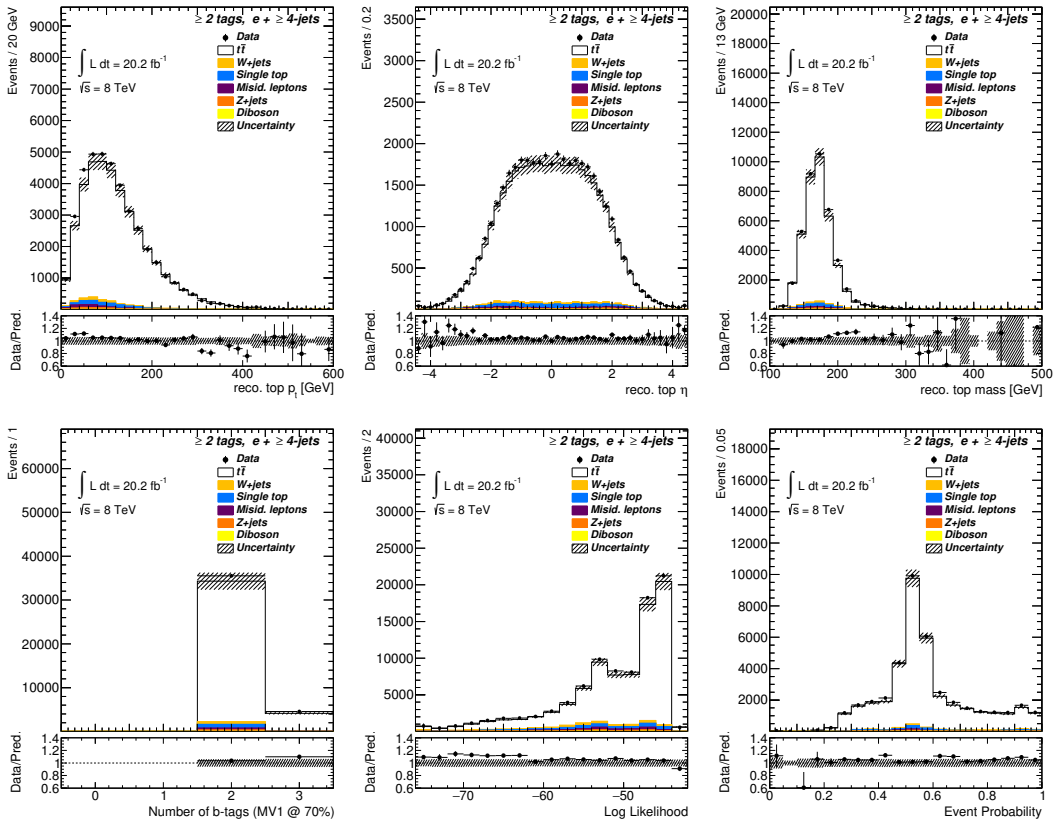

Figure 6.7.: Plots showing selected top quark kinematics, the log likelihood, and the event probability distributions of the leading permutation (ranked by event probability) in the electron channel with ≥ 2 b-tags. All plots except for the log likelihood are shown after the log LH > -48 cut. The displayed uncertainties represent the Monte Carlo statistical uncertainty as well as the background normalisation uncertainties.

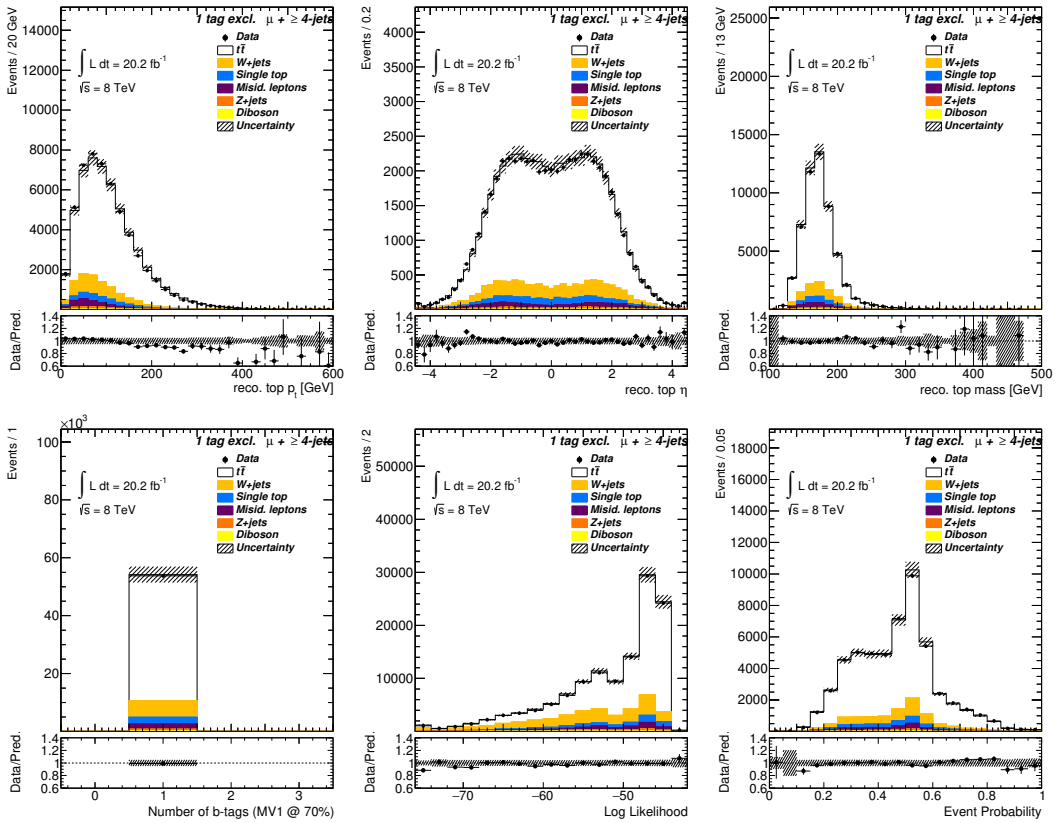

Figure 6.8.: Plots showing selected top quark kinematics, the log likelihood, and the event probability distributions of the leading permutation (ranked by event probability) in the muon channel with 1 b-tag. All plots except for the log likelihood are shown after the log LH > -48 cut. The displayed uncertainties represent the Monte Carlo statistical uncertainty as well as the background normalisation uncertainties.

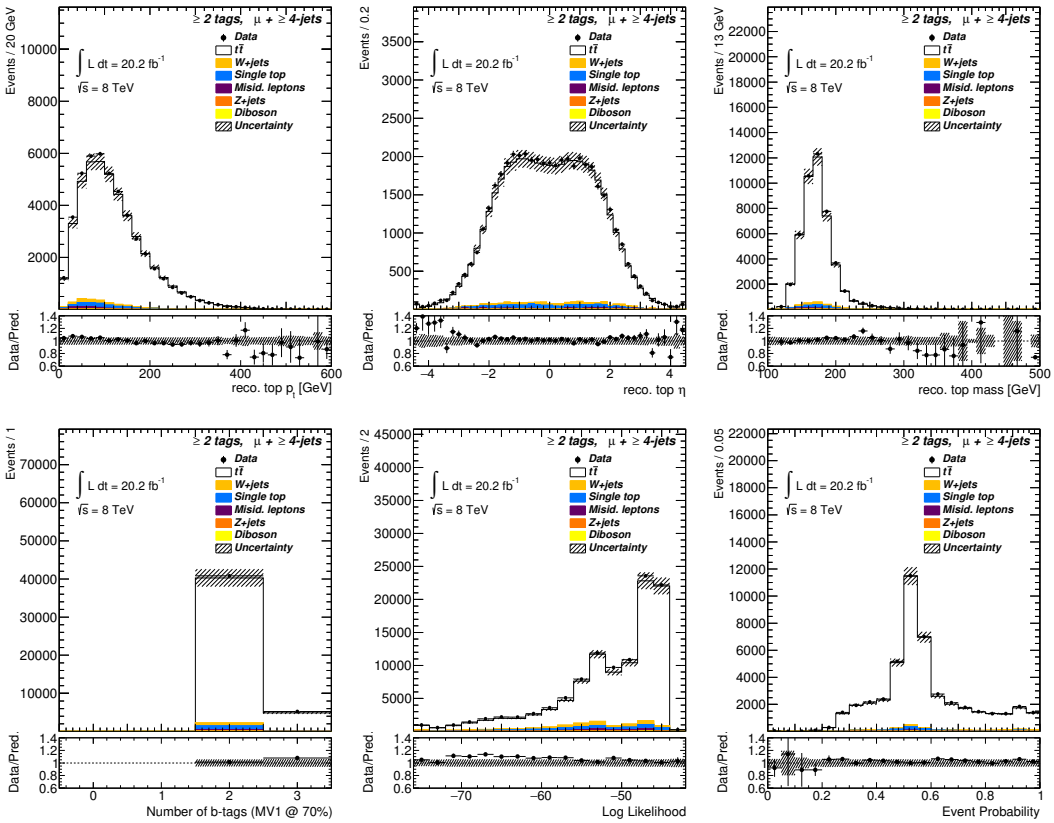

Figure 6.9.: Plots showing selected top quark kinematics, the log likelihood, and the event probability distributions of the leading permutation (ranked by event probability) in the electron muon with ≥ 2 b-tags. All plots except for the log likelihood are shown after the log LH > -48 cut. The displayed uncertainties represent the Monte Carlo statistical uncertainty as well as the background normalisation uncertainties.

level are uniquely matched to the reconstructed objects to obtain a continuous function describing the relative energy (momentum in case of muons) difference between these two stages as a function of the parton-level (*truth-level*) energy (momentum). In order to derive the transfer functions, only the reconstructed objects are used that match one-to-one to partons from the hard process. An object is considered matched when the distance ΔR between the reconstructed and truth object is less than 0.3.

The energy difference is fitted using a double Gaussian function of the form:

$$W(\Delta E) = \frac{1}{\sqrt{2\pi}(p_2 + p_3 p_5)} \left[e^{\frac{-(\Delta E - p_1)^2}{2p_2^2}} + p_3 \cdot e^{\frac{-(\Delta E - p_4)^2}{2p_5^2}} \right] \tag{6.2}$$

where $\Delta E = \frac{E_{\text{truth}} - E_{\text{reco}}}{E_{\text{truth}}}$.

As the detector response changes in different regions of the detector, individual parametrisations are derived for different regions of $|\eta|$. Also, the detector response changes with respect to each particle species. Hence, individual transfer functions are derived for electrons, muons[2], light jets, b-jets, and $E_{\text{T}}^{\text{miss}}$. As an example, Figure 6.10a shows the TF set for light jets in the central region of the detector.

The parameters p_i depend on the energy of the parton/lepton and are defined as:

$$p_i = a_i + b_i \cdot E_{\text{truth}} \quad \text{for} \quad i = 1, 3, 5, \tag{6.3}$$

$$p_i = a_i / \sqrt{E_{\text{truth}}} + b_i \quad \text{for} \quad i = 2, 4, \tag{6.4}$$

where a_i's and b_i's are obtained from a global fit for each particle species and η region. For muons, all P_i's are parametrised linearly. For jets and electrons, $p_{2,4}$ in Equation 6.4 represent the calorimeter resolution and are hence parametrised as[3] $\sim 1/\sqrt{E}$, while these parameters are considered to be linear for muons[4]. A linear dependence is assumed for all other parameters as shown in Equation 6.3.

Since the resolution of the $E_{\text{T}}^{\text{miss}}$ depends on the scalar sum of the deposited energy in the calorimeters in the transverse plane ($\sum E_T$) [152], the width of the difference $(E_{x,y}^{\text{miss}} - p_{x,y}^{\nu})$ is parametrised as a function of $\sum E_T$ as:

$$\sigma(\sum E_T) = p_0 + \frac{p_1}{1 + e^{-p_2(\sum E_T - p_3)}}. \tag{6.5}$$

[2] In the case of muons, the transfer function is given in terms of the p_{T} of the reconstructed and truth object.

[3] The calorimeter resolution in higher energies behaves as $\frac{\sigma E}{E} \sim \frac{1}{\sqrt{E}}$

[4] The muon momentum resolution decreases linearly as the muon p_{T} increases ($\frac{\sigma p_T}{p_T} \sim p_T$).

Figure 6.10b represents the transfer functions for neutrinos as a function of $\sum E_T$.

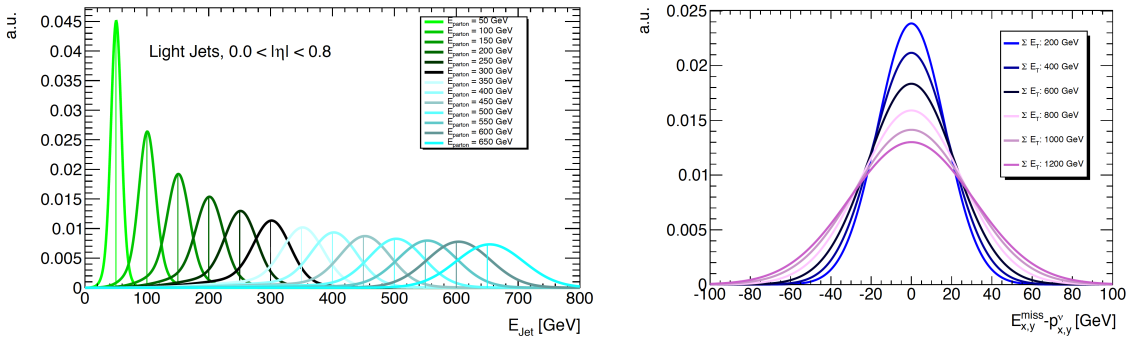

(a) (b)

Figure 6.10.: (a) TFs set for light jets in the central $|\eta|$ region, and (b) TFs set for neutrinos/$E_{\mathrm{T}}^{\mathrm{miss}}$ parametrised as a function of $\sum E_T$ [85]. The plots correspond to TFs obtained at 7 TeV (8 TeV TFs are used in this analysis).

For the reason of simplicity, the TFs model the energy resolution of the objects for a fixed (or narrow bin) E_{truth} via double Gaussian functions.

6.2.2. Up/Down-type Quarks Separation

Extracting the W boson helicity fractions using the hadronic analyser requires a correct reconstruction of the W boson daughter jets. Since a permutation of the two non-b-jets is invariant with respect to the candidate W boson and top quark masses in Equation 6.1, a quantity including information beyond the kinematics is necessary to correctly assign all four jets in the $t\bar{t}$ decay. As mentioned in Section 6.2.1, the likelihood is extended to an event probability, and for a given permutation, i, is given by:

$$p_i = \frac{\mathcal{L}_i \prod_j \Delta p_{i,j}}{\sum_i \mathcal{L}_i \prod_j \Delta p_{i,j}} \tag{6.6}$$

where the $\Delta p_{i,j}$'s are extensions or weights multiplied by the likelihood value to take into account the additional information.

The first extension is the b-tagging (MV1) weight of the jets. The simplest example of this is the application of a binary weight of 1(0) depending on whether a jet permuted into the position of a b-jet has an MV1 weight larger (smaller) than a predefined threshold,

e.g.

$$\Delta p_{i,j} = \begin{array}{ll} 0 & \text{if jet position is for a } b\text{-jet and the input jet is not } b\text{-tagged} \\ 1 & \text{if position is for a } b\text{-jet and the input jet is } b\text{-tagged.} \end{array} \tag{6.7}$$

To extract the helicity fractions in the hadronic channel, a further extension is needed to differentiate the up- and down-type jets of the W boson decay. In this regard, p_{T} dependent MV1 weight distributions obtained for different jet flavours are used. Compared to jets coming from u, d, and s quarks, jets coming from c quarks are much heavier and should have correspondingly higher MV1 weights. This discrimination is observable in Figure 6.11. These W bosons that decay via $W \to c\bar{s}$ (about 50 % of all hadronically decaying W bosons) allow the MV1 information to help to identify light jets in a significant number of reconstructed events.

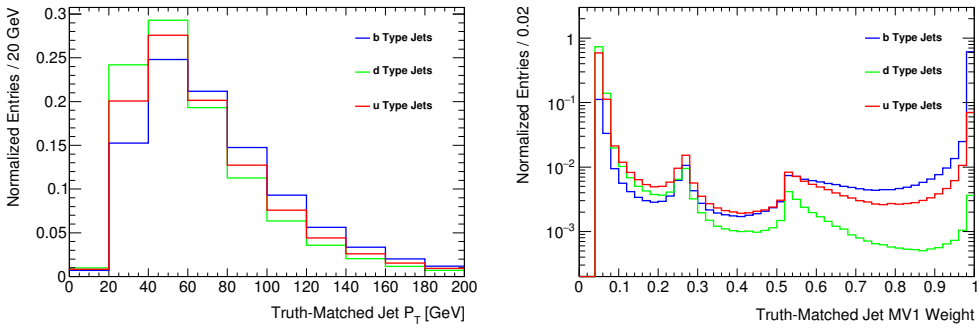

Figure 6.11.: Templates of reconstructed p_{T} and MV1 weight for truth-matched u-type, d-type, and b-jets. These templates are used as inputs to the u/d separation configuration of `KLFitter`.

A u/d separation extension can be calculated using templates of the reconstructed jet p_{T} and MV1 distributions. This approach follows the path introduced in [153]. The templates were created for up-type ($q = u, c$), down-type ($q = d, s$), and b-jets ($q = b$) using the $\sqrt{s} = 8$ TeV $t\bar{t}$ events simulated via MC@NLO. The reconstructed jets must be matched one–to–one within $\Delta R \leq 0.3$ to one of the quarks produced in the $t\bar{t}$ decay in order to be counted in the templates. Using these templates, the product of the probability extensions for all jets in one fit is given as:

$$\begin{aligned} \Delta p_{i,\mathrm{u/d\ sep}} = {} & P_1^{\text{b-type}}(p_{\mathrm{T}}^{\text{blep}}) \cdot P_2^{\text{b-type}}(MV1^{\text{blep}}) \cdot P_1^{\text{b-type}}(p_{\mathrm{T}}^{\text{bhad}}) \cdot P_2^{\text{b-type}}(MV1^{\text{bhad}}) \cdot \\ & P_1^{\text{u-type}}(p_{\mathrm{T}}^{\text{u-jet}}) \cdot P_2^{\text{u-type}}(MV1^{\text{u-jet}}) \cdot P_1^{\text{d-type}}(p_{\mathrm{T}}^{\text{d-jet}}) \cdot P_2^{\text{d-type}}(MV1^{\text{d-jet}}), \end{aligned} \tag{6.8}$$

where P_1 (P_2) represent the probability of a particular jet to have its measured values of p_T (MV1) given the jet assignment (b-jet from leptonic top (blep), b-jet from hadronic top (bhad), u-jet, d-jet) in the current permutation. The probabilities are calculated using the templates of Figure 6.11 when normalised to unity. Using these weights, the event probability is calculated for each permutation.

This extension increases the fraction of events with correct matching of the two jets originating from a W boson decay to the corresponding up- and down-quark type jet to 60%, compared to 50% correctness in random selection.

Dedicated linearity tests were performed to check whether the use of templates based on the p_T of the jets introduces a bias for left- and right-handed events. For the hadronic analyser, the calibration curves resulting from the linearity tests are presented in Section 7.3, where no bias was observed.

6.2.3. Reconstruction Optimisation Study

In general, the number of jets used as input in the `KLFitter` algorithm can be larger than four. To further increase the reconstruction efficiency, the following jet input scenarios are studied:

- **Simple 4-jets:** Using four leading jets in p_T
- **Simple 5-jets:** Using four (five) leading jets in p_T for events with 4 (≥ 5) jets
- **Advanced 5-jets:** Using two jets with the largest b-tagging weight (MV1) + two (three) leading jets in p_T for events with 4 (≥ 5) jets

The performance of a reconstruction algorithm can be quantified via the reconstruction efficiency. This efficiency relies on the jets available for a permutation. Considering the u/d separation configuration, regardless of the invariance of the hadronic W boson reconstruction under the swap of the u/d quarks, supplying KLFitter with n input jets requires the likelihood calculation for $n!$ permutations. The matching efficiency is defined as:

$$\epsilon_{\text{match}} = N_{\text{events}}^{\text{match}} / N_{\text{events}}^{\text{total}} \tag{6.9}$$

where $N_{\text{events}}^{\text{match}}$ can be defined in several different ways (e.g. correctly matching all four jets, correctly matching only the three jets necessary for the hadronic angle, correctly matching only the b-jets, etc.). In the following, an event is considered matched for the

leptonic angle when both b-jets are correctly matched while all four jets are required to be correctly matched in the hadronic case. Using these definitions, the final matching efficiencies are computed for both channels to find the optimal jet input configuration.

The simplest jets input configuration is to feed the `KLFitter` with the four highest p_{T} jets. The two b-jets are most likely the highest jets in p_{T} and the third and fourth place in p_{T} usually are the two light jets originating from the hadronic decay the W boson. However, it is also possible to have high p_{T} jets originating from initial/final state radiation within the four highest jets in p_{T}. In such cases, a simple 4-jet configuration leads to incorrect event reconstruction since the correct jet never made its way to the permutations.

The simplest extension is increasing the number of input jets to five (if they exist). In this case (simple 5-jets), the fitter iterates through $5! = 120$ permutations, and thus a jet corresponding to a direct top quark decay product sitting in the fifth place in p_{T} will be considered. Another option is to change the ordering by which jets are chosen to be included in the fit. A straightforward option is to pick-up the two jets with the highest MV1 weights, regardless of their p_{T} order, and then fill the rest of the free places according to the jet p_{T} orders (advanced 5-jets).

For this analysis, the three mentioned input configurations are studied and the result is summarised in Table 6.2.

Configuration	Matching efficiency
Simple 4-jet	0.260
Simple 5-jet	0.292
Advanced 5-jet	0.323

Table 6.2.: Matching efficiencies for different `KLFitter` input jet configurations. An event is considered matched if all four truth jets from the $t\bar{t}$ decay are bi-uniquely within a $\Delta R \leq 0.3$ matched to the four reconstructed jets of the leading `KLFitter` permutation.

This study shows that using the advanced 5-jets option leads to the highest reconstruction efficiency for events with four (at least five) jets. A similar decision was also made in [140]. Therefore, this option is chosen as the `KLFitter` input configuration in this analysis.

6.2.4. Hadronic Analyser Sensitivity Optimisation

Extracting the helicity fractions using the hadronic analyser is less sensitive than the corresponding extraction from the leptonic one since in the former case the down-type jet is in general harder to correctly identify than the charged lepton (electron or muon) used in the leptonic analyser. Indeed the leptonic and hadronic analyser distributions at the truth-level are identical, since the polarisation of the W boson does not depend on its decay mode. The incorrectly assigned jets (mostly due to swapping between the two light jets originating from the hadronic decay of the W boson) lead to left-handed and right-handed templates that closely resemble each other (see Section 7.1).

In order to obtain better up-/down-type quark separation and a more sensitive result, it is essential to select a subset of reconstructed events which contains a relatively higher fraction of correctly matched events. In this regard, four categories of $t\bar{t}$ reconstruction are defined, and the events in the resulting categories are plotted to identify the regions with higher fractions of correctly matched events:

- **Correctly reconstructed**: All 4 partons uniquely matched to their corresponding truth jets, and correctly assigned in the `KLFitter` permutation with the highest event probability (leading permutation),
- **Incorrectly reconstructed**: All 4 partons uniquely matched to their corresponding truth jets, but not correctly assigned in the leading `KLFitter` permutation,
- **Non-reconstructable**: Due to acceptance loss or non-unique matching, not all four jets from the $t\bar{t}$ decay can be matched to reconstructed objects,
- **Background**: $t\bar{t}$ events which do not have a lepton+jets topology, such as dileptonic or tauonic $t\bar{t}$ decays where no true hadronic angle exists.

Figure 6.12 shows the distributions for the event probability and the logarithm of the likelihood for the leading `KLFitter` permutation for the above defined $t\bar{t}$ event categories. Both plots are normalised to the total $t\bar{t}$ yield from the 2012 dataset.

The peak at 0.5 in Figure 6.12b corresponds to events where the algorithm fails to differentiate the up- and down-type quarks, resulting in two permutations with similar event probability value but swapped u/d jets assignments. While there is no region with clear concentration of correctly matched $t\bar{t}$ events in the event probability distribution, correctly matched events are concentrated in the log likelihood distribution above values of -55 as shown in Figure 6.12a.

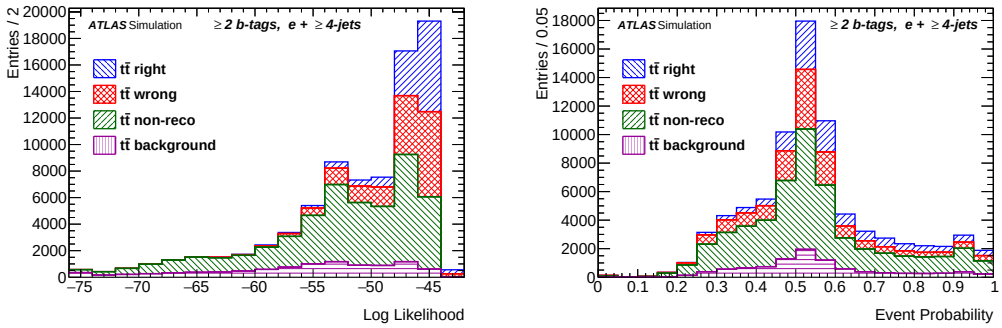

(a) (b)

Figure 6.12.: Categorised $t\bar{t}$ distributions for log likelihood (a) and event probability (b) of the `KLFitter` permutation with the highest event probability, obtained for the electron channel with ≥ 2 b-tags. The total yield is normalised to the $t\bar{t}$ yield from 20.2 fb^{-1} [154].

In order to find an optimised selection, a scan of the log likelihood cut values to achieve the best expected statistical uncertainty of the measured W boson helicity fractions in events with ≥ 2 b-tags[5] was performed.

The template fitting method used to study the effect of the likelihood cuts is discussed in Section 7.1. The background normalisations in the fit were fixed in order to isolate the effect of the likelihood cut on the $t\bar{t}$ signal. Results of the sensitivity on the extracted fractions and the signal efficiencies as a function of the likelihood cut are shown in Table 6.3.

As a result, a log likelihood cut of > -48 is found to minimise the expected statistical uncertainty in the hadronic channel. An identical study using the leptonic analyser showed no significant impact on sensitivity for any cut on likelihood, due to the much larger separation between the left- and right-handed templates. Therefore, the optimal cut on log likelihood > -48 found for the hadronic side is applied to all events for both analysers to simplify the leptonic + hadronic combination.

[5]Since the highest W boson helicity fractions sensitivity is obtained from events with ≥ 2 b-tags, the optimisation study was performed in this region.

Channel		LH > -49	LH > -48	LH > -47	LH > -46
e+jets	σ_{F_0}	0.0168±0.0002	0.0167±0.0002	0.0174±0.0002	0.0193±0.0002
	σ_{F_L}	0.0299±0.0003	0.0301±0.0003	0.0299±0.0003	0.0350±0.0003
	σ_{F_R}	0.0293±0.0003	0.0285±0.0003	0.0288±0.0003	0.0324±0.0003
μ+jets	σ_{F_0}	0.0159±0.0002	0.0161±0.0002	0.0170±0.0002	0.0193±0.0002
	σ_{F_L}	0.0285±0.0003	0.0281±0.0003	0.0297±0.0003	0.0353±0.0004
	σ_{F_R}	0.0273±0.0003	0.0268±0.0003	0.0288±0.0003	0.0337±0.0004

LH Cut Efficiency	0.418	0.375	0.308	0.212

Table 6.3.: Top: scan of log likelihood cuts performed to find the cut value that yields the best statistical sensitivity of the W boson helicity fractions extracted using the hadronic analyser. σ_{F_i} is the expected statistical uncertainty in measuring the helicity fraction F_i. Bottom: $t\bar{t}$ efficiency for each likelihood cut in the scan.

7 Analysis Strategy

In this analysis the W boson polarisation is accessed via the angular distribution of the leptonic (hadronic) analyser, as introduced in section 2.2.3. The cosine of the angle between the momentum direction of the charged lepton (down-type quark) from the leptonic (hadronic) W boson decay and the reversed momentum direction of the b-quark from the top quark decay, in the W boson rest frame, is sensitive to the W boson polarisation. The helicity fractions (polarisation of the W boson) are measured using a binned likelihood template fit to data, i.e. by comparing the shape of data and simulated distributions of the analyser.

In Section 7.1, a brief discussion of the reweighting method for producing pure helicity templates is provided, followed by a discussion of the mechanism of the likelihood fit itself. The correlation between the leptonic and hadronic measurements is discussed in Section 7.2. Finally the chapter concludes with the validation of the introduced method in Section 7.3.

7.1. Template Fitting

The W boson helicity fractions F_i are defined as the fraction of the number of $t\bar{t}$ events N_i with a specific polarisation state with respect to the total number of signal events:

$$F_i = \frac{N_i}{N_0 + N_L + N_R}, \quad \text{for} \quad i = 0, L, R. \tag{7.1}$$

The distribution of the introduced observable $\cos\theta^*$ allows to determine N_i and thus the helicity fractions as stated in Equation 2.20.

7.1.1. Template Reweighting

Dedicated $t\bar{t}$ signal templates for pure longitudinal, left- and right-handed helicity states are produced by reweighting the POWHEG SM $t\bar{t}$ events at truth level. The functional form of $\cos\theta^*$ distribution, i.e. Equation 2.20, is fit to the truth $\cos\theta^*$ distribution obtained from the simulated events, to obtain the SM helicity fractions of the sample, F_i^{Powheg}.

Two sets of weights (one for the hadronic W boson and one for the leptonic W boson) are generated per event using the truth $\cos\theta^*$ values from $t\bar{t}$ events after event selection/reconstruction. The produced weights, $W_i(\cos\theta^*)$ are of the form:

$$W_i(\cos\theta^*) = \frac{w_i(\cos\theta^*)}{w_0(\cos\theta^*) + w_L(\cos\theta^*) + w_R(\cos\theta^*)} \tag{7.2}$$

where $i = 0$, L, R and the components $w_i(\cos\theta^*)$ are taken from Equation 2.20 and have functional form

$$w_0(\cos\theta^*) = \frac{3}{4}(1 - cos^2\theta^*)F_0^{\text{Powheg}} \tag{7.3}$$

$$w_L(\cos\theta^*) = \frac{3}{8}(1 - cos\theta^*)^2 F_L^{\text{Powheg}} \tag{7.4}$$

$$w_R(\cos\theta^*) = \frac{3}{8}(1 + cos\theta^*)^2 F_R^{\text{Powheg}} \tag{7.5}$$

Figures 7.1 to 7.4 display the produced signal templates for e+jets and μ+jets channels in both b-tag regions for both leptonic and hadronic analysers.

In addition to the three signal templates for each channel, five different background templates are included: three templates for W+jets background, one for each flavour component (W+light jets, $W + c$ jets, $W + b\bar{b}/c\bar{c}$ jets), one template for misidentified leptons and one template for the remaining background contributions, namely, single top, Z+jets and diboson processes. The background templates for leptonic and hadronic analysers in both b-tag regions are shown in Figures 7.5 to 7.8.

The fluctuations and spikes in W+light and $W+c$ jets background templates in ≥ 2 b-tags region are due to the lack of MC statistics in the used samples. A comparison study was performed using the `TH1::Smooth()` [155] method implemented in ROOT to avoid fluctuations in those templates. The smoothened templates were tested with χ^2 and *Kolmogorov* [156] tests, confirming the compatibility in shape between the smoothened and the default templates. No significant difference in the fit results was observed by

using smoothened background templates in place of the default templates.

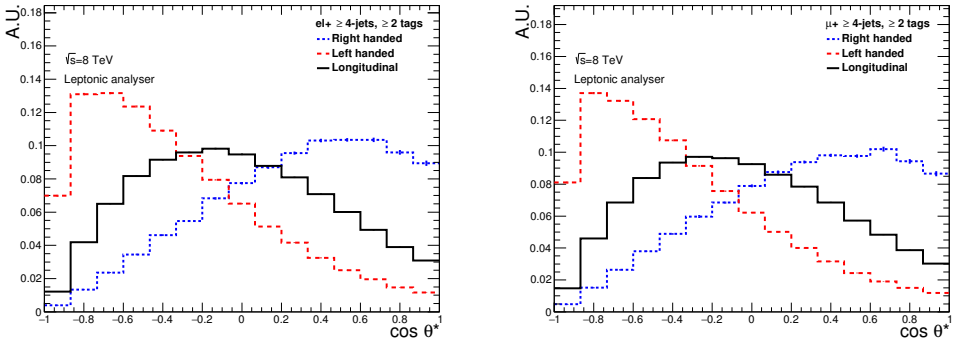

Figure 7.1.: Reconstructed signal templates for e+jets channel (left) and μ+jets channel (right) with ≥ 2 b-tags, for the leptonic angle.

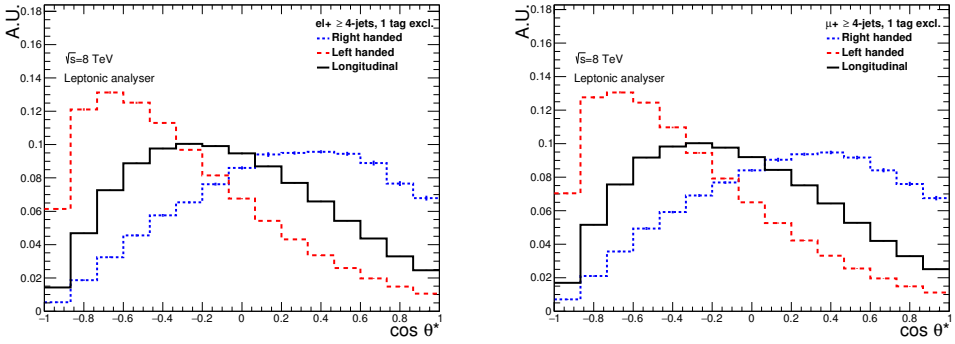

Figure 7.2.: Reconstructed signal templates for e+jets channel (left) and μ+jets channel (right) with 1 b-tag, for the leptonic angle.

7.1.2. Acceptance Effects

The acceptance effects caused by the event selection distort the distribution of $\cos\theta^*$. The primary sources of this distortion is discussed in Section 6.1.1. Figures 7.9 and 7.10 illustrate the acceptance effects by comparing the $\cos\theta^*$ distribution in the full phase space (before applying any selection) and the corresponding distributions after selection at truth and reconstructed levels.

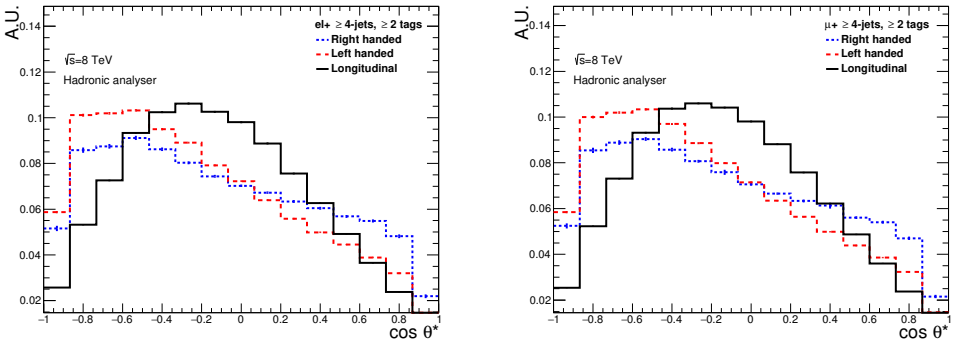

Figure 7.3.: Reconstructed signal templates for e+jets channel (left) and μ+jets channel (right) with ≥ 2 b-tags, for the hadronic angle.

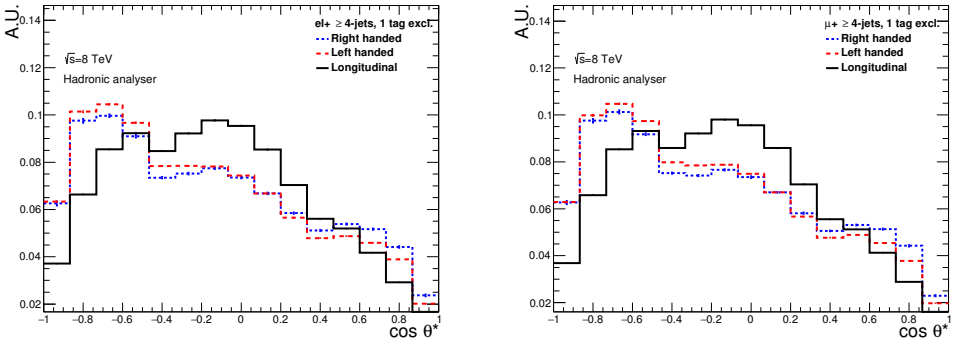

Figure 7.4.: Reconstructed signal templates for e+jets channel (left) and μ+jets channel (right) with 1 b-tag, for the hadronic angle.

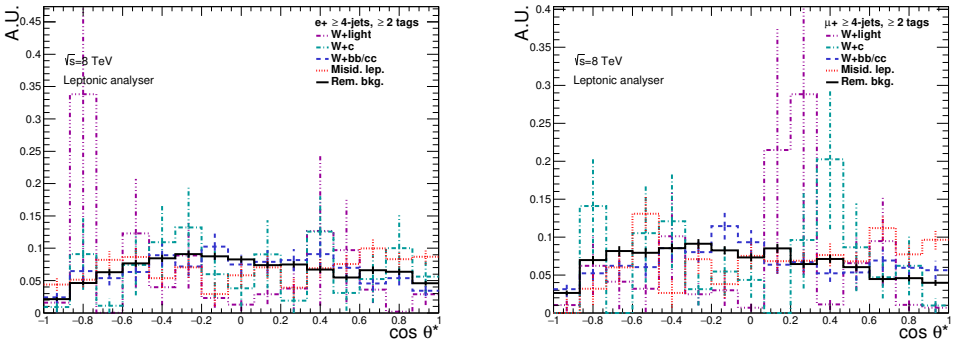

Figure 7.5.: Background templates for e+jets channel (left) and μ+jets channel (right) with ≥ 2 b-tags, for the leptonic angle.

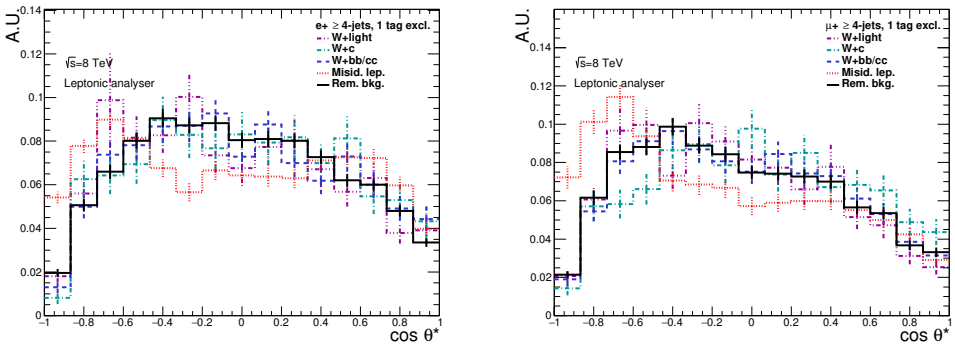

Figure 7.6.: Background templates for e+jets channel (left) and μ+jets channel (right) with 1 b-tag, for the leptonic angle.

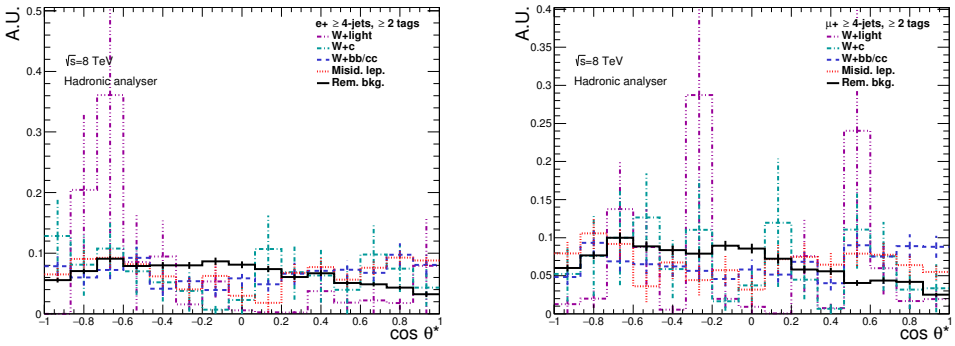

Figure 7.7.: Background templates for e+jets channel (left) and μ+jets channel (right) with ≥ 2 b-tags, for the hadronic angle.

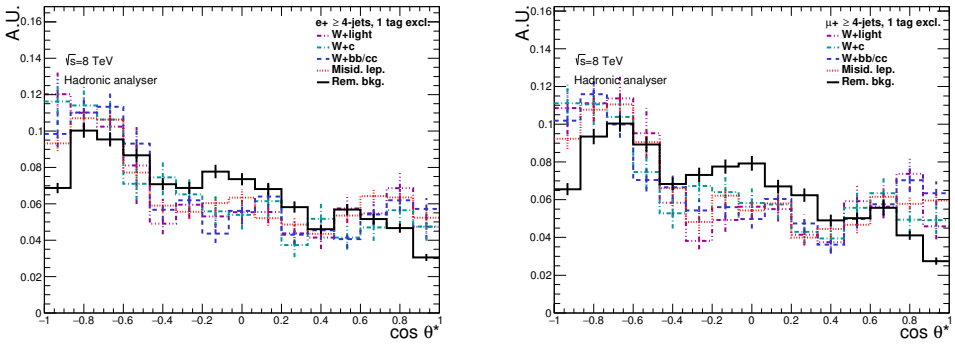

Figure 7.8.: Background templates for e+jets channel (left) and μ+jets channel (right) with 1 b-tag, for the hadronic angle.

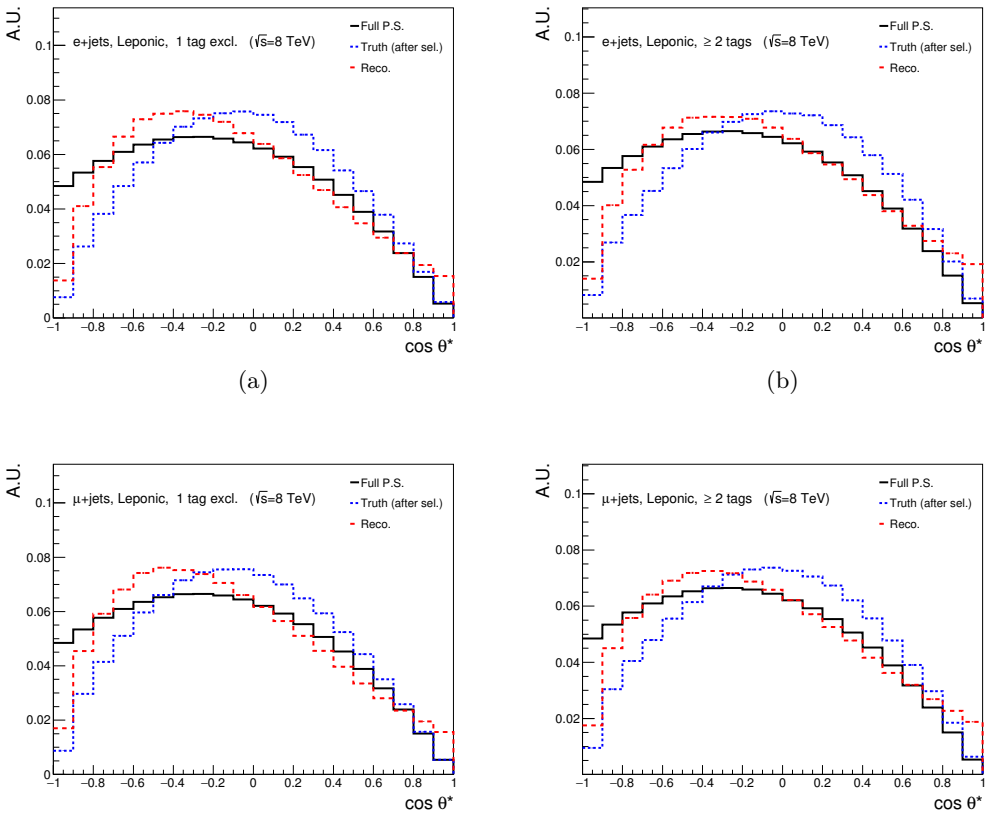

Figure 7.9.: Comparison between the full phase space (solid line), truth level after selection (short dashed line) and the reconstructed (long dashed line) distribution of the $\cos\theta^*$ obtained from the leptonic analyser in e+jets channel with 1 b-tag (a) and ≥ 2 b-tags (b), and in μ+jets channel with 1 b-tag (c) and ≥ 2 b-tags (d).

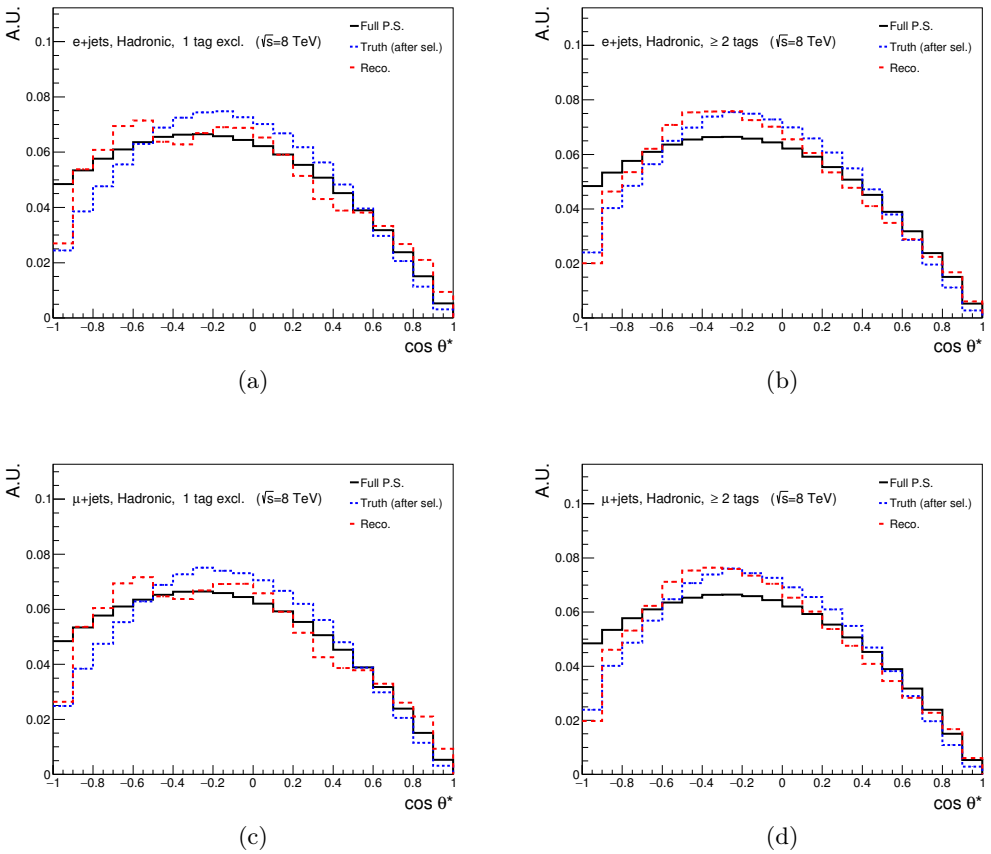

Figure 7.10.: Comparison between the full phase space (solid line), truth level after selection (short dashed line) and the reconstructed (long dashed line) distribution of the $\cos\theta^*$ obtained from the hadronic analyser in e+jets channel with 1 b-tag (a) and ≥ 2 b-tags (b), and in μ+jets channel with 1 b-tag (c) and ≥ 2 b-tags (d).

7.1.3. Likelihood Fit

A binned likelihood fit[1] is performed using the signal and background templates mentioned in the previous section. The normalisations of the background processes constrained in the fit via prior Gaussian distributions, while the normalisation of each signal template is the free parameter in the fit. Each template is normalised to the its corresponding event yield. The total number of expected events after selection corresponds to the sum of all template normalisations and is given by:

$$n_{\text{exp}} = n_0 + n_{\text{L}} + n_{\text{R}} + n_{W+\text{light}} + n_{W+c} + n_{W+bb/cc} + n_{\text{fake}} + n_{\text{rem. bkg.}}, \tag{7.6}$$

to be compared bin-by-bin to the data distribution via the maximum likelihood fit of:

$$\mathscr{L} = \prod_{i=1}^{N_{\text{bins}}} \text{Poisson}(n_{\text{data},i}, n_{\text{exp},i}) \prod_{j=1}^{N_{\text{bkg}}} \frac{1}{\sqrt{2\pi}\sigma_{\text{bkg.j}}} e^{\frac{-(n_{\text{bkg.j}}-\hat{n}_{\text{bkg.j}})^2}{2\sigma^2_{\text{bkg.j}}}}, \tag{7.7}$$

where $\hat{n}_{\text{bkg.j}}$ and $\sigma_{\text{bkg.,j}}$ represent the expected number of background events and its corresponding uncertainty, respectively, and j corresponds to each background template.

All channels share the same fit parameters of Eq. 7.6, which are considered to be correlated across the simultaneously fitted channels, except for n_{fake}. The fake lepton background normalisation is uncorrelated between electrons and muons and different b-tag regions since it is derived independently for each region. For the W+jets components, the normalisation uncertainties are taken from the data-driven calibration factors derived in [140], as explained in Section 5.5.2. A relative uncertainty of 30% estimated using various control regions in the matrix method calculation[146], is used for the fake lepton contribution.

An uncertainty of 16% (17%) is considered for the normalisation of the remaining background sources in the ≥ 2 b-tags region (1 b-tag + ≥ 2 b-tags regions[2]). This uncertainty is composed of (a): 17% normalisation uncertainty on the single top component which takes into account the theoretical uncertainty in cross section calculation, the systematic uncertainty on the initial and final state radiation in t-channel and for the additional associated jets, (b): an overall normalisation uncertainty of 48% on normalisation of the Z+jets and diboson contributions which takes into account 5% uncertainty on the theoretical (N)NLO cross section and uncertainties to account for the extrapolation to high jet multiplicity (24% per jet). A summary of all free parameters in the fit and their

[1] The fit procedure is based on the numerical minimisation computer program MINUIT [157, 158].
[2] See Section 7.1.4 for details on channels combination.

Fit Parameter	Relative Width of prior Gaussian distributions
n_0	–
n_L	–
n_R	–
$n_{W+\text{light}}$	0.05
n_{W+c}	0.25
$n_{W+bb/cc}$	0.07
n_{fake}	0.30
$n_{\text{rem. bkg.}}$	0.16(0.17) in $\geqslant 2$ b-tags (1 b-tag + $\geqslant 2$ b-tags)

Table 7.1.: List of free parameters in the likelihood fit and the relative widths (width/normalisation) of the prior Gaussian distributions assumed in the fit with the floating background normalisation.

Selection eff.	e+jets (lep)	μ+jets (lep)	e+jets (had)	μ+jets (had)
1 Exclusive b-tag				
ϵ_0	0.014	0.017	0.014	0.016
ϵ_L	0.010	0.013	0.012	0.014
ϵ_R	0.015	0.017	0.012	0.014
≥ 2 b-tags				
ϵ_0	0.014	0.017	0.013	0.016
ϵ_L	0.010	0.012	0.012	0.014
ϵ_R	0.016	0.018	0.012	0.014

Table 7.2.: Selection efficiencies in the 1 b-tag and ≥ 2 b-tags regions for both the leptonic and hadronic templates in the e+jets and μ+jets channel.

uncertainties is given in Table 7.1.

Since the event selection is not equally sensitive to all helicity states, extraction of the production-level helicity fractions requires knowledge of acceptance effect and the reconstruction efficiency per helicity state.

These efficiencies, ϵ_i^{sel} calculated using the nominal $t\bar{t}$ sample are taken into account in the fit and are summarised in Table 7.2.

The number of events with a helicity state N_i defined in Equation 7.1 is related to the corresponding selected number of events via:

$$n_i = \epsilon_i^{\text{sel.}} \cdot N_i, \quad \text{for} \quad i = 0, L, R. \tag{7.8}$$

Parameter	Norm. unc.	Pre-fit	Post-fit	Δ%
$t\bar{t}$	–	2.78e+06	2.87e+06 ± 44700	1.03
W+light	5%	68	68 ± 3	0.02
$W + c$	25%	105	105 ± 26	0.3
$W + bb/cc$	7%	1318	1317 ± 92	-0.08
fake 2incl. (el)	30%	447	575 ± 117	28.6
fake 2incl. (mu)	30%	330	285 ± 93	-13.6
Rem. bkg.	16%	2633	2629 ± 414	-0.2

Table 7.3.: Pre-fit and post-fit yields comparison in the combined electron + muon channels with ≥ 2 b-tags, obtained using the leptonic analyser.

7.1.4. Combination of Channels

In order to obtain the best precision in the measurement of the W boson polarisation, different combination configurations of the eight orthogonal channels (e/μ+jets $\times$ 1 b-tag/≥ 2 b-tags $\times$ leptonic/hadronic analyser) have been studied.

The channels are combined via a simultaneous likelihood fit. The signal templates for each of the respective helicity states are combined in an extended distribution with two/four/eight times the number of bins in the two/four/eight channel combination, while each background contribution is fitted according to its correlation across the fitted channels as described in the previous section. The selection efficiencies for the combined templates are adjusted accordingly. The combination leading to the lowest total uncertainty using the leptonic analyser is the two-channel combination (electron + muon) with ≥ 2 b-tags, while the four-channel combination (electron + muon) in the 1 b-tag + ≥ 2 b-tags regions gives the lowest total uncertainty using the hadronic analyser. Further discussion about the estimation of uncertainties is given in Chapter 8.

Despite the improvement in the statistical error and several sources of systematic error, the combination of leptonic and hadronic analysers lead to a larger total systematic uncertainty with respect to the two-channel combination of the leptonic analyser. The individual leptonic and hadronic measurements do however yield consistent results in agreement with each other and the corresponding results are compared in Chapter 9.

The summary of the pre-fit and post-fit yields in the combined electron + muon channels with ≥ 2 b-tags for leptonic analyser and in 1 b-tag + ≥ 2 b-tags regions for the hadronic analyser are summarised in Tables 7.3 and 7.4 respectively.

Parameter	Norm. unc.	Pre-fit	Post-fit	Δ%
$t\bar{t}$	–	2.78e+06	2.90e+06 ± 94400	1.04
W+light	5%	1430	1424 ± 71	-0.4
$W + c$	25%	2756	2070 ± 577	-24.9
$W + bb/cc$	7%	7565	7298 ± 495	-3.5
fake 1excl. (el)	30%	2272	1431 ± 348	-37
fake 1excl. (mu)	30%	447	620 ± 111	38.7
fake 2incl. (el)	30%	1746	1379 ± 340	-21
fake 2incl. (mu)	30%	323	283 ± 92	-12.3
Rem. bkg.	17%	9191	6019 ± 1290	-34.5

Table 7.4.: Pre-fit and post-fit yields comparison in the combined electron + muon channels in 1 b-tag + ≥ 2 b-tags regions, obtained using the hadronic analyser.

7.2. Correlations Between Leptonic and Hadronic Measurements

Since there are two measurements being performed per event (in case of performing a simultaneous fit using both leptonic and hadronic analysers), the correlation between the two angles needs to be quantified. Even though they are in principle uncorrelated as the W boson decays themselves are independent, a non-zero correlation could be introduced through the reconstruction. In the case of non-negligible correlation, it would be incorrect to evaluate the uncertainties in the different channels independently, and the correlation would need to be correctly accounted for. In the case of negligible correlation, the two channels can be treated as orthogonal channels.

To estimate the correlation, two-dimensional plots of $\cos\theta^*$ (one analyser per axis) are produced and the correlation factor (-1 for perfect anti-correlation, +1 for perfect correlation and 0 for 100% uncorrelated) calculated. The plots are shown in Figure 7.11. The correlation factor is evaluated for all events with at least two b-tags passing the nominal selection. The subset events with log LH > -48 cut (discussed in Section 6.2.4) is also compared.

The correlation factor is calculated to be -0.0029 (-0.0038) for the nominal selection (without imposing the LH cut). Therefore, the correlation is considered to be negligible in both cases, and the measurements are considered to be independent for the remainder of this analysis.

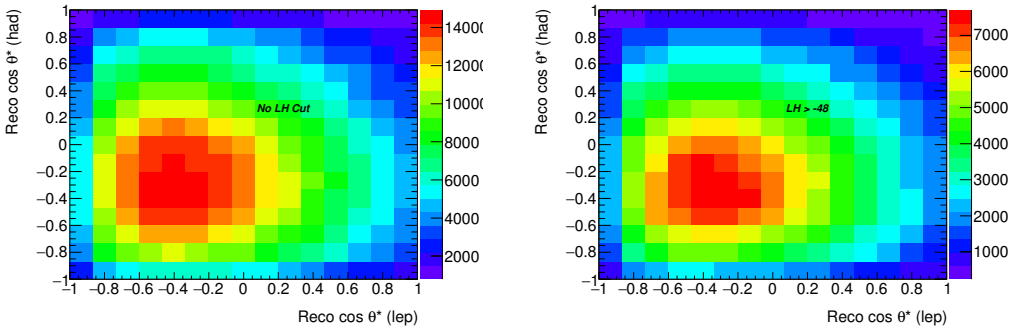

(a) (b)

Figure 7.11.: Two-dimensional distributions of the reconstructed leptonic and hadronic $\cos\theta^*$ in all events with two or more b-tags passing the nominal selection (a) and passing the nominal selection (b) to optimise the sensitivity of the hadronic analyser.

7.3. Method Validation

In order to ensure that the fit machinery is bias-free, the method is validated by performing linearity tests and creating pull distributions.

To check the linearity of the method, a number of pseudo-data sets is produced with different user-defined W boson helicity fractions. The default templates are fitted to those pseudo-data and the helicity fractions are extracted. In a bias-free machinery, it is expected that the same helicity fractions as input ones are obtained. In this study, the linearity test is performed by creating 5000 ensembles per calibration point varied via Poisson statistics with respect to the nominal pseudo-data corresponding to each calibration point. The longitudinal W boson helicity fraction is varied between 0.4 and 1.0 incremented by 0.1, the left- and right-handed fractions are both iterated in steps of 0.05 while enforcing the condition that the sum of the three fractions equals unity.

The linearity test results for the best combination for the leptonic and hadronic analysers are shown in Figures 7.12 and 7.13 respectively. For an unbiased estimator, a slope of one and offset of zero are expected and observed.

The pull is defined as the difference between the fitted value of N_{nom} and the value of N_j used to create the pseudo data which was fitted, divided by the uncertainty on the fitted value:

$$\text{Pull} = \frac{N_{nom} - N_j}{\sigma_{N_{nom}}}. \tag{7.9}$$

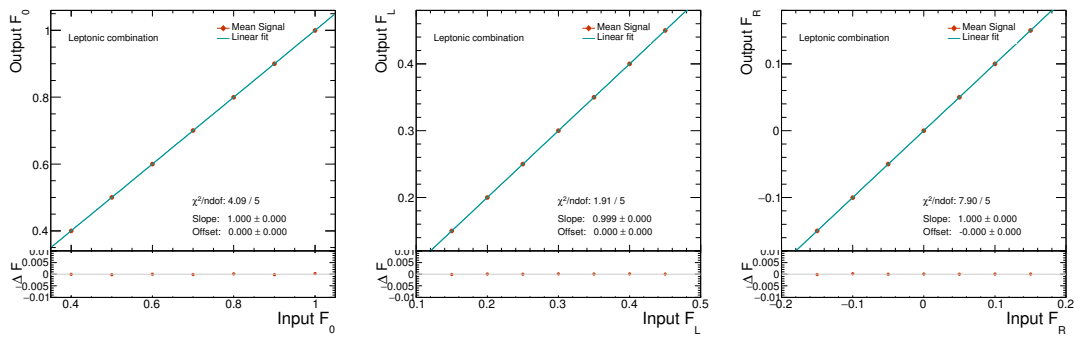

Figure 7.12.: Linearity checks for F_0, F_L, and F_R in the electron+muon channels with ≥ 2 b-tags for the leptonic analyser. 5000 sets of pseudo-data were fit to perform the test. Good closure is seen for all helicity fractions, and no bias is observed.

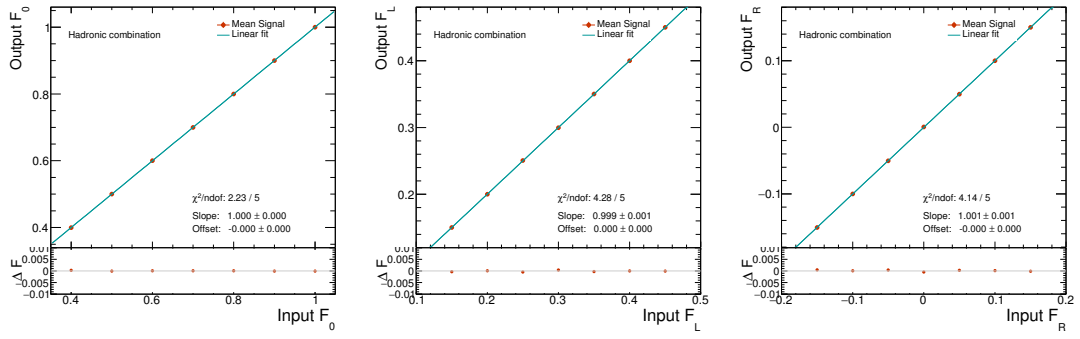

Figure 7.13.: Linearity checks for F_0, F_L, and F_R in the electron+muon channels with 1 b-tag + ≥ 2 b-tags regions for the hadronic analyser. 5000 sets of pseudo-data were fit to perform the test. Good closure is seen for all helicity fractions, and no bias is observed.

For each value of N_{nom} the pull distribution is obtained. The distribution of this quantity should follow standard normal distribution. Pull distributions provide evidence for various forms of biases and allow the verification of error coverage. For example, if the distribution is not centred around zero, it would be an indication of a bias in the measurement, or in case the width is smaller (larger) than unity, it would correspond to an error under (over)-estimate. Figure 7.14 presents the mean and width values of the pull distributions of the best combination for the leptonic and hadronic analysers. No significant deviations from the expectations are observed.

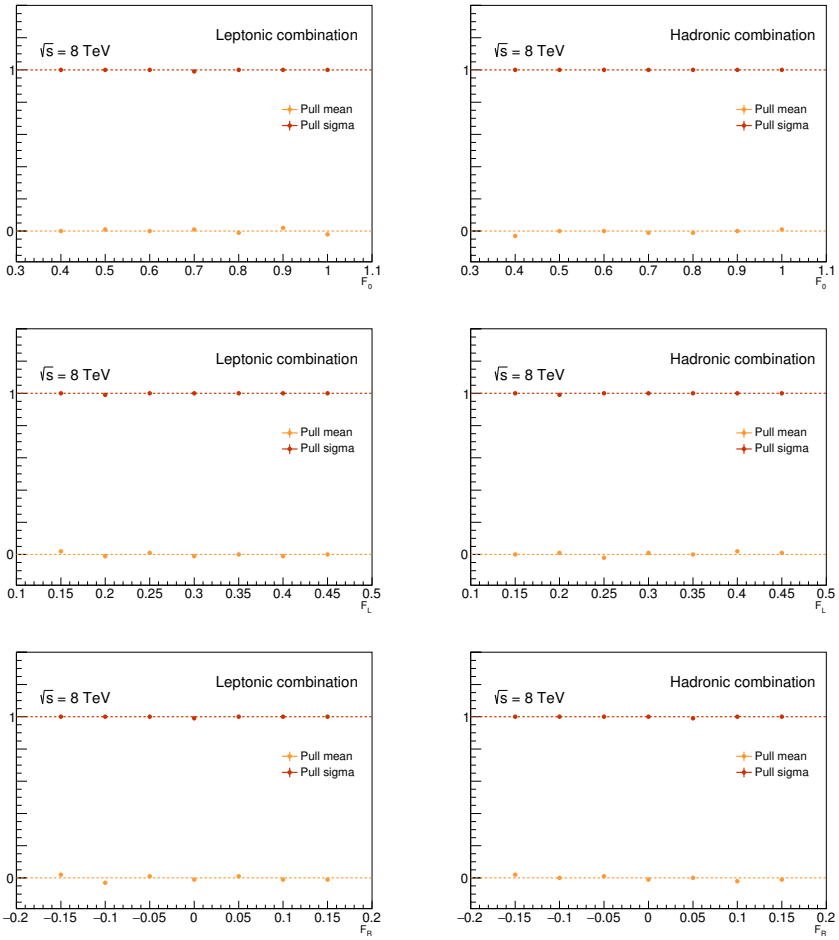

Figure 7.14.: Pull distributions summary for F_0, F_L, and F_R in the two-channel combination (electron + muon) with ≥ 2 b-tags obtained using the leptonic analyser (left column), and the four-channel combination (electron + muon) in the 1 b-tag + ≥ 2 b-tags regions obtained using the hadronic analyser (right column). 5000 sets of pseudo-data were fit to perform the test. Good match with the normal distribution is seen for all helicity fractions, and no bias is observed.

8

Uncertainty Evaluation

Measurements of any physical quantity can never be exact, but are subject to different types of uncertainties. In general, the associated uncertainties in high energy physics are categorised into statistical and systematic uncertainties.

The statistical uncertainty is always present in a physical measurement. It is the result of stochastic fluctuations arising from repeated measurements of the same phenomenon (in this analysis it is the measurement of $\cos\theta^*$ in each $t\bar{t}$ event) which result in a set of observations. The statistical uncertainty is a measure of the range of the variation in those observations. Estimation of the expected statistical uncertainty is detailed in Section 8.1.

Systematic uncertainties, on the other hand, arise from the imperfect modelling of the underlying physics processes and the detector response. These uncertainties affect the signal and background normalisation and/or the shape of the analyser's distribution. Due to the large number of $t\bar{t}$ signal events produced at the LHC, the measurement of the W boson polarisation is dominated by systematic uncertainties. A detailed discussion of sources of systematic uncertainties is presented in Section 8.2.

The estimation of systematic and expected statistical uncertainties is performed via ensemble tests. *Pseudo-data* distributions are obtained from MC simulation and scaled to the data statistics. Ensembles (*pseudo-experiments*) are obtained by fluctuating each bin of the pseudo-data distribution according to Poisson statistics. Five thousand pseudo-experiments are generated and the template fit is performed for each one using the templates introduced in Section 7.1. The result forms a Gaussian distribution for each helicity fraction. The width of this distribution yields the expected statistical uncertainty.

To evaluate the systematic uncertainties, the ensembles are generated from systemati-

cally varied pseudo-data distribution for each source of systematic uncertainty. The shift of the mean value of the corresponding Gaussian distribution with respect to the mean value of a reference distribution, e.g. nominal distribution or an independent reference, presents the corresponding systematic uncertainty.

8.1. Expected Statistical Uncertainty

As mentioned earlier, the expected statistical uncertainties are obtained from fits of five thousand ensembles produced from the nominal pseudo-data distribution, using the nominal templates. The width of the obtained Gaussian distribution corresponding to the measurement of each W boson polarisation state presents the corresponding uncertainty. Table 8.1 presents the statistical uncertainty expectation in the measurement of the W boson helicity fractions obtained using leptonic, hadronic and the combination of both analysers, categorised in $\geq$ 2 b-tags and in 1 b-tag + $\geq$ 2 b-tags channels. The e+jets and μ+jets channels are combined for each analyser. The normalisation of the background contributions is fixed in the fit during these tests in order to extract the pure statistical uncertainty.

Increasing the statistics by combining more channels, the sensitivities show better results as expected. The combination of all eight channels including both leptonic and hadronic analysers, provides the lowest expected statistical uncertainty.

As seen in Table 8.1, the expected statistical sensitivities are worse for the helicity fractions fit using the hadronic analyser than the leptonic one. This is a reflection of the imperfect matching of the up and down type jets from the decay of the hadronic W boson which results in a poor discrimination between the left- and right-handed templates. The sensitivity of the hadronic extraction is improved by requiring the logarithm of the likelihood of the leading permutation to be greater than -48. This optimisation is discussed in Section 6.2.4.

In order to quantify the impact of the likelihood cut on the leptonic channels, a study is performed to test the sensitivity of the leptonic measurement after applying this cut. Five thousand pseudo-experiments are performed to evaluate the sensitivity of the leptonic channel both with and without the likelihood cut. The sensitivity of the measurement with the combination of all eight channels is also evaluated when the likelihood cut is applied to both channels and when it is only applied to the hadronic channel. The results are summarised in same table and show negligible difference. Therefore, to simplify the combination of the leptonic and hadronic measurements, the same likelihood cut is

imposed on both leptonic and hadronic measurements. Using identical phase spaces for both measurements has the additional benefit of allowing the background templates to be treated as fully correlated in the fit for the leptonic+hadronic combinations.

Cut		2incl. b-tag	1excl+2incl b-tag
Leptonic analyser			
no LH cut	σ_{F_0}	0.010 ± 1.0%	0.009 ± 1.0%
	σ_{F_L}	0.006 ± 1.0%	0.005 ± 1.0%
	σ_{F_R}	0.005 ± 1.0%	0.004 ± 1.0%
log LH >-48	σ_{F_0}	0.012 ± 1.3%	0.010 ± 1.1%
	σ_{F_L}	0.008 ± 1.3%	0.006 ± 1.0%
	σ_{F_R}	0.006 ± 1.3%	0.004 ± 1.1%
Hadronic analyser			
log LH >-48	σ_{F_0}	0.012 ± 1.0%	0.010 ± 1.0%
	σ_{F_L}	0.022 ± 1.1%	0.021 ± 1.0%
	σ_{F_R}	0.022 ± 1.0%	0.021 ± 1.1%
Leptonic + hadronic combination			
log LH >-48 in the hadronic analyser	σ_{F_0}	0.008 ± 1.0%	0.007 ± 1.1%
	σ_{F_L}	0.005 ± 1.0%	0.004 ± 1.1%
	σ_{F_R}	0.004 ± 1.0%	0.003 ± 1.0%
log LH >-48 in both analysers	σ_{F_0}	0.008 ± 1.0%	0.007 ± 1.0%
	σ_{F_L}	0.006 ± 1.0%	0.005 ± 1.0%
	σ_{F_R}	0.004 ± 1.0%	0.004 ± 1.0%

Table 8.1.: Absolute statistical uncertainty expectations of the helicity fractions fitted using the leptonic, hadronic side and combined analysers in ≥ 2 b-tags and the combined $1 + \geq 2$ b-tags. The requirement of the leading log likelihood to be > -48 is applied to both hadronic and leptonic analysers. The combination of leptonic and hadronic analysers is also presented for both cut options. The background normalisation are fixed in the fit. The relative errors presenting the error in obtaining the Gaussian width of each helicity fraction distribution.

8.2. Systematic Uncertainties

The measurement of the W boson polarisation is subject to several systematic uncertainties, which are categorised in the following groups: uncertainties associated with reconstructed objects, uncertainties in signal and background modelling, method related uncertainties, and uncertainty in the luminosity measurement. Individual sources of systematic uncertainties are considered uncorrelated. Correlations of a given systematic

uncertainty are maintained across processes and channels. Table 8.2 presents a summary of the systematic uncertainties considered in the analysis indicating whether they are taken to affect normalisation or both shape and normalisation. Details about each systematic source are given in the following sections.

Systematic uncertainty	Type	Components
Luminosity	N	1
Physics Objects		
Electron	SN	5
Muon	SN	6
Jet energy scale	SN	26
Jet vertex fraction	SN	1
Jet energy resolution	SN	11
Jet reconstruction efficiency	SN	1
b-tagging efficiency	SN	6
c-tagging efficiency	SN	4
Light jet tagging efficiency	SN	12
Background Model		
W+light/c/bb/cc calibration	N	3
W+jets shape	S	1
Multijet normalisation	N	1
Z+jets normalisation	N	1
Single top cross section	N	1
Diboson+jets normalisation	N	1
Signal Model		
$t\bar{t}$ Radiation	SN	2
$t\bar{t}$ MC Generator	SN	1
$t\bar{t}$ Showering & Hadronisation	SN	1
$t\bar{t}$ PDF	SN	3
Top mass	SN	1
Method related		
Template Statistics	SN	1

Table 8.2.: List of systematic uncertainties considered. "N" ("S") represents uncertainties only affecting the normalisation (shape) for all processes and channels. whereas "SN" means that the uncertainty is affecting both shape and normalisation. Some of the systematic uncertainties are split into several different components for a more accurate treatment (number indicated under the column labelled as "Components").

8.2.1. Luminosity

The luminosity estimate has an uncertainty of 1.9% in the $\sqrt{s} = 8$ TeV dataset [81]. In this analysis, the uncertainty in the luminosity estimate only affect the normalisation of single top, Z+jets and diboson backgrounds, which are grouped as remaining background component in the fit[1]. Furthermore, the normalisation of each background processes is constrained in the fit. On the other hand, the impact of luminosity uncertainty is fully correlated between the contributions of the three polarisation states (N_is in Equation 7.1). Therefore, it is expected that the effect cancels out in the calculation of the helicity fractions. The impact of the luminosity uncertainty on measuring the helicity fractions has been evaluated and found to be in order of $< 10^{-6}$ and hence it is considered as negligible.

8.2.2. Uncertainties Associated with Reconstructed Objects

Every measuring instrument/device has an inherent uncertainty which is determined by the precision of the instrument. Consequently, the reconstruction of the objects discussed in Chapter 4 are associated with different systematic uncertainties. The following subsections detail the systematic uncertainty sources which are considered in this analysis.

Lepton Reconstruction, Identification and Trigger

The measured reconstruction and identification and trigger efficiencies of electrons and muons differ between data and simulation. Scale factors are derived using tag-and-probe techniques described in Refs. [90, 92, 93]. The $Z \to \ell^+\ell^-$ ($\ell = e, \mu$), $J/\psi \to \ell^+\ell^-$ and $W \to e\nu$ processes in data are compared to the simulated samples to correct the simulation for the discrepancies. The scale factors are derived in bins of η and E_T (p_{T}) for electrons (muons). Therefore, the uncertainties associated with those factors are affecting both the shape and the normalisation of the distribution of the analysers.

Lepton Momentum Scale and Resolution

The reconstructed distributions of $Z \to \ell^+\ell^-$ and $J/\psi \to \ell^+\ell^-$ masses are compared to the simulated events to estimate the accuracy of lepton momentum scale and resolution in the simulation. In addition to these processes, $W \to e\nu$ events are also used for the electron case. The observed discrepancies between data and simulation were found to

[1] The normalisation of W+jets and fake leptons are estimated via a data driven method (see Section 5.5)

be small. For electrons, the correction is applied to both data and simulation, while in the case of muons, momentum scale and resolution corrections are only applied to the simulation. Uncertainties on momentum scale and resolutions in the muon spectrometer and the tracking systems are considered, and varied separately [159, 160].

In total, there are five (six) uncertainty components considered for electrons (muons).

Jet Reconstruction Efficiency

The jet reconstruction efficiency for jets with a p_{T} between 20 and 30 GeV is overestimated in MC simulations [161]. A systematic uncertainty is considered to take this effect into account. Reconstructed jets are randomly rejected in the simulation according to the mismatch in efficiency to lower the efficiency in the MC sample by about 0.2% for the affected jets. The analysis is repeated with the reduced set of jets and the difference to the nominal selection is quoted as uncertainty in jet reconstruction efficiency.

Jet Vertex Fraction Efficiency

As mentioned in Section 4.5, to avoid selecting jets from secondary pp interactions, a selection on the JVF variable (see section 4.5.1) above 0.5 is applied to jets with $p_{\mathrm{T}} < 50$ GeV. The uncertainty on the JVF selection is propagated to the W boson helicity measurement by changing the nominal JVF cut value by $\pm$ 0.1 and repeating the analysis using the modified cut value. The difference to the nominal selection is quoted as uncertainty on the jet vertex fraction efficiency[162].

Jet Energy Scale

The jet energy scale (JES) and its uncertainty have been derived from the combined information of test-beam data, LHC collision data as well as Monte Carlo simulation [161, 163–166]. The JES uncertainty is parametrised in jet η and p_{T} and is split into 26 uncorrelated sources in the 8 TeV analyses which are treated independently:

- **in situ calibration (15):** well-calibrated objects are used as reference to calibrate JES in data. In the central rapidity region, $|\eta| < 0.8$, in situ calibration methods are applied using the p_{T} Direct Balance (DB) between Z/γ and a jet, or p_{T} balance between Z/γ and the hadronic recoil for high p_{T} jets, which is known as the Missing Projection Fraction (MPF) technique. In these methods, the data-to-MC ratio is used as a residual correction. This correction is applied to the data in addition to

the simulation-based corrections, in order to improve the jet energy measurement. The systematic effects in the selection, modelling and calibration of the reference objects are propagated to the calibration factors and evaluated by shifting up and down the energy (or momentum) of those reference objects accordingly [102]. The uncertainties associated with the in situ calibration are categorised as: detector description (3), statistics (4), physics modelling (4) and mixed detector and modelling (4). Figure 8.1 shows the corresponding uncertainties on the jet response[2] ratio of the data and MC simulation for various in situ techniques in the central rapidity region as a function of jet p_{T}.

- **η-intercalibration (2):** in order to improve the in situ calibration in the forward rapidity region with respect to the central region, p_{T} balance in dijet events between a well calibrated jet in the central region and a jet in the forward region is used. The corresponding uncertainty is composed of a statistical component and a MC modelling component.

- **pile-up (5):** uncertainties of the pile-up correction in the jet energy arise from mismodelling of the pile-up effect on simulated jets, uncertainty on the number of reconstructed primary vertices and the average number of interactions per bunch crossing.

- **jet flavour composition and response (2):** in order to cope with the unequal calorimeter response for different jet flavour types, differences between light quark- and gluon-initiated jets from MC simulations are taken into account as uncertainties in the jet energy.

- ***b*-JES (1):** the different calorimeter response of b-jets with respect to other quark-initiated jets is taken into account as an uncertainty on the jet energy.

- **high p_{T} jets (1):** for high p_{T} jets, $p_{\mathrm{T}} > 1$ TeV, JES uncertainties are derived from single-particle response measurements [161], where the uncertainty in the calorimeter response to jets is obtained from the response uncertainty on the individual jet constituting particles.

In Figure 8.2, the fractional jet energy scale uncertainty components are compared to the total JES uncertainty for the analysed 2012 dataset. As shown, the dominant JES

[2]The jet response is defined using the associated particle jet kinematics as $R =< p_T^{\mathrm{jet}}/p_T^{\mathrm{truth}} >$

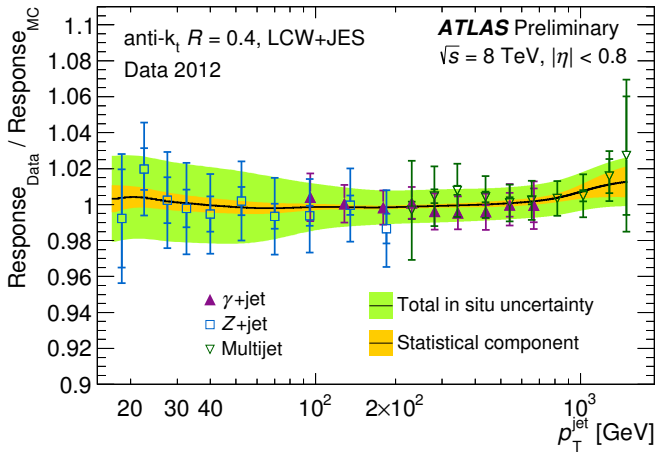

Figure 8.1.: Jet response ratio of the data to MC as a function of p_{T} for three in situ techniques combined to determine the in situ energy scale correction: Z+jet, γ+jet and multijet events. The error bars indicate the statistical and the total uncertainties. The results are shown for anti-k_t jets with radius parameter of R = 0.4 calibrated with the LCW+JES scheme. The result of the combination of the in situ techniques is shown as the dark line with the total uncertainty (outer green band) and statistical uncertainty (inner orange band) [167].

component for the higher p_{T} jets is the in situ JES uncertainty. The impact of pile-up is significant for the low p_{T} jets, but becomes negligible as the p_{T} raises. On the other hand, for a fixed jet p_{T}, the JES uncertainty is driven by in situ contribution in the forward rapidity region, while the contribution of the flavour response is dominant in the central region.

Jet Energy Resolution

The jet energy resolution (JER) is determined from the width of the p_{T} balance distribution, measured using the DB method in Z/γ +jet events [102]. The reconstructed jet that passes the selection of the DB is required to be matched to a truth-jet[3]. The JER uncertainty is estimated via:

$$\sigma_{\text{in situ}} = \sqrt{(\sigma(p_T^{\text{jet}}/p_T^{\text{ref}}))^2 - (\sigma(p_T^{\text{truth-jet}}/p_T^{\text{ref}}))^2}, \tag{8.1}$$

[3]The energies of all truth particles associated with a given reconstructed jet are summed. If this summed energy is greater than 50% of the energy of the particle-level jet (truth-jet), the reconstructed jet is considered matched to the truth-jet

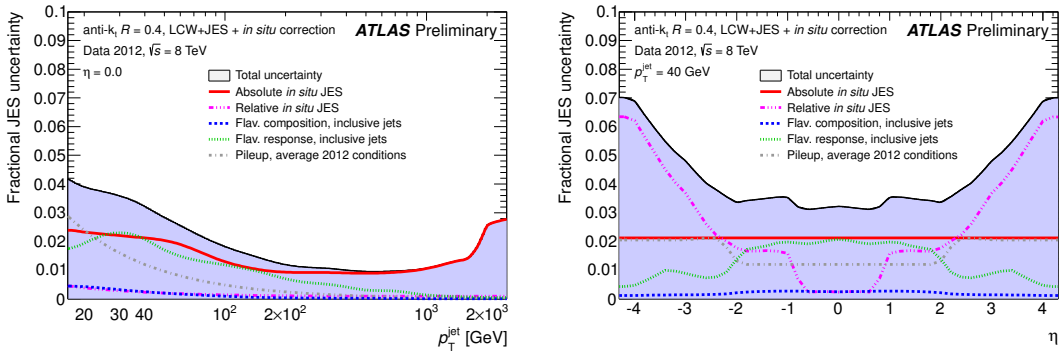

(a) (b)

Figure 8.2.: Fractional jet energy scale systematic uncertainty components as a function of (a): p_{T} for jets with $|\eta| = 0.0$, and (b): η for jets with $p_{\mathrm{T}} = 40$ GeV, calibrated using the LCW+JES calibration scheme. The total uncertainty (quadrature sum of all components) is shown as a filled blue region topped by a solid black line. Average 2012 pileup conditions are used, and flavour response and composition are taken from inclusive dijet samples [167].

where p_T^{ref} represents the transverse momentum of the reference jet.

Alternatively, in MC simulation, the JER can be determined by comparing the reconstructed jet with its corresponding matched truth-jet and probing the width of the $(p_T^{\mathrm{jet}}/p_T^{\mathrm{ref}})$ distribution. The JER measurement using these methods has a 10-20 % systematic difference, which is taken as a JER systematic uncertainty.

Using the truth-jet in the in situ measurement of the JER depends on the choice of the MC generator. Therefore, the $\sigma_{\mathrm{in\ situ}}$ in Equation 8.1 is estimated with an alternative MC generator and the difference is taken as systematic uncertainty in JER determination. Other systematic uncertainties sources are the same as those considered for the JES determination.

The effect of the total jet energy resolution is parametrised as the sum of terms relating electronic and pile-up noise, a term arising from the stochastic effect due to the sampling nature of the calorimeters, and a constant p_{T} independent term (see Section 3.2.3). To account for correlations between the measurements at different $|\eta|$, a correlation matrix as a function of p_{T} and $|\eta|$ is built. An eigenvector reduction is performed which results in a maximum of twelve additional nuisance parameters which describe all correlations between the p_{T} and $|\eta|$ regions covered by the *in situ* studies. In total, eleven orthogonal nuisance parameters are used to estimate the total systematic effect of the jet energy resolution.

Figure 8.3 shows different contributions to the jet energy resolution uncertainty, obtained by using Z+jet events. The large uncertainty in the high-p_T^{ref} for LCW+JES jets is due to statistical fluctuations. As seen in the plots, the uncertainties due to the choice of the MC generator, non-closure and limited statistics constitute the dominant uncertainty sources.

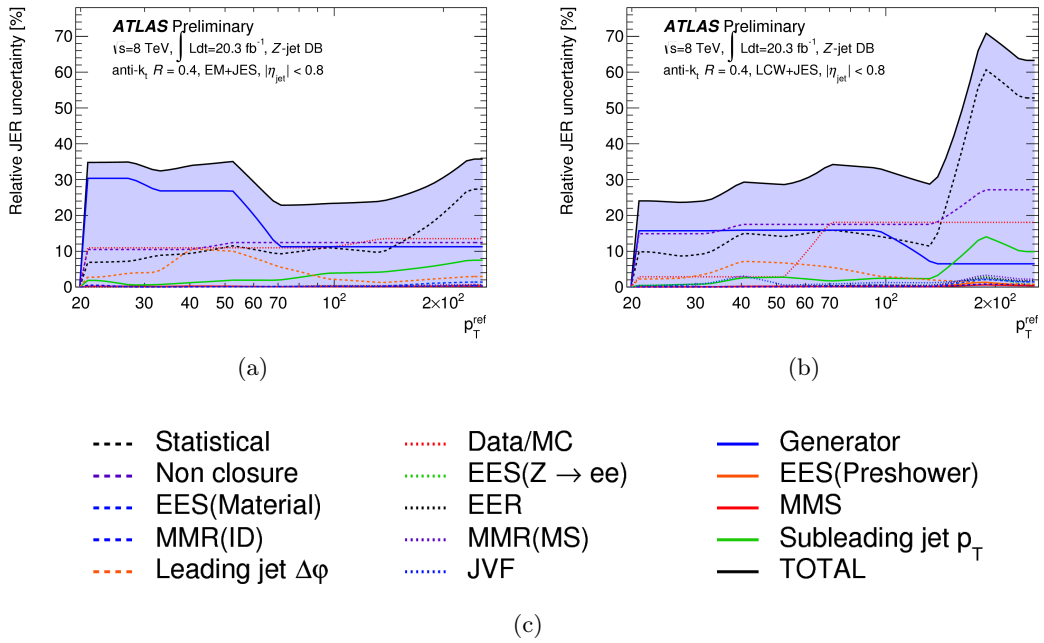

Figure 8.3.: Summary of the uncertainties in the data-to-MC ratio of the JER calibrated with the (a) EM+JES and (b) LCW+JES schemes. Resolutions are computed using the direct balance method in Z+jet events. Legend with the systematic uncertainties representation is presented in (c) [102].

Heavy- and Light-Flavour Tagging

As discussed in Section 4.5.2, p_{T}-dependent scale factors are derived to reduce the discrepancy between the measured efficiencies for b-tagging, c-tagging and mistag rate in MC and data. These scale factors are accompanied by systematic uncertainties and are applied to each jet in the simulation depending on its flavour and p_{T}. In the case of light-flavour jets, the corrections also depend on jet η.

The corresponding uncertainties are split into sub-components via the *eigenvector method*. A total of six independent sources of uncertainty affecting the b-tagging effi-

ciency and four affecting the c-tagging efficiency are considered. Each of these uncertainties correspond to a resulting eigenvector after diagonalising the matrix containing the information of total uncertainty per p_{T} bin and the bin-to-bin correlations. Twelve uncertainties are considered for the efficiency of light jet tagging which depend on six jet p_{T} bins and two η regions. These systematic uncertainties are taken as uncorrelated between b-jets, c-jets, and light flavour jets.

8.2.3. Uncertainties in the Background Estimates

W+jets Modelling

As explained in Section 5.5.2, a W boson charge asymmetry based data driven method is employed to calibrate different flavour components of the W+jets background for the given Monte Carlo samples [140]. The uncertainty in those calibration factors (5% for W+light-jets, 25% for W + c-jets and 7% for W + bb/cc-jets) is used as a Gaussian constraint for the W+jets normalisation in the likelihood fit introduced in Section 7.1.3, where each W+jets component is allowed to vary independently.

In addition to that, by independently varying each flavour component of the W+jets by its uncertainty, with the other two components fixed to their respective normalisations, the overall shape of the W+jets background is varied. The impact of this change on the W boson helicity fractions measurement is evaluated. The total shape uncertainty is then estimated from the envelope of each flavour component variations. The impact is found to be negligible.

Fake-lepton

The fake lepton background is estimated in different regions via the matrix method introduced in Section 5.5.1. A conservative normalisation uncertainty of 30% is assigned independently to the electron and muon channels and to each b-tag region [146].

Remaining Background Sources

As discussed in Section 7.1.1, one template is considered to account for the backgrounds from single top, Z+jets and diboson processes. Therefore, the overall normalisation uncertainty for this combination is considered as a weighted average of the normalisation uncertainties associated to those background components.

For the single top quark production, a normalisation uncertainty of 17% is considered, which takes into account the weighted average of the theoretical uncertainties in s-, t- and Wt-channel production (+5%/- 4%) [142–144] as well as additional uncertainties due to variations in the amount of initial- and final-state radiation and the extrapolation to high jet multiplicity.

The uncertainty in the single top background shape is assessed by comparing Wt-channel MC samples generated using alternative approaches (diagram removal and diagram subtraction) to take into account interference of the Wt and $t\bar{t}$ diagrams [168]. The impact on the W boson helicity fractions measurement due to the change in single top samples is found to be negligible ($\mathcal{O}(10^{-5})$) for all fractions.

In general, the $\cos\theta^*$ template for the single top background depends on the W boson helicity fractions. In order to investigate its possible effect on the measurement, alternative templates of t-channel single top background (as the dominant single top production channel) are produced using samples generated with anomalous Wtb couplings which corresponds to non-SM helicity fractions. The samples are generated with Protos LO event generator [65, 169], interfaced with Pythia 6 to model the showering and hadronisation. The left-handed vector (right-handed tensor) coupling is varied between 0.99 and 0.96 (-0.09 to +0.23). The impact on the measurement of W boson helicity fractions was also observed to be negligible ($\mathcal{O}(10^{-4})$).

An overall normalisation uncertainty of 48% is applied to both Z+jets and diboson contributions. It takes into account a 5% uncertainty in the theoretical (N)NLO cross section [127, 137] and a 24% uncertainty on the extrapolation to higher jet multiplicities, added in quadrature for each jet.

8.2.4. Signal Modelling

Signal modelling is accompanied by several sources of systematic uncertainties, which affect the kinematic properties of simulated $t\bar{t}$ events. Therefore, the acceptance and the shape of the reconstructed $\cos\theta^*$ distribution are subject to change. These uncertainty sources are discussed in more details in the following.

Monte Carlo Generators

An uncertainty due to the choice of the matrix element MC generator for the hard process is evaluated by comparing events produced by Powheg-Box and MC@NLO, both interfaced to Herwig to model the showering and hadronisation. The full symmetrised

difference is taken as systematic uncertainty.

Parton Showering and Hadronisation

To cope with the impact of the different parton shower and hadronisation models, the generated events with POWHEG are interfaced with HERWIG and compared with those events interfaced with PYTHIA. The full symmetrised difference is taken as systematic uncertainty.

Initial and Final State Radiation

The uncertainties due to QCD initial- and final-state radiation (ISR/FSR) modelling are estimated using two alternative signal samples generated with POWHEG-BOX interfaced to PYTHIA, that use varied values for the factorisation scale (μ is varied from 0.5 to 2), the h_{damp} parameter responsible for high p_{T} radiation damping in the event generator ($h_{damp} = m_t$ for $\mu = 2$ and $h_{damp} = 2m_t$ for $\mu = 0.5$), and the transverse momentum scale of space-like parton-shower evolution in PYTHIA, to produce more and less radiation in the event. The variations span the ranges compatible with the results of measurements of $t\bar{t}$ production in association with jets. The variation with the largest effect on the measured helicity fractions with respect to the nominal sample is taken as the total radiation uncertainty and symmetrised.

Top Quark Mass

The $t\bar{t}$ sample is generated with a top quark mass of m_t =172.5 GeV. In the reconstruction, the top mass has been fixed to this value. In order to evaluate the uncertainty due to the choice of top quark mass in the event generator, alternative MC samples generated with different input top masses used in place of the default sample. The dependence of the obtained helicity fractions on the top quark mass is fitted with a linear function. The uncertainties in the measurement of the W boson helicity fractions are obtained from the slope multiplied by uncertainty in the latest top quark mass measurement of 172.84 $\pm$ 0.70 GeV [136] measured by ATLAS at $\sqrt{s} = 8$ TeV. Figure 8.4 and 8.5 show the W boson helicity fractions obtained as a function of top quark mass for the best combination for the leptonic and hadronic analysers.

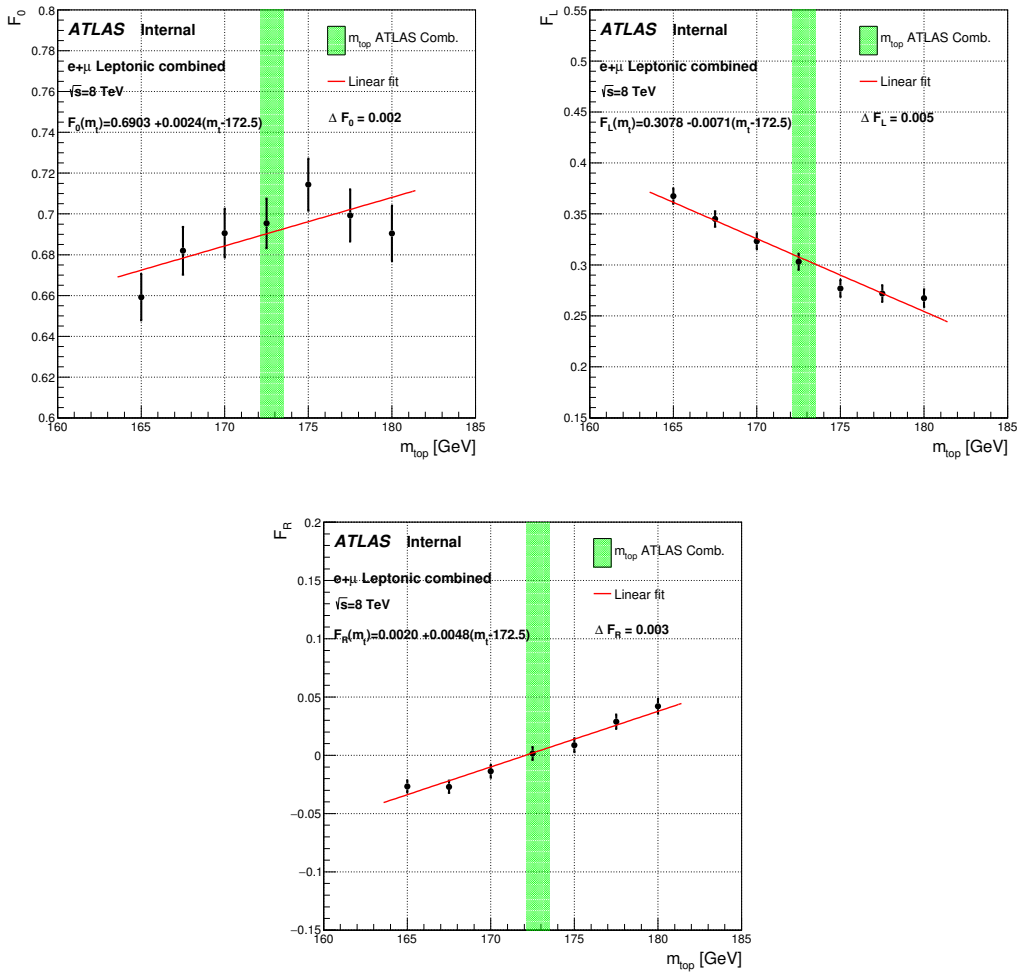

Figure 8.4.: The helicity fractions as a function of top mass obtained using the leptonic analyser in electron + muon channels with ≥ 2 b-tags.

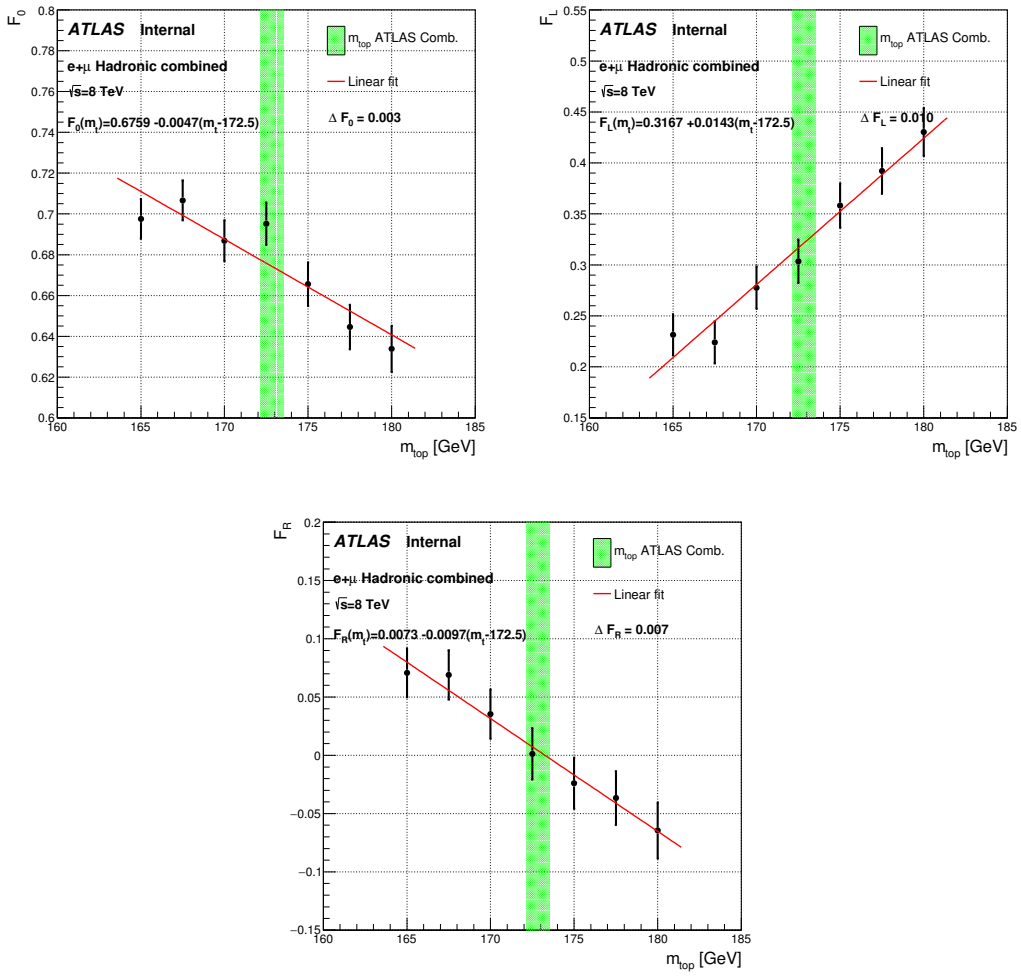

Figure 8.5.: The helicity fractions as a function of top mass obtained using the hadronic analyser in electron + muon channels, in 1 b-tag + ≥ 2 b-tags regions.

Parton Density Functions

The uncertainty due to the choice of the PDF set is evaluated using an aMC@NLO $t\bar{t}$ sample following the recommendation of the *PDF4LHC* working group [170]. Three PDF sets - CT10 NLO [122], MSTW2008 68% CL NLO [134, 135] and NNPDF 2.3 NLO [52] are compared. Each PDF set is accompanied by a set of uncertainties (52 uncertainties for CT10, 40 for MSTW and 100 for NNPDF), where the $\cos\theta^*$ distribution of the $t\bar{t}$ signal is reweighted using the LHAPDF tool [171] for each given variation.

Three different methods are used to evaluate the PDF uncertainty: symmetric Hessian for CT10, asymmetric Hessian MSTW and sample standard deviation for NNPDF. The final uncertainty is an envelope of a) intra-PDF uncertainty, which evaluates the changes due to the variation of different PDF parameters within a single PDF error set, and b) inter-PDF uncertainty, which evaluates differences between different PDF sets. Half width of the envelope of the three estimates is taken as PDF systematic uncertainty.

The corresponding plots are shown in Figures 8.6 and 8.7 for the best combination for the leptonic and hadronic analysers.

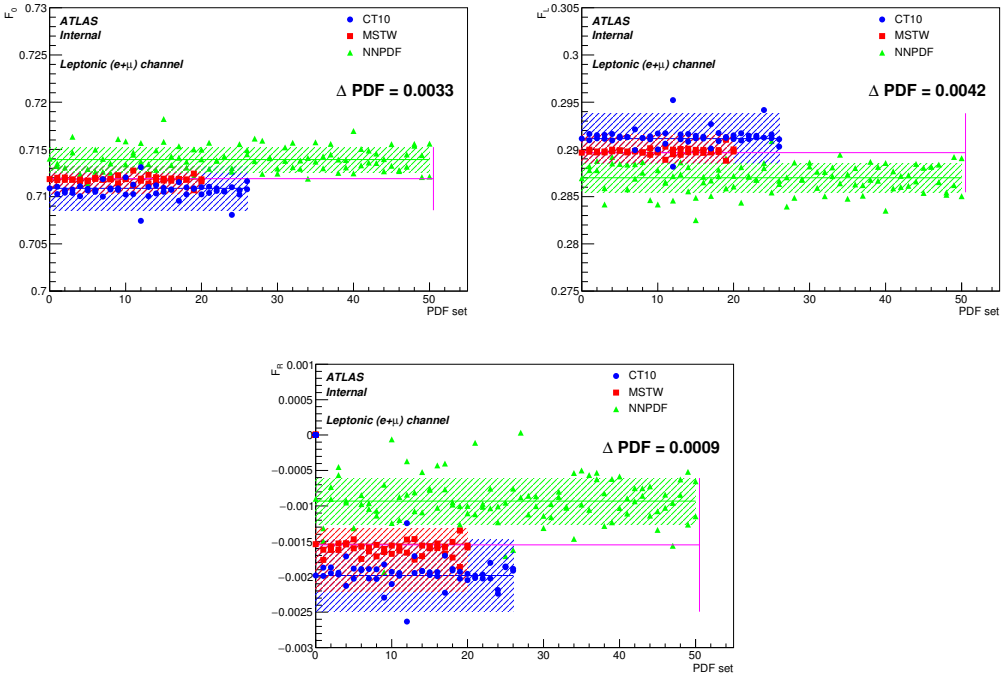

Figure 8.6.: The helicity fractions for different PDF sets obtained using the leptonic analyser in electron + muon channels with ≥ 2 b-tags.

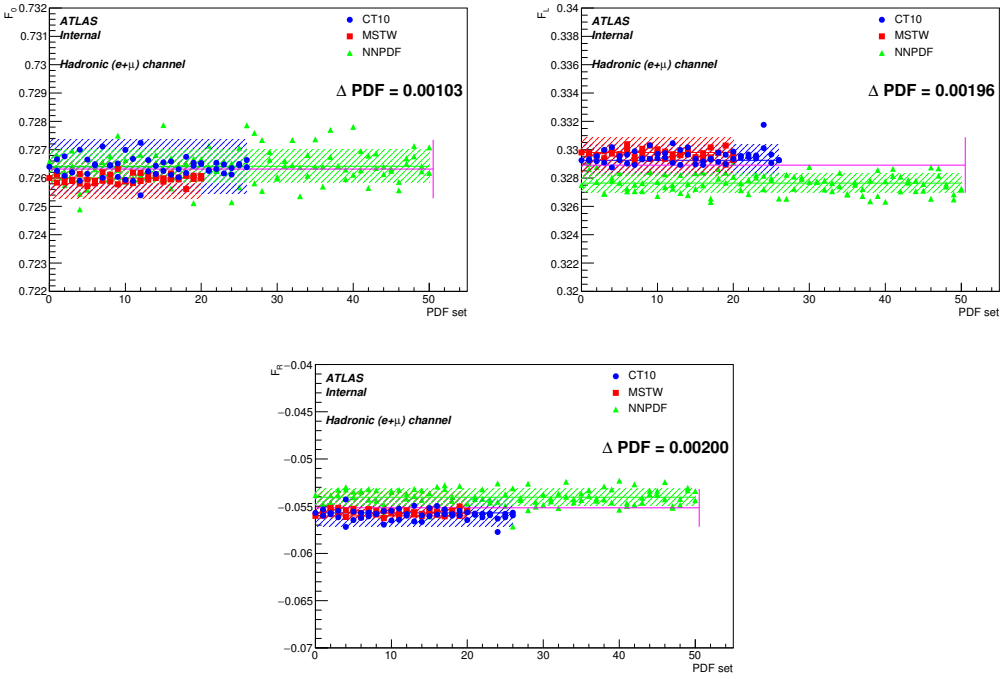

Figure 8.7.: The helicity fractions for different PDF sets obtained using the hadronic analyser in electron + muon channels, in 1 b-tag + ≥ 2 b-tags regions.

8.2.5. Method related Uncertainties

Template Statistics Uncertainty

To account for possible fluctuations in the templates, ensemble tests are performed. In these ensemble tests, the pseudo data distribution is not changed, but the template distributions are fluctuated within their sample statistical error. The width of the distributions for the W boson helicity fractions is taken as a measure of the uncertainty that arises due to the limited template statistics. The result is comparable to the statistical uncertainty and mainly originates from the signal templates due to the reweighting method. Table 8.3 presents the uncertainty contribution due to the signal and each background templates statistics.

Template	≥ 2 b-tags			1+≥ 2 b-tags		
	F_0	F_L	F_R	F_0	F_L	F_R
	Leptonic analyser					
Signal ($t\bar{t}$)	0.009	0.005	0.004	0.007	0.004	0.003
Fake leptons	0.001	0.001	0.001	0.002	0.001	0.001
W+jets	0.002	0.001	0.001	0.002	0.001	0.001
Rem. backgrounds	0.002	0.001	0.001	0.002	0.001	0.001
Total	0.009	0.006	0.004	0.008	0.005	0.004
	Hadronic analyser					
Signal ($t\bar{t}$)	0.008	0.015	0.015	0.007	0.015	0.014
Fake leptons	0.001	0.003	0.003	0.001	0.003	0.003
W+jets	0.002	0.004	0.004	0.002	0.004	0.005
Rem. backgrounds	0.002	0.004	0.005	0.002	0.004	0.004
Total	0.009	0.017	0.017	0.008	0.016	0.016
	Leptonic + hadronic combination					
Signal ($t\bar{t}$)	0.006	0.004	0.003	0.005	0.003	0.003
Fake leptons	0.001	0.001	0.001	0.001	0.001	0.001
W+jets	0.001	0.001	0.001	0.002	0.001	0.001
Rem. backgrounds	0.002	0.001	0.001	0.001	0.001	0.001
Total	0.006	0.004	0.004	0.005	0.004	0.003

Table 8.3.: The uncertainty in measuring the W boson helicity fractions due to limited MC template statistics.

8.2.6. Significance of Systematic Uncertainty

As discussed in Section 7.1, a dedicated pseudo-data distribution is produced for each individual source of systematic uncertainty. The systematically varied ensembles are fitted with the nominal templates in a likelihood fit to evaluate the effect of each corresponding uncertainty. This procedure only makes sense when the difference between the nominal distribution and a given systematically varied distribution is larger than the statistical uncertainty on the Monte Carlo yield of the nominal sample. Therefore, a systematic variation is considered significant if: a) the difference between the total yield of the varied $\cos\theta^*$ distribution and the total nominal yield is larger than the total nominal MC statistical uncertainty, or b) if the difference in per bin yield between the nominal sample and a variation is larger than the nominal MC uncertainty in at least two bins. All varied $\cos\theta^*$ distributions are compared with the nominal distribution. The significant systematic uncertainty sources are listed in Table 8.4. All sources of systematic uncertainties that are represented by scale factors applied on the nominal distribution are considered in the total systematic uncertainty, since they are evaluated using the same events and thus have no statistical component.

Considering the above conditions, the estimated uncertainties in the W boson helicity fractions measurement for the best combination for the leptonic and hadronic analysers are summarised in Tables 8.5- 8.7. The result of the full combination, i.e. the eight-channel combination of the electron and muon channels of leptonic and hadronic analysers with 1 b-tag + ≥ 2 b-tags, is also presented for comparison.

Significant Systematic uncertainty	Leptonic 2incl. b-tag	Hadronic 1excl+2incl b-tag
ELE_RECO	✓	✓
ELE_ID	✓	✓
ELE_TRIGGER	✓	✓
MUON_RECO	✓	✓
MUON_ID	✓	✓
MUON_TRIGGER	✓	✓
JES_EffectiveNP_Modelling1	✓	✓
JES_EffectiveNP_Statistical1	✗	✓
JES_EtaIntercalibration_TotalStat	✗	✓
JES_FlavourComp	✓	✓
JES_FlavourResponse	✓	✓
JES_RhoTopology	✓	✓
JER	✗[a]	✓
JVF	✓	✓
BTAG_btag[b]	✓	✓
BTAG_ctag	✓	✓
BTAG_mistag	✓	✓
Radiation	✓	✓
MC Generator	✓	✓
Showering & Hadronisation	✓	✓
PDF	✓	✓
TopMass	✓	✓
Template statistics	✓	✓

Table 8.4.: List of significant systematic uncertainties considered .

[a] Only jer_NP0 is significant in the leptonic analyser

[b] All b-tagging uncertainty components are considered since they are applied as scale factors to the nominal $\cos\theta^*$ distribution.

		F_0		
Systematic uncertainty	N_{syst}	Lep. ≥ 2 b-tags	Had. $1+\geq 2$ b-tags	Lep+Had $1+\geq 2$ b-tags
Reconstructed Objects				
Muon	6(3)	+0.0024 -0.0029	+0.0026 -0.0037	+0.0026 -0.0026
Electron	5(3)	+0.0028 -0.003	+0.0025 -0.0021	+0.0026 -0.003
JES	26(6)	+0.0063 -0.0033	+0.0069 -0.007	+0.0077 -0.009
JER	11(11)	+0.0062 -0.0059	+0.0274 -0.031	+0.0068 -0.0068
JVF	1(1)	+0.0036 -0.0017	+0.0129 -0.0092	+0.0025 -0.0015
b-tagging	3(3)	+0.0017 -0.0021	+0.0289 -0.0307	+0.0213 -0.0211
Sum of Reco. Objects	-	+0.0104 -0.0084	+0.0426 -0.0454	+0.0241 -0.0243
Modelling				
Radiation	radLo radHi	+0.0033 -0.0025	+0.0178 -0.0108	-0.0079 +0.0025
Parton Shower	1(1)	+0.0019 -0.0019	+0.015 -0.015	+0.0072 -0.0072
ME Generator	1(1)	+0.0025 -0.0025	+0.0159 -0.0159	+0.0019 -0.0019
PDF	3(3)	+0.003 -0.003	+0.001 -0.001	+0.002 -0.002
Top Mass	3(3)	+0.002 -0.002	+0.003 -0.003	+0.001 -0.001
Sum of Modelling	-	+0.0058 -0.0058	+0.0284 -0.0284	+0.0111 -0.0111
Method Uncertainty				
Template Statistics	3(3)	+0.009 -0.009	+0.008 -0.008	+0.005 -0.005
Total Syst.	-	+0.0149 -0.0136	+0.0518 -0.0541	+0.027 -0.0271
Stat. + Bkg.	-	0.012	0.010	0.007

Table 8.5.: Summary of systematic and statistical errors in the measurement of F_0. The errors are obtained using the leptonic (hadronic) analyser with ≥ 2 b-tags ($1+\geq 2$ b-tags), and eight-channel combination using both analysers. The numbers in parentheses in the N_{syst} column refer to the significant systematic components discussed in Section 8.2.6. Systematic uncertainties are grouped by their positive/negative impact on the W boson helicity fractions measurement. One-sided sources of systematic errors are symmetrised. For the radiation uncertainty, the larger of the two variations is taken as the total uncertainty and symmetrised. When the difference between the up and down total systematic uncertainty is less than 0.015, the magnitude of the larger uncertainty is taken as the total symmetrised uncertainty.

		F_L		
Systematic uncertainty	N_{syst}	Lep $\geq$ 2 b-tags	Had 1+$\geq$ 2 b-tags	Lep+Had 1+$\geq$ 2 b-tags
Reconstructed Objects				
Muon	6(3)	+0.0013 -0.0015	+0.0046 -0.0035	+0.0011 -0.0008
Electron	5(3)	+0.0018 -0.002	+0.0028 -0.0038	+0.0011 -0.0014
JES	26(6)	+0.0028 -0.0025	+0.0119 -0.0078	+0.0022 -0.0032
JER	11(11)	+0.0048 -0.0018	+0.0329 -0.0407	+0.0043 -0.0019
JVF	1(1)	+0.0019 -0.0013	+0.0012 -0.0046	+0.0021 -0.0017
b-tagging	3(3)	+0.0012 -0.0013	+0.0132 -0.0143	+0.0082 -0.0078
Sum of Reco Objects	-	+0.0064 -0.0044	+0.0378 -0.0444	+0.0099 -0.009
Modeling				
Radiation	radLo radHi	-0.0032 +0.0058	+0.0393 -0.0115	-0.006 +0.0076
Parton Shower	1(1)	+0.0019 -0.0019	+0.001 -0.001	+0.0086 -0.0086
ME Generator	1(1)	+0.0032 -0.0032	+0.0242 -0.0242	+0.0016 -0.0016
PDF	3(3)	+0.003 -0.003	+0.001 -0.001	+0.002 -0.002
Top Mass	3(3)	+0.002 -0.002	+0.003 -0.003	+0.001 -0.001
Sum of Modeling	-	+0.0078 -0.0078	+0.0463 -0.0463	+0.0118 -0.0118
Method Uncertainty				
Template Statistics	3(3)	+0.009 -0.009	+0.008 -0.008	+0.005 -0.005
Total Syst.	-	+0.0135 -0.0127	+0.0603 -0.0646	+0.0162 -0.0157
Stat. + Bkg.	-	0.012	0.010	0.007

Table 8.6.: Summary of systematic and statistical errors in the measurement of F_L. The errors are obtained using the leptonic (hadronic) analyser in $\geq$ 2 b-tags (1+$\geq$ 2 b-tags), and eight-channel combination using both analysers. The numbers in parentheses in the N_{syst} column refer to the significant systematic components discussed in Section 8.2.6. Systematic uncertainties are grouped by their positive/negative impact on the helicity fractions measurement. One-sided sources of systematic errors are symmetrised. For the radiation uncertainty, the larger of the two variations is taken as the total uncertainty and symmetrised. When the difference between the up and down total systematic uncertainty is less than 0.015, the magnitude of the larger uncertainty is taken as the total symmetrised uncertainty.

		F_R		
Systematic uncertainty	N_{syst}	Lep ≥ 2 b-tags	Had 1+≥ 2 b-tags	Lep+Had 1+≥ 2 b-tags
Reconstructed Objects				
Muon	6(3)	+0.001 -0.0015	+0.0072 -0.0072	+0.0015 -0.0017
Electron	5(3)	+0.0011 -0.0011	+0.0051 -0.0058	+0.0015 -0.0017
JES	26(6)	+0.0037 -0.0014	+0.0139 -0.0054	+0.0073 -0.0061
JER	11(11)	+0.0072 -0.0067	+0.0573 -0.0707	+0.0076 -0.0065
JVF	1(1)	+0.0017 -0.0006	+0.0114 -0.0045	+0.0003 -0.0002
b-tagging	3(3)	+0.0011 -0.0012	+0.0336 -0.0349	+0.0132 -0.0132
Sum of Reco Objects	-	+0.0085 -0.0072	+0.0694 -0.0797	+0.017 -0.0161
Modeling				
Radiation	radLo radHi	-0.0001 -0.0034	-0.0573 +0.022	+0.014 -0.0101
Parton Shower	1(1)	+0.0037 -0.0037	+0.0144 -0.0144	+0.0013 -0.0013
ME Generator	1(1)	+0.0057 -0.0057	+0.0401 -0.0401	+0.0033 -0.0033
PDF	3(3)	+0.003 -0.003	+0.001 -0.001	+0.002 -0.002
Top Mass	3(3)	+0.002 -0.002	+0.003 -0.003	+0.001 -0.001
Sum of Modeling	-	+0.0084 -0.0084	+0.0715 -0.0715	+0.0146 -0.0146
Method Uncertainty				
Template Statistics	3(3)	+0.009 -0.009	+0.008 -0.008	+0.005 -0.005
Total Syst.	-	+0.0149 -0.0142	+0.0999 -0.1074	+0.023 -0.0223
Stat. + Bkg.	-	0.012	0.010	0.007

Table 8.7.: Summary of systematic and statistical errors in the measurement of F_R. The errors are obtained using the leptonic (hadronic) analyser in ≥ 2 b-tags (1+$\geq$ 2 b-tags), and eight-channel combination using both analysers. The numbers in parentheses in the N_{syst} column refer to the significant systematic components discussed in Section 8.2.6. Systematic uncertainties are grouped by their positive/negative impact on the helicity fractions measurement. One-sided sources of systematic errors are symmetrised. For the radiation uncertainty, the larger of the two variations is taken as the total uncertainty and symmetrised. When the difference between the up and down total systematic uncertainty is less than 0.015, the magnitude of the larger uncertainty is taken as the total symmetrised uncertainty.

9 Results

The measurement of the W boson helicity fractions in the semileptonic top quark pair events obtained via template fit method as described in Section 7.1. The full 2012 dataset recorded by the ATLAS detector at a centre-of-mass energy of $\sqrt{s} = 8$ TeV, with an integrated luminosity corresponding to 20.2 fb^{-1} is analysed. The W boson helicity fractions are accessed via the angular distributions of polarisation analysers defined in Section 2.2.5 for leptonic and hadronic W boson decays.

Studying both leptonic and hadronic analysers with 1 b-tag and $\geq$ 2 b-tags in the electron and muon channels, gives several options to perform combined fit results, which are discussed in more details in Section 9.1. In order to achieve the goal of this research as discussed in Section 2.2.3, the obtained results are interpreted in terms of limits set on the Wtb vertex anomalous couplings, where the details are given in Section 9.2.

9.1. Combination of Helicity Fraction Measurements

In order to obtain the most precise measurement of the W boson helicity fractions, different channel combinations are studied. From the statistical error point of view, combining more channels leads to an increase of sensitivity (see Table 8.1). For instance, a simultaneous fit with both 1 b-tag and $\geq$ 2 b-tags gives smaller statistical error with respect to a fit with $\geq$ 2 b-tags. It is also true for combining templates from both analysers. Therefore, the eight-channel combination, which is composed of leptonic and hadronic templates with 1 b-tag and $\geq$ 2 b-tags in electron and muon channels led to the smallest statistical error compared to the other combinations.

However, due to the high rate of $t\bar{t}$ production at the LHC, the uncertainty in measuring

the W boson helicity fractions is driven by the systematic errors. Therefore, the impact of different combination options on the systematic uncertainties are studied.

Combination of different b-tag regions

Simultaneous fits using events with 1 b-tag and $\geq$ 2 b-tags are studied using each of leptonic and hadronic analysers. The inclusion of 1 b-tag region in the fit using the leptonic analyser does not improve the sensitivity due to larger systematic uncertainties in this region, which has less signal purity compared to the $\geq$ 2 b-tags regions (see Table 6.1 for signal and background yields comparison in different b-tag regions.).

In contrast, as seen in Figure 7.3, the hadronic analyser suffers from low separation power between the left- and right-handed templates in both b-tag regions, due to mis-assignment of the light jets, originating from the W boson decay, to the up/down-type quarks in event reconstruction[1](see Section 6.2.2 for details). The evaluation of the systematic errors in measuring the helicity fractions via the hadronic analyser shows that the hadronic channel sensitivity is improved by the inclusion of the 1 b-tag region. A full comparison between the systematic errors evaluated with and without the inclusion of 1 b-tag region in the fit is presented in Appendix A. The largest impact of the 1 b-tag inclusion is driven by the JES uncertainties which are smaller compared to the fit using only $\geq$ 2 b-tags.

Combination of leptonic and hadronic analysers

The hadronic branch of the semileptonic $t\bar{t}$ decays deals with two extra light jets originating from the W boson hadronic decay. Thus, the impact of the jet related sources of systematic uncertainties, e.g. JER, JES, etc., on the hadronic channel is expected to be larger compared to the leptonic channel, which deals with one b-jet originating from the top quark decay. However, the combination of leptonic and hadronic analysers has been tested and, despite the improvement in the statistical uncertainty as mentioned earlier, it does not improve the total uncertainty.

Tables 8.5 – 8.7 present the comparison between the considered systematic uncertainties in the measurement of the W boson helicity fractions using the best combinations with the leptonic and hadronic analysers. A comparison is also made for the combination of the two analysers in an eight-channel configuration.

[1]Swapping the up/down-type quarks leads to measure the $(\pi - \theta^*)$ angle in the W boson rest frame, which as a result, swaps the left- and right-handed helicity states.

Figure 9.1 presents the post-fit $\cos\theta^*$ distribution obtained using the leptonic analyser with ≥ 2 b-tags, and Figure 9.2 shows the corresponding distribution obtained via the hadronic analyser with 1 b-tag and ≥ 2 b-tags. The uncertainty band in the data-to-best-fit ratio represents the total systematic and statistical uncertainties in the fit result. The peak at $\cos\theta^* \approx$ -0.7 in the 1 b-tag channels in Figure 9.2 is caused by misreconstructed events. A missing second b-tag jet increases the probability of swapping the b-quark jet from the top quark decay with the up-type quark jet from the W boson decay, which affects the $\cos\theta^*$ distribution by measuring the wrong angle.

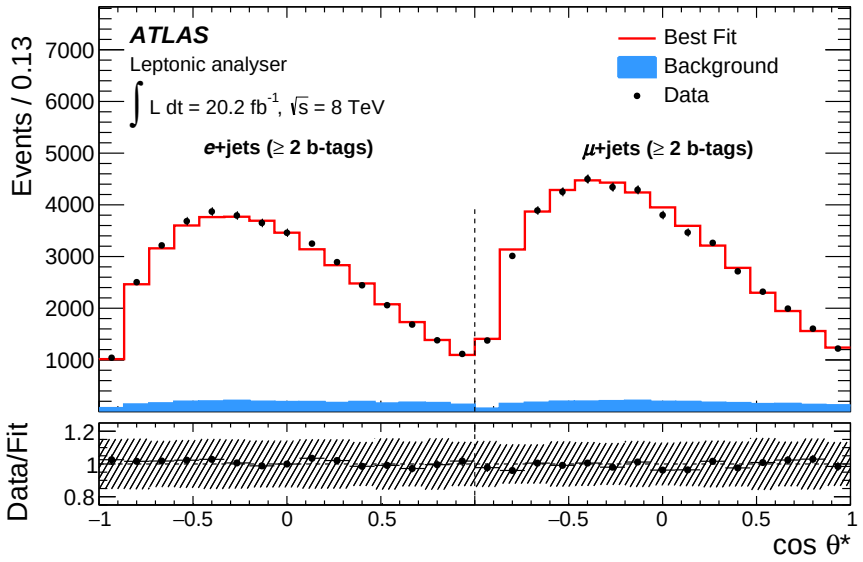

Figure 9.1.: Post-fit distribution of $\cos\theta^*$ for the leptonic analyser with ≥ 2 b-tags, in which a two-channel combination is performed (electron and muon). The uncertainty band represents the total systematic and statistical uncertainties in the fit result [154].

The measured W boson helicity fractions obtained via the leptonic branch of the semileptonic $t\bar{t}$ events with ≥ 2 b-tags are presented in Table 9.1. By definition, the individual fractions sum up to one. The F_0 value is anti-correlated with both F_L and F_R ($\rho_{F_0,F_L} =$ -0.55, $\rho_{F_0,F_R} =$ -0.75), while F_L and F_R are positively correlated ($\rho_{F_L,F_R} =$ +0.16). The quoted values correspond to the total correlation, considering both statistical and systematic uncertainties. Details of the calculation of the total correlation coefficient are given in Appendix B.

Table 9.2 shows the corresponding measurements obtained via the hadronic analyser with 1 b-tag and ≥ 2 b-tags.

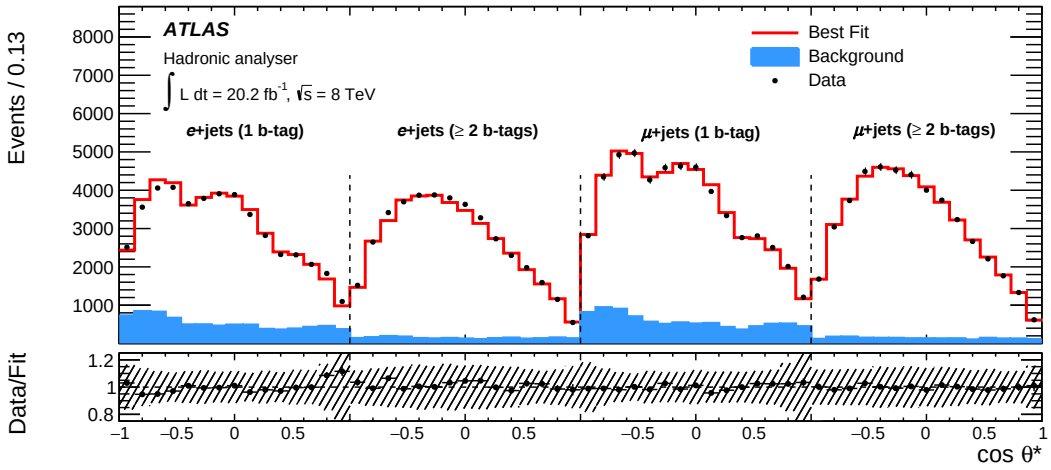

Figure 9.2.: Post-fit distribution of $\cos\theta^*$ for the hadronic analyser, in which the combination of four channels is performed (electron and muon, with exactly 1 b-tag and ≥ 2 b-tags). The uncertainty band represents the total systematic and statistical uncertainties in the fit result [154].

Leptonic analyser (≥ 2 b-tags)
$F_0 = 0.709 \pm 0.012$ (stat.+bkg) $^{+0.015}_{-0.014}$ (syst.)
$F_L = 0.299 \pm 0.008$ (stat.+bkg) $^{+0.013}_{-0.012}$ (syst.)
$F_R = -0.008 \pm 0.006$ (stat.+bkg) ± 0.012 (syst.)

Table 9.1.: Measured W boson helicity fractions obtained from the combination of e+jets and μ+jets channels with ≥ 2 b-tags using the leptonic analyser, including the statistical and background normalisation uncertainties from the fit and the full systematic uncertainties.

Hadronic analyser (1 b-tag + ≥ 2 b-tags)
$F_0 = 0.659 \pm 0.010$ (stat.+bkg) $^{+0.052}_{-0.054}$ (syst.)
$F_L = 0.281 \pm 0.021$ (stat.+bkg) $^{+0.063}_{-0.067}$ (syst.)
$F_R = 0.061 \pm 0.022$ (stat.+bkg) $^{+0.101}_{-0.108}$ (syst.)

Table 9.2.: Measured W boson helicity fractions obtained from the combination of e+jets and μ+jets channels with 1 b-tag + ≥ 2 b-tags using the hadronic analyser, including the statistical and background normalisation uncertainties from the fit and the full systematic uncertainties.

The results obtained with the two analysers agree well within the uncertainties.

9.2. Constraints on Wtb Vertex

The results of the measurement of the W boson polarisation obtained from the leptonic analyser with ≥ 2 b-tags are interpreted in terms of limits set on the anomalous couplings of the top quark decay vertex.

As discussed in Section 2.2.3, the Wtb vertex is parametrised in terms of an effective Lagrangian [58, 172, 173]. The effect of non-vanishing V_{R}, g_{L}, and g_{R} on the helicity fractions has been calculated in [65, 174]. As an example, Figure 9.3 shows the influence on left-handed polarisation, F_L. The dependence of the helicity fractions on the anomalous couplings are implemented in the `EFTfitter` tool [175], which is used in this analysis to extract those limits. For simplicity, all couplings are assumed to be real[2].

The `EFTfitter` makes use of the measured values of the longitudinal and left-handed fractions. The right-handed fraction is considered via the constraint of $\sum F_i = 1$. The tool also needs the total uncertainties of the input helicity fractions and the correlation between those uncertainties. Appendix B details the total covariance matrix calculation which is used to obtain the required correlation between the total systematic uncertainties.

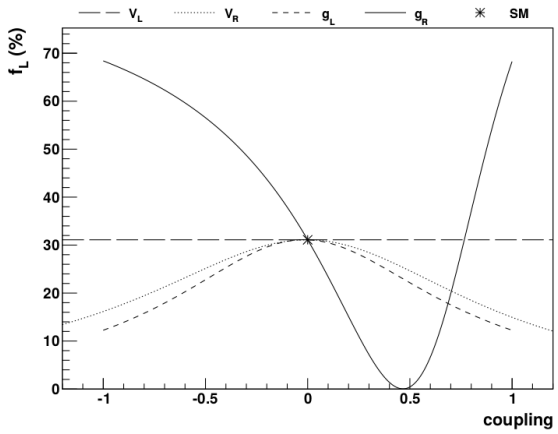

Figure 9.3.: Effect of modified anomalous couplings V_{R}, g_{L}, and g_{R} on the fraction of longitudinally polarised W bosons as implemented in the `EFTfitter` tool.

Results showing the 68% and 95.5% posterior integrals for g_{L} and g_{R} (while fixing

[2]This condition corresponds to the CP-conserving case. Complex values would imply that the top quark decay has a CP-violating component [57].

$V_L = 1$, $V_R = 0$) can be found in Figure 9.4, as well as the corresponding posterior integrals for g_R and V_R, while fixing the other parameters to their SM values.

In Figure 9.5, the one-dimensional limits for each anomalous coupling are shown (for all other couplings fixed to their SM expectation). The 95.5% CL intervals for the anomalous couplings are also summarised in Table 9.3.

Coupling	95 % CL limit
V_R	$[-0.24, 0.31]$
g_L	$[-0.14, 0.11]$
g_R	$[-0.02, 0.06]$, $[0.74, 0.78]$

Table 9.3.: Limits for the anomalous couplings V_R, g_L, and g_R at 95.5 % CL. The limits were derived using the measured W boson helicity fractions (combination of electron+muon channels using the leptonic analyser with ≥ 2 b-tags).

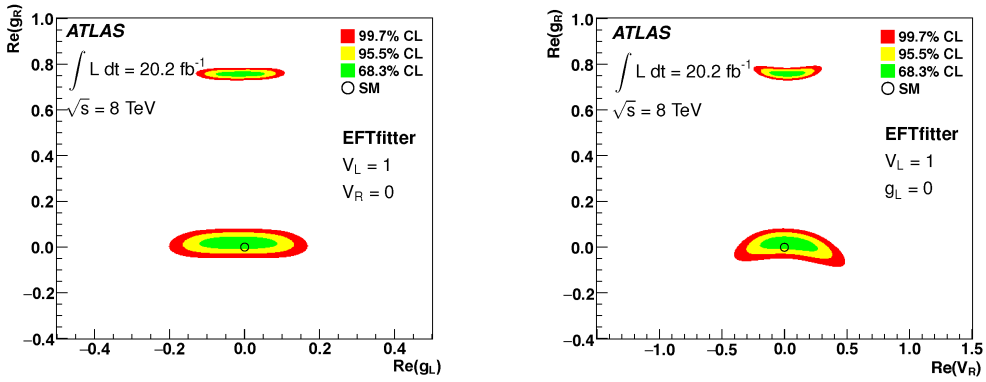

(a) (b)

Figure 9.4.: (a): Allowed regions at 68%, 95.5% and 99.7 % confidence level (CL) for the Wtb anomalous couplings g_L and g_R. The other couplings are fixed to their SM expectation ($V_L = 1$, $V_R = 0$), and (b): Corresponding limits on V_R and g_R for the other couplings fixed to their SM expectation. The limits are obtained using the combined electron and muon channels of the leptonic analyser with ≥ 2 b-tags [154].

Similar limits derived in previous measurements by ATLAS and CMS at the LHC and by CDF and DØ at Tevatron are listed in Table 2.2. Complementary limits can be set by other measurements: the allowed region of $g_R \approx 0.75$ is excluded by measurements of the t-channel single top quark production [175–178], which also constrains V_L. The top

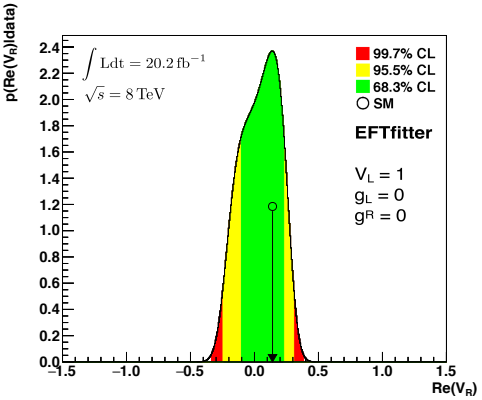

(a)

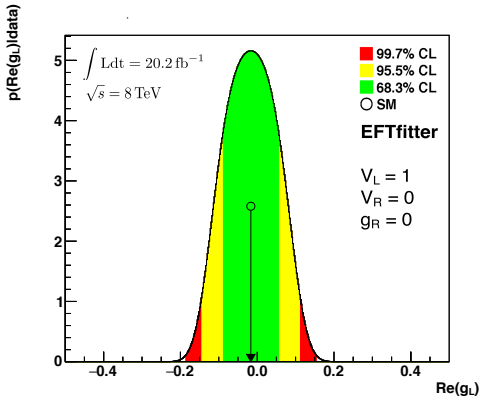

(b)

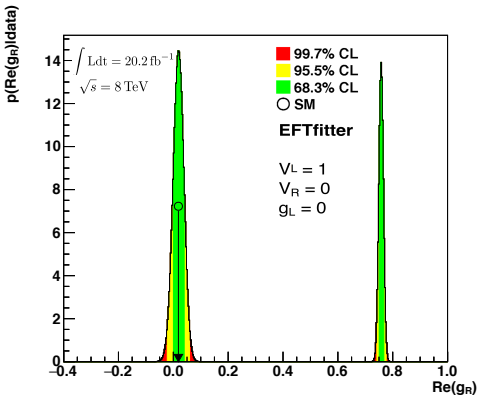

(c)

Figure 9.5.: Limits on (a): V_{R}, (b) g_{L} and (c): g_{R}, while fixing the other anomalous couplings to their SM values. The limits are obtained using the combined electron and muon channels of the leptonic analyser with ≥ 2 b-tags.

quark decay vertex is also probed via the measurement of weak radiative B-meson decay branching ratio, $\bar{B} \to X_s\gamma$, which provides stringent bounds on V_{R} and g_{R} [179].

10

Summary, Conclusion and Outlook

In this thesis, the polarisation of the W boson in semileptonic $t\bar{t}$ decays is studied. The full 2012 dataset corresponding to an integrated luminosity of 20.2 fb^{-1} collected at a centre-of-mass energy of $\sqrt{s} = 8$ TeV with the ATLAS detector is analysed to measure the W boson helicity fractions.

The angular distribution of the charged lepton (down-type quark) with respect to the reversed b-quark momentum direction in the leptonically (hadronically) decaying W boson rest frame is sensitive to the W boson polarisation, and utilised as a polarisation analyser to measure the longitudinal, left- and right-handed W boson helicity fractions. This analysis represents the first measurement of the helicity fractions using a dedicated up- and down-type quark separation for the hadronic analyser.

The $t\bar{t}$ event selection requires at least one primary collision vertex, exactly one reconstructed electron or muon with $p_{\mathrm{T}} > 25$ GeV and at least four jets, of which at least one is b-tagged. The selected events are split into two orthogonal b-tag regions: 1) with exactly one b-tag, and 2) with at least two b-tags. Hence, taking the lepton flavour types into account, the data is split into four orthogonal channels. In order to suppress multijet background in events with one b-tag, $E_{\mathrm{T}}^{\mathrm{miss}}$ is required to be larger than 20 GeV and the sum of $E_{\mathrm{T}}^{\mathrm{miss}}$ and the transverse mass of the leptonically decaying W boson, $m_T(W)$, is required to be larger than 60 GeV.

To reconstruct the polarisation analysers, the $t\bar{t}$ events are fully reconstructed using a kinematic likelihood fit. An extension to the kinematic likelihood fit is utilised to differentiate the up- and down-type jets of the hadronically decaying W boson. A p_{T} dependent b-jet tagging algorithm weights distribution obtained for different jet flavours is used to discriminate between up- and down-type jets.

The shape of data and simulated distributions of the analysers are compared via a binned likelihood template fit approach, in order to measure the helicity fractions. Dedicated $t\bar{t}$ signal templates for pure longitudinal, left- and right-handed helicity states are produced by reweighting the SM Monte Carlo $t\bar{t}$ events at truth level. To account for the background processes, three templates for W+jets background separated with respect to its heavy flavour component, one template for misidentified leptons, and one template for the remaining background contributions (single top, Z+jets and diboson) are considered. The normalisation of the background processes are used to constrain the fit, while the normalisation of each signal template is considered as a free parameter.

The results obtained from the combined electron and muon channels of the leptonic analyser with ≥ 2 b-tags are found to be $F_0 = 0.709 \pm 0.012$ (stat.+bkg. norm.) ± 0.015 (syst.), $F_L = 0.299 \pm 0.008$ (stat.+bkg. norm.) ± 0.013 (syst.) and $F_R = -0.008 \pm 0.006$ (stat.+bkg.) ± 0.012 (syst). These results present the most sensitive determination of the W boson helicity fractions using semileptonic $t\bar{t}$ decays to date, and are in good agreement with the NNLO prediction of the Standard Model within the uncertainties. Figure 10.1 presents the summary of the W boson helicity fraction measurements from ATLAS and CMS compared to the theory predictions.

The limits set via the presented measurement on the anomalous couplings of the Wtb vertex improved the limits set via previous ATLAS and CMS measurements, and good agreement with the Standard Model is observed.

10.1. Outlook

The future measurements of the W boson polarisation in higher energies at the hadron colliders could benefit from the following proposals.

10.1.1. Combining the results with the measurements from Dileptonic $t\bar{t}$ events

The dileptonic $t\bar{t}$ channel is known as the most pure top quark decay channel. Although it has low statistics, but it has the lowest jet multiplicity in the final state signature. Therefore, the jet related systematic uncertainty sources are expected to have the lowest impact in the measurement of the W boson polarisation in this channel. Furthermore, this channel benefits from having two leptonic analysers which is more sensitive than the hadronic analyser as seen in this analysis.

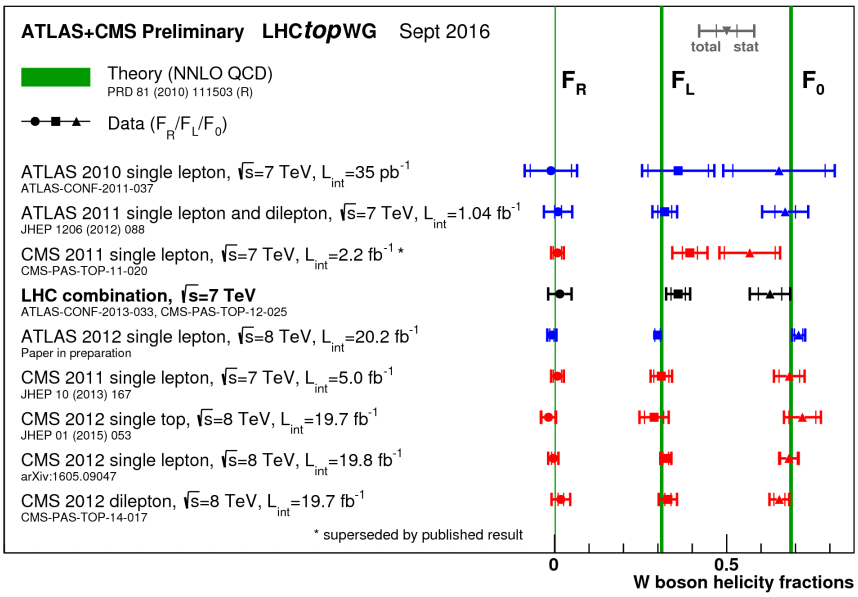

Figure 10.1.: Summary of the W boson helicity fraction measurements from ATLAS and CMS compared to the theory predictions. The uncertainty on the theory predictions is shown by the width of the green band [180]. The entry of ATLAS 2012 single lepton, $\sqrt{s} = 8$ TeV, belongs to the results obtained from this thesis.

On the other hand, the measurement of the W boson polarisation in the dileptonic channel is orthogonal to the corresponding measurement in the lepton+jets channel, i.e. they use statistically independent events. Therefore, results with higher sensitivity are expected by combining the results of the two measurements.

10.1.2. Usage of Jet Charge to Improve the Up/Down-type Quark Separation

In order to make use of the hadronic analyser in the measurement of the W boson polarisation, the separation between the up- and down-type quarks is essential. As explained in Section 6.2.2, a p_{T} dependent MV1 weights distribution obtained for different jet flavours is used to discriminate between up- and down-type jets.

Another discriminant that could serve the mentioned separation is the use of *jet charge*. Given the conservation of charge in the hadronisation process, the charge of the originating parton could be identified by the identification of the charge of the hadrons to which a jet is fragmented [181, 182]. Similar methods are used to measure the charge of the top quark by both ATLAS and CMS [183, 184] to exclude the BSM processes with exotic top quark charge of $-4/3$.

However, the light jets originating from the hadronic W boson decay have same sign charges, some discriminating variables such as the tracks with maximum p_{T} and weighted jet charge proposed in [85], could be defined and utilised in a multi-variate technique to construct a final discriminant variable, which potentially can improve the current up- and down-type quark discriminant. In former method the charge of the track within the jet that has the highest p_{T} is used to assign the jet charge, while in the latter method a weighted charge using all tracks are used according to their momentum contribution.

10.1.3. Usage of Up-type Quark in the Hadronic Analyser

As discussed in Section 3.2.3, the jets with higher transverse momentum have higher energy resolution, and therefore, have lower uncertainty in measuring their energy. Due to the $V-A$ structure of the Wtb vertex as discussed in Section 2.2.3, the up-type quark originating from the W boson hadronic decay is preferably propagated in the direction of the W boson. Thus, on average the up-type quark acquires a higher transverse momentum with respect to the down-type quark, and consequently it has on average a higher reconstruction efficiency compared to the down-type quark.

On the other hand, the hadronic analyser is defined as the angle between the down-type

quark and the inverse direction of the b-quark in the W boson rest frame. However, one could use the inverse direction of the up-type quark with higher reconstruction efficiency rather than the direct usage of the down-type quark direction, knowing that the light jets are propagated back-to-back in the W boson rest frame.

Acknowledgements

This thesis would not have been possible without the support and guidance of many people to whom I owe my gratitude. At first, I would like to express my gratitude to my supervisor, Arnulf Quadt, for inviting me to join his research group, for all his kind support and guidances during this journey and for the opportunity that he gave me to understand the priceless joy of research. Thank you for believing in me. It was an honer for me to be a member in this institute and your research group. I would also like to thank Stan Lai for agreeing to be the co-referee of this thesis, and thanks for spreading positive energy to everyone he meets.

There are no words to express how thankful I am to Boris Lemmer. Thank you for a lot of discussions and advice and your continued encouragement and all the positive energy I got from you, and for all your kind help in the hard moments. Lisa Shabalina, thank you for all the support during my stay at CERN, for your patience and kindness. Without your support and encouragement this success wouldnt́ have been possible. You gave me enthusiasm and taught me how to think analytically. I am proud that I worked with you and under your supervision. Thank you for everything you have done for me. Thanks to the tireless and energetic friend, Maria Moreno Llacer, for her kind support during my stay at CERN. Thanks to Jörn Grosse-Knetter, for supervising my first project in particle physics hardware with ATLAS during my Pixel detector Qualification task, for his patience and support. I would like to take the opportunity to express my sincere appreciation to all my friends and colleagues at the II. Institute of Physics with whom I shared nice moments along the way. Thank you for all the support, insights, and help you have provided me over the past 4 years. Especially I want to thank Ms. Hamdi, Ms.

Tyson, Ms. Lange and Ms. Afshar.

My special feelings and thanks to my dear wife, Nibras, who has been with me all these years and has made them the best years of my life. Her support, encouragement, patience and unwavering love were undeniably the bedrock upon which this success have been built. Thanks to my little daughter Fatema, for coming to my life. You are the best daughter I could ever have. Thanks for your smiles that encouraged me to efficiently overcome the difficulties encountered in my pursuit of the Ph.D. degree.

My final words go to my bleeding homeland. I am greatly honoured to have received the Ph.D. scholarship from the Iraqi ministry of higher education and scientific research (MOHESR). Thanks for supporting me during all these years despite the pain and suffering of the war.

Appendices

A

Systematic Uncertainties - Full Tables

This appendix presents the tables of significant systematic uncertainties in the measurement of W boson helicity fractions. The systematic uncertainties are evaluated via the ensemble test method using 5000 sets of pseudo-data. The results here quoted for the leptonic analyser with ≥ 2 b-tags, hadronic analyser with ≥ 2 b-tags, and the hadronic analyser with 1 b-tag + ≥ 2 b-tags. The algorithm discussed in Section 8.2.6 is used to determine which systematics are considered significant. The uncertainties are split according detector and modelling systematics, and three tables are provided (one for each helicity fraction).

Table A.1.: Change in the mean value of fitted helicity fraction, F_0, due to systematic variations up and down. The fits are performed using 5000 sets of pseudo-data and correspond to the leptonic analyser with ≥ 2 b-tags, hadronic analyser with ≥ 2 b-tags, and the leptonic+hadronic analysers with 1 b-tag + ≥ 2 b-tags.

		F_0		
Systematic uncertainty	Up/Down	Leptonic 2incl	Had 2incl	Had 1excl+2incl
Modeling				
Radiation	radHi	-0.0025	-0.0382	-0.0108
	radLo	0.0033	0.048	0.0178
Reconstructed Objects				
BTAG_bTagVar_0	up	-0.0001	-0.0007	-0.0012
	down	0.0	-0.0	0.0001
BTAG_bTagVar_1	up	-0.001	-0.0021	0.0014
	down	0.0008	0.0012	-0.0026
BTAG_bTagVar_2	up	0.0001	-0.0002	-0.0069
	down	-0.0004	-0.0006	0.0059
BTAG_bTagVar_3	up	0.0005	0.0008	0.0081
	down	-0.0011	-0.0014	-0.0093
BTAG_bTagVar_4	up	0.0005	0.0003	-0.0005
	down	-0.0008	-0.0008	-0.0006
BTAG_bTagVar_5	up	-0.0001	-0.0002	0.0246
	down	0.0004	-0.0006	-0.0262
BTAG_cTagVar_0	up	-0.0005	-0.0006	-0.0009
	down	-0.0003	-0.0002	-0.0003
BTAG_cTagVar_1	up	0.0005	0.0014	0.004
	down	-0.0004	-0.0021	-0.0051
BTAG_cTagVar_2	up	0.0001	-0.0007	-0.0022
	down	0.0001	0.0002	0.0011
BTAG_cTagVar_3	up	0.0006	0.0033	0.0076
	down	-0.0006	-0.004	-0.0084
BTAG_misTagVar_0	up	-0.0002	-0.0006	-0.0007
	down	-0.0003	-0.0003	-0.0003
BTAG_misTagVar_1	up	-0.0003	-0.0005	-0.0003
	down	-0.0	-0.001	-0.0011
BTAG_misTagVar_10	up	-0.0002	-0.0007	-0.0016
	down	0.0001	0.0009	0.0015
BTAG_misTagVar_11	up	-0.0005	-0.0021	-0.0053
	down	0.0008	0.0021	0.0047
BTAG_misTagVar_2	up	0.0002	-0.0008	-0.0009
	down	0.0001	-0.0007	-0.0012
BTAG_misTagVar_3	up	-0.0	-0.0004	-0.0005
	down	-0.0003	-0.0006	-0.0007
BTAG_misTagVar_4	up	-0.0001	-0.0003	-0.0008
	down	-0.0001	-0.0003	-0.0001

		F_0		
Systematic uncertainty	Up/Down	Leptonic 2incl	Had 2incl	Had 1excl+2incl
BTAG_misTagVar_5	up	-0.0	-0.0003	-0.0007
	down	-0.0001	-0.0006	-0.0004
BTAG_misTagVar_6	up	-0.0001	0.0	0.0003
	down	-0.0002	-0.0	-0.0008
BTAG_misTagVar_7	up	-0.0	0.0002	-0.0003
	down	-0.0003	0.0002	-0.0002
BTAG_misTagVar_8	up	0.0001	-0.0001	0.0001
	down	-0.0002	-0.0002	-0.0006
BTAG_misTagVar_9	up	0.0	0.0008	0.001
	down	0.0001	-0.0008	-0.0013
ELE_ID	up	-0.0028	-0.0027	-0.0023
	down	0.003	0.0027	0.0021
ELE_RECO	up	-0.0003	-0.0003	-0.0007
	down	0.0002	-0.0	-0.0001
ELE_TRIGGER	up	-0.0003	-0.0007	-0.0008
	down	0.0	0.0008	0.0004
MUON_ID	up	0.0006	0.0008	0.001
	down	-0.0009	-0.0014	-0.0014
MUON_RECO	up	0.0	-0.0001	-0.0002
	down	-0.0003	-0.0013	-0.0009
MUON_TRIGGER	up	0.0024	0.0031	0.0024
	down	-0.0028	-0.0039	-0.0034
jer_DataMC_Difference		-0.0021	-0.0096	-0.0096
jer_NP0	up	0.0013	-0.0003	-0.0043
	down	-0.0021	-0.0096	-0.0096
jer_NP1	up	-0.0021	-0.0096	-0.0101
	down	-0.0019	-0.0069	-0.0088
jer_NP2	up	-0.0013	-0.0043	-0.0069
	down	-0.0018	-0.0101	-0.0104
jer_NP3	up	-0.0025	-0.0088	-0.0096
	down	-0.0004	-0.0056	-0.0077
jer_NP4	up	-0.0013	-0.0094	-0.0098
	down	-0.0024	-0.008	-0.0101
jer_NP5	up	-0.002	-0.0095	-0.0117
	down	-0.0018	-0.0063	-0.0084
jer_NP6	up	-0.0025	-0.008	-0.0094
	down	-0.0006	-0.0086	-0.0088
jer_NP7	up	-0.0028	-0.0089	-0.0086
	down	-0.0013	-0.0076	-0.0091
jer_NP8	up	-0.0021	-0.0096	-0.0097
	down	-0.0018	-0.0084	-0.0092
jer_Noise_ForwardRegion		-0.002	-0.0101	-0.0104

F_0				
Systematic uncertainty	Up/Down	Leptonic 2incl	Had 2incl	Had 1excl+2incl
jes_EtaIntercalibration_TotalStat	up	-0.0007	0.0031	0.0013
	down	-0.0007	-0.0035	-0.0026
jes_FlavourComp	up	-0.0042	0.0096	0.0054
	down	0.0018	-0.0077	-0.003
jes_FlavourResponse	up	-0.0024	-0.0003	0.0038
	down	-0.0005	-0.0003	-0.0056
jes_Modelling1	up	-0.003	0.0046	-0.0005
	down	0.0014	-0.0041	0.0016
jes_RhoTopology	up	-0.0021	0.0047	0.0014
	down	0.0022	-0.0045	-0.0003
jes_Statistical1	up	-0.0015	0.0023	-0.0002
	down	0.0006	-0.0011	-0.0003
jvf	up	-0.0036	-0.0152	-0.0129
	down	-0.0017	0.0105	0.0092
Total Syst.		+0.0149	+0.067	+0.0518
		-0.0136	-0.0673	-0.0541

Table A.2.: Change in the mean value of fitted helicity fraction, F_L, due to systematic variations up and down. The fits are performed using 5000 sets of pseudo-data and correspond to the leptonic analyser with $\geq$2 b-tags, hadronic analyser with $\geq$2 b-tags, and the leptonic+hadronic analysers with 1 b-tag + $\geq$2 b-tags.

		F_L		
Systematic uncertainty	Up/Down	Leptonic 2incl	Had 2incl	Had 1excl+2incl
Modeling				
Radiation	radHi	0.0058	-0.0089	-0.0115
	radLo	-0.0032	0.0376	0.0393
Reconstructed Objects				
BTAG_bTagVar_0	up	0.0001	-0.001	-0.0003
	down	-0.0002	0.0007	0.0007
BTAG_bTagVar_1	up	0.0007	-0.0014	-0.0019
	down	-0.0007	0.0001	0.0019
BTAG_bTagVar_2	up	-0.0003	0.0022	0.0021
	down	0.0004	-0.0026	-0.0023
BTAG_bTagVar_3	up	-0.0006	-0.0013	-0.0007
	down	0.0007	0.0013	0.0007
BTAG_bTagVar_4	up	-0.0006	-0.0008	0.0
	down	0.0006	0.0006	0.0005
BTAG_bTagVar_5	up	-0.0002	0.0009	-0.0013
	down	-0.0002	-0.0012	0.0022
BTAG_cTagVar_0	up	0.0003	0.0025	0.002
	down	-0.0	-0.003	-0.0021
BTAG_cTagVar_1	up	-0.0002	0.0024	0.0014
	down	0.0	-0.0025	-0.0013
BTAG_cTagVar_2	up	0.0	0.0018	0.0025
	down	-0.0	-0.0023	-0.0012
BTAG_cTagVar_3	up	-0.0001	0.0084	0.0078
	down	0.0001	-0.0089	-0.0075
BTAG_misTagVar_0	up	0.0001	-0.0008	-0.0
	down	0.0	-0.0006	-0.0004
BTAG_misTagVar_1	up	0.0001	-0.0003	0.0005
	down	-0.0001	-0.0003	0.0001
BTAG_misTagVar_10	up	0.0001	-0.0033	-0.0033
	down	0.0001	0.0035	0.0039
BTAG_misTagVar_11	up	-0.0001	-0.0098	-0.0086
	down	-0.0002	0.0103	0.0103
BTAG_misTagVar_2	up	-0.0	0.0005	0.0
	down	-0.0001	-0.0001	0.0001
BTAG_misTagVar_3	up	0.0	-0.0007	-0.0004
	down	0.0002	-0.0	0.0001
BTAG_misTagVar_4	up	0.0	0.0003	0.0004
	down	-0.0	-0.0004	-0.0006

		F_L		
Systematic uncertainty	Up/Down	Leptonic 2incl	Had 2incl	Had 1excl+2incl
BTAG_misTagVar_5	up	-0.0001	-0.0008	-0.0012
	down	0.0	0.0003	0.0008
BTAG_misTagVar_6	up	0.0001	0.0002	0.0009
	down	0.0002	0.0004	0.0004
BTAG_misTagVar_7	up	-0.0	-0.0001	0.0002
	down	0.0001	0.0007	0.0004
BTAG_misTagVar_8	up	-0.0001	0.0024	0.0019
	down	0.0001	-0.0013	-0.0013
BTAG_misTagVar_9	up	0.0001	-0.0005	0.0002
	down	-0.0001	0.0004	0.001
ELE_ID	up	0.0018	-0.0021	-0.0028
	down	-0.002	0.0026	0.0034
ELE_RECO	up	0.0002	-0.0005	0.0005
	down	-0.0003	0.0009	0.0003
ELE_TRIGGER	up	0.0	-0.0009	-0.0002
	down	0.0002	0.0003	0.0015
MUON_ID	up	-0.0002	0.0016	0.0014
	down	0.0003	-0.0014	-0.0014
MUON_RECO	up	-0.0001	0.0007	0.0005
	down	0.0	-0.0005	-0.0006
MUON_TRIGGER	up	-0.0012	0.0031	0.0044
	down	0.0015	-0.0035	-0.0031
jer_DataMC_Difference		0.0002	-0.0125	-0.0114
jer_NP0	up	-0.0044	-0.002	0.0026
	down	0.0002	-0.0125	-0.0114
jer_NP1	up	0.0002	-0.012	-0.0122
	down	-0.0003	-0.0138	-0.0099
jer_NP2	up	-0.0016	-0.0002	0.0071
	down	0.0	-0.0141	-0.0125
jer_NP3	up	0.0001	-0.0152	-0.0145
	down	-0.0012	-0.0076	-0.0014
jer_NP4	up	-0.0001	-0.0139	-0.0141
	down	-0.0006	-0.0164	-0.0143
jer_NP5	up	-0.0004	-0.0078	-0.0048
	down	-0.0003	-0.013	-0.0125
jer_NP6	up	0.0004	-0.013	-0.013
	down	-0.0009	-0.014	-0.0131
jer_NP7	up	-0.0	-0.0125	-0.012
	down	-0.0005	-0.0143	-0.0133
jer_NP8	up	0.0002	-0.0125	-0.0114
	down	-0.0001	-0.0153	-0.0156
jer_Noise_ForwardRegion		0.0003	-0.0136	-0.0137

F_L				
Systematic uncertainty	Up/Down	Leptonic 2incl	Had 2incl	Had 1excl+2incl
jes_EtaIntercalibration_TotalStat	up	0.0001	-0.0022	-0.0022
	down	0.0002	-0.0012	-0.0002
jes_FlavourComp	up	0.0017	-0.0	0.0034
	down	-0.0013	0.0059	0.0029
jes_FlavourResponse	up	0.0013	0.004	-0.0031
	down	-0.0002	0.004	0.0055
jes_Modelling1	up	0.0013	0.0054	0.0103
	down	-0.0008	0.0013	-0.0025
jes_RhoTopology	up	0.0009	0.0012	0.0027
	down	-0.0018	0.0012	-0.0014
jes_Statistical1	up	0.0008	-0.0	0.0015
	down	-0.0008	-0.0032	-0.0036
jvf	up	0.0019	0.0041	0.0012
	down	0.0013	-0.0062	-0.0046
Total Syst.		+0.0129	+0.0596	+0.0625
		-0.012	-0.0672	-0.0667

Table A.3.: Change in the mean value of fitted helicity fraction, F_R, due to systematic variations up and down. The fits are performed using 5000 sets of pseudo-data and correspond to the leptonic analyser with $\geq$2 b-tags, hadronic analyser with $\geq$2 b-tags, and the leptonic+hadronic analysers with 1 b-tag + $\geq$2 b-tags.

		F_R		
Systematic uncertainty	Up/Down	Leptonic 2incl	Had 2incl	Had 1excl+2incl
Modeling				
Radiation	radHi	-0.0034	0.047	0.022
	radLo	-0.0001	-0.0855	-0.0573
Reconstructed Objects				
BTAG_bTagVar_0	up	0.0	0.0016	0.0018
	down	0.0001	-0.0009	-0.001
BTAG_bTagVar_1	up	0.0002	0.0034	0.0003
	down	-0.0	-0.0017	0.0011
BTAG_bTagVar_2	up	0.0003	-0.0022	0.0048
	down	0.0001	0.0029	-0.0035
BTAG_bTagVar_3	up	-0.0	0.0003	-0.0076
	down	0.0004	0.0003	0.0084
BTAG_bTagVar_4	up	0.0001	0.0006	0.0003
	down	0.0001	-0.0	0.0001
BTAG_bTagVar_5	up	0.0003	-0.0009	-0.0232
	down	-0.0002	0.0017	0.0238
BTAG_cTagVar_0	up	0.0003	-0.0023	-0.0013
	down	0.0002	0.0028	0.0024
BTAG_cTagVar_1	up	-0.0003	-0.0043	-0.0056
	down	0.0004	0.0044	0.0062
BTAG_cTagVar_2	up	0.0001	-0.0014	-0.0001
	down	0.0001	0.0018	0.0003
BTAG_cTagVar_3	up	-0.0005	-0.0119	-0.0156
	down	0.0007	0.0126	0.0162
BTAG_misTagVar_0	up	0.0002	0.0012	0.0005
	down	0.0001	0.0007	0.0007
BTAG_misTagVar_1	up	0.0002	0.0006	-0.0
	down	0.0002	0.0009	0.0009
BTAG_misTagVar_10	up	0.0002	0.0038	0.005
	down	-0.0	-0.0046	-0.0053
BTAG_misTagVar_11	up	0.0006	0.0116	0.014
	down	-0.0006	-0.0126	-0.0149
BTAG_misTagVar_2	up	0.0	0.0001	0.0006
	down	0.0001	0.0004	0.0011
BTAG_misTagVar_3	up	0.0001	0.0006	0.0008
	down	0.0003	0.0004	0.0005
BTAG_misTagVar_4	up	0.0001	-0.0003	0.0005
	down	0.0001	0.0006	0.0007

F_R				
Systematic uncertainty	Up/Down	Leptonic 2incl	Had 2incl	Had 1excl+2incl
BTAG_misTagVar_5	up	0.0001	0.0009	0.0018
	down	0.0001	0.0001	-0.0003
BTAG_misTagVar_6	up	0.0001	-0.0003	-0.0009
	down	0.0002	-0.0004	0.0003
BTAG_misTagVar_7	up	0.0001	-0.0002	0.0
	down	0.0001	-0.001	0.0001
BTAG_misTagVar_8	up	-0.0	-0.0025	-0.0022
	down	0.0002	0.0015	0.0018
BTAG_misTagVar_9	up	-0.0001	-0.0005	-0.0011
	down	0.0001	0.0002	0.0004
ELE_ID	up	0.001	0.0042	0.005
	down	-0.0011	-0.005	-0.0054
ELE_RECO	up	0.0001	0.0006	0.0
	down	-0.0	-0.0007	-0.0003
ELE_TRIGGER	up	0.0003	0.0013	0.001
	down	-0.0002	-0.0012	-0.0019
MUON_ID	up	-0.0002	-0.0025	-0.0024
	down	0.0005	0.0028	0.0026
MUON_RECO	up	-0.0	-0.0007	-0.0005
	down	0.0002	0.0016	0.0016
MUON_TRIGGER	up	-0.001	-0.0062	-0.0068
	down	0.0013	0.007	0.0066
jer_DataMC_Difference		0.0019	0.0219	0.021
jer_NP0	up	0.0031	0.0021	0.0018
	down	0.0019	0.0219	0.021
jer_NP1	up	0.0019	0.0212	0.022
	down	0.002	0.0207	0.0187
jer_NP2	up	0.003	0.0042	-0.0001
	down	0.0017	0.0238	0.0225
jer_NP3	up	0.0025	0.0239	0.0242
	down	0.0015	0.0128	0.009
jer_NP4	up	0.0014	0.0231	0.0236
	down	0.0031	0.0242	0.0243
jer_NP5	up	0.0026	0.017	0.0166
	down	0.0023	0.0191	0.0208
jer_NP6	up	0.0021	0.0209	0.0222
	down	0.0016	0.0225	0.0217
jer_NP7	up	0.0028	0.0213	0.0207
	down	0.0017	0.0216	0.0222
jer_NP8	up	0.0019	0.0219	0.0212
	down	0.002	0.0238	0.0248
jer_Noise_ForwardRegion		0.0019	0.0235	0.024

F_R				
Systematic uncertainty	Up/Down	Leptonic 2incl	Had 2incl	Had 1excl+2incl
jes_EtaIntercalibration_TotalStat	up	0.0006	-0.0011	0.0006
	down	0.0006	0.0045	0.0027
jes_FlavourComp	up	0.0026	-0.0098	-0.0089
	down	-0.0003	0.002	-0.0
jes_FlavourResponse	up	0.0011	-0.0039	-0.0007
	down	0.0008	-0.0039	0.0002
jes_Modelling1	up	0.0018	-0.0102	-0.0097
	down	-0.0007	0.0026	0.0013
jes_RhoTopology	up	0.0012	-0.0063	-0.0042
	down	-0.0005	0.0031	0.0019
jes_Statistical1	up	0.0007	-0.0023	-0.0013
	down	0.0	0.0042	0.0041
jvf	up	0.0017	0.011	0.0114
	down	0.0006	-0.0046	-0.0045
Total Syst.		+0.0125	+0.1208	+0.101
		-0.0116	-0.1277	-0.1084

B

Systematics: Covariance Matrix

The covariance matrix for each systematic uncertainty component, k, is defined as:

$$C_{syst,k} = \begin{pmatrix} \sigma^2_{F_0} & cF_0F_L & cF_0F_R \\ cF_0F_L & \sigma^2_{F_L} & cF_LF_R \\ cF_0F_R & cF_LF_R & \sigma^2_{F_R} \end{pmatrix}, \tag{B.1}$$

where σ_{F_i} is the uncertainty in measuring the helicity fraction, F_i, for a given systematic component. Since each systematic is assumed to be correlated across the different helicity fractions, the off-diagonal terms are written as:

$$cF_iF_j = \sigma_{F_i}\sigma_{F_j}. \tag{B.2}$$

The signs of the components σ_{F_i} reflects whether the up/down variation has a positive/negative effect on a given helicity fraction measurement with respect to the nominal measurement. For every systematic uncertainty there should be at least one positive error and at least one negative error, such that the overall normalisation $F_0 + F_L + F_R = 1$ is respected.

Once all component matrices are calculated, the full covariance matrix, C can be constructed as the sum of the statistical covariance matrix (C_{stat}) and the direct sum of all systematic matrices (assuming each systematic uncertainty component is uncorrelated from all others). The final covariance matrix, C, is expressed mathematically as:

$$C = C_{stat} + \sum_k C_{syst,k}. \tag{B.3}$$

For the fully combined measurement, i.e., the eight-channel combination of the electron

and muon channels of leptonic and hadronic analysers with 1 b-tag + $\geq$2 b-tags, the summed systematic matrix obtained as

$$C_{\text{syst}} = \begin{pmatrix} 0.00166 & -0.00050 & -0.00114 \\ -0.00050 & 0.00034 & 0.00021 \\ -0.00114 & 0.00021 & 0.00098 \end{pmatrix}. \tag{B.4}$$

The information for the statistical covariance matrix, C_{stat}, is obtained directly from the fit, and the final covariance matrix, $C_{\text{stat + syst}}$ is found as

$$C_{\text{stat + syst}} = \begin{pmatrix} 0.00175 & -0.00053 & -0.00117 \\ -0.00053 & 0.00035 & 0.00022 \\ -0.00117 & 0.00022 & 0.00098 \end{pmatrix} \tag{B.5}$$

The total covariance matrix is used as input to the `EFTfitter` tool, used to place limits on anomalous couplings of the Wtb vertex. Since the fitter takes the correlation coefficients between the fractions as the input, the covariance matrix, C, is translated into the correlation matrix, S, via introducing the diagonal matrix D as

$$D = \text{sqrt}(\text{diag}(C)) \tag{B.6}$$

Indeed D is the square root of the diagonal matrix obtained from C. From there, S is obtained via

$$S = D^{-1}CD^{-1} \tag{B.7}$$

The correlation coefficients, ρ can then be read from the off-diagonal elements of S. Performing this procedure, the correlation fractions for the eight-channel combination is found as

$$\begin{aligned} \rho(F_0, F_L) &= -0.68 \\ \rho(F_0, F_R) &= -0.89 \\ \rho(F_L, F_R) &= 0.37 \end{aligned} \tag{B.8}$$

The sensitivity of anomalous Wtb limits derived using the eight-channel combination can be compared with the limits derived from any other region given the central values obtained from the template fit and the correlation coefficients obtained from the above procedure.

The corresponding correlation coefficients obtained from the measurement using the leptonic analyser with $\geq$2 b-tags results in

$$\begin{aligned} \rho(F_0, F_L) &= -0.55 \\ \rho(F_0, F_R) &= -0.75 \\ \rho(F_L, F_R) &= 0.16 \end{aligned} \tag{B.9}$$

And finally, the correlation coefficients obtained from the hadronic analyser with 1 b-tag + $\geq$2 b-tags are

$$\begin{aligned} \rho(F_0, F_L) &= 0.56 \\ \rho(F_0, F_R) &= -0.91 \\ \rho(F_L, F_R) &= -0.92 \end{aligned} \tag{B.10}$$

Bibliography

[1] J. J. Thomson. "Cathode rays". *Phil. Mag.* 44 (1897), 293.

[2] ATLAS Collaboration. "Observation of a new particle in the search for the Standard Model Higgs boson with the ATLAS detector at the LHC". *Phys. Lett. B* 716 (2012), 1.

[3] CMS Collaboration. "Observation of a new boson at a mass of 125 GeV with the CMS experiment at the LHC". *Phys. Lett. B* 716 (2012), 30.

[4] ATLAS Collaboration, CDF Collaboration, CMS Collaboration, D0 Collaboration. "First combination of Tevatron and LHC measurements of the top-quark mass" (2014). arXiv: 1403.4427 [hep-ex].

[5] CDF Collaboration, F. Abe, et al. "Observation of top quark production in $\bar{p}p$ collisions". *Phys. Rev. Lett.* 74 (1995), 2626.

[6] D0 Collaboration, S. Abachi, et al. "Search for high mass top quark production in $p\bar{p}$ collisions at $\sqrt{s} = 1.8$ TeV". *Phys. Rev. Lett.* 74 (1995), 2422.

[7] A. Czarnecki et al. "Helicity fractions of W bosons from top quark decays at NNLO in QCD". *Phys. Rev* D81 (2010), 111503.

[8] T. Aaltonen et al. "Combination of CDF and D0 measurements of the W boson helicity in top quark decays". *Phys. Rev.* D85 (2012), 071106.

[9] CDF Collaboration, T. Aaltonen, et al. "Measurement of W-Boson Polarization in Top-quark Decay in $p\bar{p}$ Collisions at $\sqrt{s} = 1.96$ TeV". *Phys. Rev. Lett.* 105 (2010), 042002.

[10] D0 Collaboration, V. M. Abazov, et al. "Measurement of the W boson helicity in top quark decays using 5.4 fb^{-1} of $p\bar{p}$ collision data". *Phys. Rev.* D83 (2011), 032009.

[11] ATLAS Collaboration. "Measurement of the W boson polarization in top quark decays with the ATLAS detector". *JHEP* 06 (2012), 088.

[12] CMS Collaboration. "Measurement of the W boson helicity fractions in the decays of top quark pairs to lepton+jets final states produced in pp collisions at $\sqrt{s}$ = 8 TeV". *Phys. Lett.* B762 (2016), 512.

[13] CDF Collaboration, T. Aaltonen, et al. "Model-independent measurement of the W boson helicity in top quark decays at D0". *Phys. Rev. Lett.* 100 (2008), 062004.

[14] CMS Collaboration. "Measurement of the W-boson helicity in top-quark decays from $t\bar{t}$ production in lepton+jets events in pp collisions at $\sqrt{s} = 7$ TeV". *JHEP* 10 (2013), 167.

[15] D. Griffiths. *Introduction to Elementary Particles*. 2nd. Wiley-VCH, Oct. 2008.

[16] F. Halzen and A. D. Martin. *Quarks and Leptons: An Introductory Course in Modern Particle Physics*. 1st. Wiley, Jan. 1984.

[17] K. A. Olive et al. "Review of Particle Physics". *Chin. Phys.* C38 (2014), 090001.

[18] P. A. M. Dirac. "The quantum theory of the electron". *Proc. Roy. Soc. Lond.* A117 (1928), 610.

[19] C. D. Anderson. "The Positive Electron". *Phys. Rev.* 43 (1933), 491.

[20] S. L. Glashow. "Partial Symmetries of Weak Interactions". *Nucl. Phys.* 22 (1961), 579.

[21] S. Weinberg. "A Model of Leptons". *Phys. Rev. Lett.* 19 (1967), 1264.

[22] A. Salam and J. C. Ward. "Electromagnetic and weak interactions". *Phys. Lett.* 13 (1964), 168.

[23] N. Cabibbo. "Unitary Symmetry and Leptonic Decays". *Phys. Rev. Lett.* 10 (1963). [648(1963)], 531.

[24] M. Kobayashi and T. Maskawa. "CP Violation in the Renormalizable Theory of Weak Interaction". *Prog. Theor. Phys.* 49 (1973), 652.

[25] C. S. Wu et al. "Experimental Test of Parity Conservation in Beta Decay". *Phys. Rev.* 105 (1957), 1413.

[26] R. P. Feynman and M. Gell-Mann. "Theory of Fermi interaction". *Phys. Rev.* 109 (1958), 193.

[27] UA2 Collaboration, M. Banner, et al. "Observation of Single Isolated Electrons of High Transverse Momentum in Events with Missing Transverse Energy at the CERN anti-p p Collider". *Phys. Lett.* B122 (1983), 476.

[28] UA1 Collaboration, G. Arnison, et al. "Experimental Observation of Isolated Large Transverse Energy Electrons with Associated Missing Energy at $\sqrt{s} = 540$ GeV". *Phys. Lett.* B122 (1983). [611(1983)], 103.

[29] UA1 Collaboration, G. Arnison, et al. "Experimental Observation of Lepton Pairs of Invariant Mass Around 95-GeV/c^2 at the CERN SPS Collider". *Phys. Lett.* B126 (1983), 398.

[30] UA2 Collaboration, P. Bagnaia, et al. "Evidence for $Z^0 \to e^+e^-$ at the CERN anti-p p Collider". *Phys. Lett.* B129 (1983), 130.

[31] F. Englert and R. Brout. "Broken Symmetry and the Mass of Gauge Vector Mesons". *Phys. Rev. Lett.* 13 (1964), 321.

[32] P. W. Higgs. "Broken Symmetries and the Masses of Gauge Bosons". *Phys. Rev. Lett.* 13 (1964), 508.

[33] G. S. Guralnik, C. R. Hagen, and T. W. B. Kibble. "Global Conservation Laws and Massless Particles". *Phys. Rev. Lett.* 13 (1964), 585.

[34] P. Z. Quintas et al. "A Measurement of $\Lambda_{\overline{MS}}$ from ν_μ - Fe Nonsinglet Structure Functions at the Fermilab Tevatron". *Phys. Rev. Lett.* 71 (1993), 1307.

[35] R. Adam et al. "Planck 2015 results. I. Overview of products and scientific results". *Astron. Astrophys.* 594 (2016), A1.

[36] S. M. Carroll. "The Cosmological constant". *Living Rev. Rel.* 4 (2001), 1.

[37] B. Pontecorvo. "Mesonium and anti-mesonium". *Sov. Phys. JETP* 6 (1957), 429.

[38] S. P. Martin. "A Supersymmetry primer". *Adv. Ser. Direct. High Energy Phys.18,1* (1997).

[39] J. C. Collins, D. E. Soper, and G. F. Sterman. "Factorization of Hard Processes in QCD". *Adv. Ser. Direct. High Energy Phys.* 5 (1989), 1.

[40] G. Altarelli and G. Parisi. "Asymptotic Freedom in Parton Language". *Nucl. Phys.* B126 (1977), 298.

[41] Y. L. Dokshitzer. "Calculation of the Structure Functions for Deep Inelastic Scattering and e+ e- Annihilation by Perturbation Theory in Quantum Chromodynamics." *Sov. Phys. JETP* 46 (1977). [Zh. Eksp. Teor. Fiz.73,1216(1977)], 641.

[42] V. N. Gribov and L. N. Lipatov. "Deep inelastic e p scattering in perturbation theory". *Sov. J. Nucl. Phys.* 15 (1972). [Yad. Fiz.15,781(1972)], 438.

[43] J. Gao et al. "CT10 next-to-next-to-leading order global analysis of QCD". *Phys. Rev.* D89.3 (2014), 033009.

[44] M. Cacciari et al. "Top-pair production at hadron colliders with next-to-next-to-leading logarithmic soft-gluon resummation". *Phys. Lett.* B710 (2012), 612.

[45] P. Bärnreuther, M. Czakon, and A. Mitov. "Percent Level Precision Physics at the Tevatron: First Genuine NNLO QCD Corrections to $q\bar{q} \to t\bar{t} + X$". *Phys. Rev. Lett.* 109 (2012), 132001.

[46] M. Czakon and A. Mitov. "NNLO corrections to top-pair production at hadron colliders: the all-fermionic scattering channels". *JHEP* 1212 (2012), 054.

[47] M. Czakon and A. Mitov. "NNLO corrections to top-pair production at hadron colliders: the quark-gluon reaction". *JHEP* 1301 (2013), 080.

[48] M. Czakon, P. Fiedler, and A. Mitov. "The total top quark pair production cross-section at hadron colliders through $\mathcal{O}(\alpha_S^4)$". *PRL* 110 (2013), 252004.

[49] M. Czakon and A. Mitov. "Top++: a program for the calculation of the top-pair cross-section at hadron colliders" (2011). arXiv: 1112.5675 [hep-ph].

[50] A. D. Martin et al. "Parton distributions for the LHC". *Eur. Phys. J.* C63 (2009), 189.

[51] A. D. Martin et al. "Uncertainties on alpha(S) in global PDF analyses and implications for predicted hadronic cross sections". *Eur. Phys. J.* C64 (2009), 653.

[52] R. D. Ball et al. "Parton distributions with LHC data". *Nucl. Phys.* B867 (2013), 244.

[53] ATLAS and CMS Collaborations. *Combination of ATLAS and CMS top quark pair cross section measurements in the eμ final state using proton-proton collisions at* $\sqrt{s}$*= 8 TeV*. Tech. rep. ATLAS-CONF-2014-054.

[54] Tait, M. P. Timothy, and C. P. Yuan. "Single top quark production as a window to physics beyond the standard model". *Phys. Rev.* D63 (2000), 014018.

[55] J. M. Campbell and R. K. Ellis. "MCFM for the Tevatron and the LHC". *Nucl. Phys. Proc. Suppl.* 205-206 (2010), 10–15.

[56] C. Patrignani et al. "Review of Particle Physics". *Chin. Phys.* C40.10 (2016), 100001.

[57] J. A. Aguilar-Saavedra and J. Bernabeu. "W polarisation beyond helicity fractions in top quark decays". *Nucl. Phys.* B840 (2010), 349.

[58] J. A. Aguilar-Saavedra. "A Minimal set of top anomalous couplings". *Nucl. Phys.* B812 (2009), 181.

[59] W. Bernreuther, P. Gonzalez, and M. Wiebusch. "The Top Quark Decay Vertex in Standard Model Extensions". *Eur. Phys. J.* C60 (2009), 197.

[60] J.-j. Cao et al. "Supersymmetric effects in top quark decay into polarized W boson". *Phys. Rev.* D68 (2003), 054019.

[61] J. F. Gunion et al. "The Higgs Hunter's Guide". *Front. Phys.* 80 (2000).

[62] S. M. Etesami, M. Khatiri Yanehsari, and M. Mohammadi Najafabadi. "The effects of standard model extensions on W-boson helicity ratios in top quark decay". *Int. J. Theor. Phys.* 51 (2012), 3694.

[63] C. T. Hill. "Topcolor assisted technicolor". *Phys. Lett.* B345 (1995), 483.

[64] K. D. Lane and E. Eichten. "Natural topcolor assisted technicolor". *Phys. Lett.* B352 (1995), 382.

[65] J. A. Aguilar-Saavedra et al. "Probing anomalous Wtb couplings in top pair decays". *Eur. Phys. J.* C50 (2007), 519.

[66] F. del Aguila and J. A. Aguilar-Saavedra. "Precise determination of the Wtb couplings at CERN LHC". *Phys. Rev.* D67 (2003), 014009.

[67] ATLAS and CMS Collaborations. *Combination of the ATLAS and CMS measurements of the W-boson polarization in top-quark decays.* ATLAS-CONF-2013-033.

[68] T. Aaltonen et al. "Combination of CDF and D0 measurements of the W boson helicity in top quark decays". *Phys. Rev.* D85 (2012), 071106.

[69] L. Evans and P. Bryant. "LHC Machine". *JINST* 3 (2008), S08001.

[70] K. Aamodt et al. "The ALICE experiment at the CERN LHC". *JINST* 3 (2008), S08002.

[71] ATLAS Collaboration. "The ATLAS Experiment at the CERN Large Hadron Collider". *JINST* 3 (2008), S08003.

[72] CMS Collaboration. "The CMS experiment at the CERN LHC". *JINST* 3 (2008), S08004.

[73] A. A. Alves Jr. et al. "The LHCb Detector at the LHC". *JINST* 3 (2008), S08005.

[74] LHCf Collaboration, O. Adriani, et al. "The LHCf detector at the CERN Large Hadron Collider". *JINST* 3 (2008), S08006.

[75] MoEDAL Collaboration, J. Pinfold, et al. *Technical Design Report of the MoEDAL Experiment*. CERN-LHCC-2009-006.

[76] TOTEM Collaboration, V. Berardi, et al. *TOTEM: Technical design report. Total cross section, elastic scattering and diffraction dissociation at the Large Hadron Collider at CERN*. CERN-LHCC-2004-002.

[77] C. Lefevre. *LHC: the guide (English version). Guide du LHC (version anglaise)*. Feb. 2009. https://cds.cern.ch/record/1165534.

[78] M. Capeans et al. *ATLAS Insertable B-Layer Technical Design Report*. CERN-LHCC-2010-013.

[79] ATLAS Collaboration. *ATLAS tile calorimeter: Technical design report*. CERN-LHCC-96-42.

[80] A. Collaboration. *ATLAS: Detector and physics performance technical design report. Volume 1*. CERN-LHCC-99-14.

[81] ATLAS Collaboration. "Luminosity determination in pp collisions at $\sqrt{s} = 8$ TeV using the ATLAS detector at the LHC". *Eur. Phys. J.* C76.12 (2016), 653.

[82] ATLAS Collaboration. *Luminosity Public Results*. https://twiki.cern.ch/twiki/bin/view/AtlasPublic/LuminosityPublicResults (visited on 02/26/2017).

[83] ATLAS Collaboration. "Luminosity determination in pp collisions at $\sqrt{s} = 7$ TeV using the ATLAS detector at the LHC". *Eur. Phys. J. C* 71 (2011), 1630.

[84] ATLAS Collaboration. *ATLAS Run 1 Detector Status*. https://twiki.cern.ch/twiki/bin/view/AtlasPublic/ApprovedPlotsATLASDetector (visited on 02/26/2017).

[85] B. Lemmer. "Measurement of Spin Correlations in $t\bar{t}$ Events from pp Collisions at $\sqrt{s} = 7$ TeV in the Lepton + Jets Final State with the ATLAS Detector". PhD thesis. II.PHYSIK-UNIGÖ-DISS-2014-02. arXiv: 1410.1791 [hep-ex].

[86] ATLAS Collaboration. *ATLAS Public Event Displays*. https://twiki.cern.ch/twiki/bin/view/AtlasPublic/EventDisplayPapers (visited on 02/26/2017).

[87] ATLAS Collaboration. *Performance of the ATLAS Silicon Pattern Recognition Algorithm in Data and Simulation at $\sqrt{s} = 7$ TeV*. ATLAS-CONF-2010-072.

[88] ATLAS Collaboration. *Performance of the ATLAS Inner Detector Track and Vertex Reconstruction in High Pile-Up LHC Environment*. ATLAS-CONF-2012-042.

[89] ATLAS Collaboration. *Data-driven background estimation for the $H \to \tau^+\tau^- \to \ell\tau_h$ search at $\sqrt{s} = 7$ TeV with the ATLAS detector*. ATLAS-CONF-2010-096.

[90] ATLAS Collaboration. "Electron performance measurements with the ATLAS detector using the 2010 LHC proton–proton collision data". *Eur. Phys. J. C* 72 (2012), 1909.

[91] ATLAS Collaboration. *Electron efficiency measurements with the ATLAS detector using the 2012 LHC proton–proton collision data*. ATLAS-CONF-2014-032.

[92] ATLAS Collaboration. "Electron and photon energy calibration with the ATLAS detector using LHC Run 1 data". *Eur. Phys. J. C* 74 (2014), 3071.

[93] ATLAS Collaboration. "Measurement of the muon reconstruction performance of the ATLAS detector using 2011 and 2012 LHC proton–proton collision data". *Eur. Phys. J. C* 74 (2014), 3130.

[94] K. Rehermann and B. Tweedie. "Efficient Identification of Boosted Semileptonic Top Quarks at the LHC". *JHEP* 03 (2011), 059.

[95] ATLAS Collaboration. "Hadronic calibration of the ATLAS liquid argon end-cap calorimeter in the pseudorapidity region $1.6 < |\eta| < 1.8$ in beam tests". *Nucl. Instrum. Meth.* A531 (2004), 481.

[96] ATLAS Collaboration. *Local Hadronic Calibration*. ATL-LARG-PUB-2009-001-2.

[97] M. Cacciari, G. P. Salam, and G. Soyez. "The Anti-k(t) jet clustering algorithm". *JHEP* 04 (2008), 063.

[98] M. Cacciari and G. P. Salam. "Dispelling the N^3 myth for the k_t jet-finder". *Phys. Lett.* B641 (2006), 57.

[99] M. Cacciari, G. P. Salam, and G. Soyez. "FastJet User Manual". *Eur. Phys. J.* C72 (2012), 1896.

[100] G. P. Salam. "Towards Jetography". *Eur. Phys. J.* C67 (2010), 637.

[101] ATLAS Collaboration. *Monte Carlo Calibration and Combination of In-situ Measurements of Jet Energy Scale, Jet Energy Resolution and Jet Mass in ATLAS*. ATLAS-CONF-2015-037.

[102] ATLAS Collaboration. *Determination of the jet energy scale and resolution at ATLAS using Z/γ-jet events in data at $\sqrt{s} = 8$ TeV*. ATLAS-CONF-2015-057.

[103] ATLAS Collaboration. "Performance of b-Jet Identification in the ATLAS Experiment". *JINST* 11 (2016), P04008.

[104] ATLAS Collaboration. *Calibration of b-tagging using dileptonic top pair events in a combinatorial likelihood approach with the ATLAS experiment.* ATLAS-CONF-2014-004.

[105] ATLAS Collaboration. *Pile-up subtraction and suppression for jets in ATLAS.* ATLAS-CONF-2013-083.

[106] ATLAS Collaboration. *Commissioning of the ATLAS high performance b-tagging algorithms in the 7 TeV collision data.* ATLAS-CONF-2011-102.

[107] ATLAS Collaboration. *Measurement of the b-tag Efficiency in a Sample of Jets Containing Muons with 5 fb^{-1} of data from the ATLAS detector.* ATLAS-CONF-2012-043.

[108] ATLAS Collaboration. *b-jet tagging calibration on c-jets containing D^{*+} mesons.* ATLAS-CONF-2012-039.

[109] ATLAS Collaboration. *Measurement of the Mistag Rate of b-tagging algorithms with 5 fb^{-1} of Data Collected by the ATLAS Detector.* ATLAS-CONF-2012-040.

[110] ATLAS Collaboration. *Performance of Missing Transverse Momentum Reconstruction in ATLAS studied in Proton–Proton Collisions recorded in 2012 at $\sqrt{s} = 8$ TeV.* ATLAS-CONF-2013-082.

[111] ATLAS Collaboration. *Reconstruction and Calibration of Missing Transverse Energy and Performance in Z and W events in ATLAS Proton–Proton Collisions at $\sqrt{s} = 7$ TeV.* ATLAS-CONF-2011-080.

[112] P. Nason. "A New method for combining NLO QCD with shower Monte Carlo algorithms". *JHEP* 11 (2004), 040.

[113] S. Frixione, P. Nason, and C. Oleari. "Matching NLO QCD computations with Parton Shower simulations: the POWHEG method". *JHEP* 11 (2007), 070.

[114] S. Alioli et al. "A general framework for implementing NLO calculations in shower Monte Carlo programs: the POWHEG BOX". *JHEP* 06 (2010), 043.

[115] T. Gleisberg et al. "Event generation with SHERPA 1.1". *JHEP* 02 (2009), 007.

[116] T. Sjostrand, S. Mrenna, and P. Z. Skands. "PYTHIA 6.4 Physics and Manual". *JHEP* 05 (2006), 026.

[117] G. Corcella et al. "HERWIG 6: An Event generator for hadron emission reactions with interfering gluons (including supersymmetric processes)". *JHEP* 01 (2001), 010.

[118] X. Artru and G. Mennessier. "String model and multiproduction". *Nucl. Phys.* B70 (1974), 93.

[119] S. Agostinelli et al. "GEANT4: A Simulation toolkit". *Nucl. Instrum. Meth.* A506 (2003), 250.

[120] A. Corso-Radu et al. "Data quality monitoring framework for the ATLAS experiment: Performance achieved with colliding beams at the LHC". *J. Phys. Conf. Ser.* 331 (2011), 022027.

[121] A. Corso-Radu et al. *Data Quality Monitoring Framework for the ATLAS Experiment at the LHC*.

[122] H.-L. Lai et al. "New parton distributions for collider physics". *Phys. Rev.* D82 (2010), 074024.

[123] J. Pumplin et al. "New generation of parton distributions with uncertainties from global QCD analysis". *JHEP* 07 (2002), 012.

[124] P. Z. Skands. "Tuning Monte Carlo Generators: The Perugia Tunes". *Phys. Rev.* D82 (2010), 074018.

[125] M. L. Mangano et al. "ALPGEN, a generator for hard multiparton processes in hadronic collisions". 07 (2003), 001.

[126] M. L. Mangano et al. "Multijet matrix elements and shower evolution in hadronic collisions: $Wb\bar{b} + n$ jets as a case study". B 632 (2002), 343.

[127] K. Melnikov and F. Petriello. "Electroweak gauge boson production at hadron colliders through $\mathcal{O}(\alpha_s^2)$". 74 (2006), 114017.

[128] S. Alioli et al. "NLO single-top production matched with shower in POWHEG: s- and t-channel contributions". *JHEP* 09 (2009), 111. [Erratum: JHEP 02 (2010) 011].

[129] E. Re. "Single-top Wt-channel production matched with parton showers using the POWHEG method". *Eur. Phys. J.* C71 (2011), 1547.

[130] S. Frixione et al. "Single-top hadroproduction in association with a W boson". *JHEP* 07 (2008), 029.

[131] N. Kidonakis. "Next-to-next-to-leading-order collinear and soft gluon corrections for t-channel single top quark production". *Phys. Rev.* D83 (2011), 091503.

[132] N. Kidonakis. "NNLL resummation for s-channel single top quark production". *Phys. Rev.* D81 (2010), 054028.

[133] N. Kidonakis. "Two-loop soft anomalous dimensions for single top quark associated production with a W- or H-". *Phys. Rev.* D82 (2010), 054018.

[134] A. D. Martin et al. "Parton distributions for the LHC". *Eur. Phys. J.* C63 (2009), 189.

[135] A. D. Martin et al. "Uncertainties on alpha(S) in global PDF analyses and implications for predicted hadronic cross sections". *Eur. Phys. J.* C64 (2009), 653.

[136] ATLAS Collaboration. "Measurement of the top quark mass in the $t\bar{t} \to$ dilepton channel from $\sqrt{s} = 8$ TeV ATLAS data". *Phys. Lett. B* 761 (2016), 350.

[137] J. Campbell and R. Ellis. "An update on vector boson pair production at hadron colliders". *PRD* 60 (1999), 113006.

[138] P. Nason. "A New method for combining NLO QCD with shower Monte Carlo algorithms." *JHEP* 11 (2004), 040.

[139] P. N. S. Frixione and C. Oleari. "Matching NLO QCD computations with Parton Shower simulations: the POWHEG method." *JHEP* 11 (2007), 070.

[140] ATLAS Collaboration. "Measurement of the charge asymmetry in top-quark pair production in the lepton-plus-jets final state in pp collision data at $\sqrt{s} = 8$ TeV with the ATLAS detector". *Eur. Phys. J. C* 76 (2016), 87.

[141] K. Melnikov and F. Petriello. "Electroweak gauge boson production at hadron colliders through $O(\alpha_s^2)$". *Phys. Rev. D.* 74 (2006), 114017.

[142] N. Kidonakis. "Next-to-next-to-leading-order collinear and soft gluon corrections for t-channel single top quark production". *Phys. Rev. D.* 83 (2011), 091503.

[143] N. Kidonakis. "Two-loop soft anomalous dimensions for single top quark associated production with a W^- or H^-". *Phys. Rev. D.* 82 (2010), 054018.

[144] N. Kidonakis. "NNLL resummation for s-channel single top quark production". *Phys. Rev. D.* 81 (2010), 054028.

[145] J. Campbell and R. Ellis. "An update on vector boson pair production at hadron colliders". *Phys. Rev. D.* 60 (1999), 113006.

[146] ATLAS Collaboration. *Estimation of non-prompt and fake lepton backgrounds in final states with top quarks produced in proton–proton collisions at* $\sqrt{s} = 8$ *TeV with the ATLAS Detector.* ATLAS-CONF-2014-058.

[147] ATLAS Collaboration. *Selection of jets produced in proton–proton collisions with the ATLAS detector using 2011 data.* ATLAS-CONF-2012-020.

[148] J. Erdmann et al. "A likelihood-based reconstruction algorithm for top-quark pairs and the KLFitter framework". *Nucl. Instrum. Meth.* A748 (2014), 18.

[149] A. Caldwell, D. Kollar, and K. Kroninger. "BAT: The Bayesian Analysis Toolkit". *Comput. Phys. Commun.* 180 (2009), 2197.

[150] S. Frixione and B. R. Webber. "Matching NLO QCD computations and parton shower simulations". *JHEP* 06 (2002), 029.

[151] S. Frixione, P. Nason, and B. R. Webber. "Matching NLO QCD and parton showers in heavy flavor production". *JHEP* 08 (2003), 007.

[152] ATLAS Collaboration. "Performance of missing transverse momentum reconstruction in proton–proton collisions at $\sqrt{s} = 7$ TeV with ATLAS". *Eur. Phys. J. C* 72 (2012), 1844.

[153] ATLAS Collaboration. "Measurements of spin correlation in top–antitop quark events from proton–proton collisions at $\sqrt{s} = 7$ TeV using the ATLAS detector". *Phys. Rev. D* 90 (2014), 112016.

[154] ATLAS Collaboration. "Measurement of the W boson polarisation in $t\bar{t}$ events from pp collisions at $\sqrt{s} = 8$ TeV in the lepton+jets channel with ATLAS" (2016). arXiv: 1612.02577 [hep-ex]. Submitted to EPJ C.

[155] J. Friedman. "Data analysis techniques for high energy particle physics". *Proc.of the 1974 CERN School of Computing* (1974).

[156] L. Chakravarti and Roy. "Handbook of Methods of Applied Statistics". *John Wiley and Sons* I (1967), 392.

[157] F. James and M. Roos. "Minuit: A System for Function Minimization and Analysis of the Parameter Errors and Correlations". *Comput. Phys. Commun.* 10 (1975), 343.

[158] R. Brun and F. Rademakers. "ROOT: An object oriented data analysis framework". *Nucl. Instrum. Meth.* A389 (1997), 81.

[159] ATLAS Collaboration. "Electron reconstruction and identification efficiency measurements with the ATLAS detector using the 2011 LHC proton–proton collision data". *Eur. Phys. J. C* 74 (2014), 2941.

[160] ATLAS Collaboration. "Muon reconstruction efficiency and momentum resolution of the ATLAS experiment in proton–proton collisions at $\sqrt{s} = 7$ TeV in 2010". *Eur. Phys. J. C* 74 (2014), 3034.

[161] ATLAS Collaboration. "Jet energy measurement with the ATLAS detector in proton–proton collisions at $\sqrt{s} = 7$ TeV". *Eur. Phys. J. C* 73 (2013), 2304.

[162] ATLAS Collaboration. "Performance of pile-up mitigation techniques for jets in *pp* collisions with the ATLAS detector" (2015). arXiv: 1510.03823 [hep-ex].

[163] ATLAS Collaboration. *In-situ jet energy scale and jet shape corrections for multiple interactions in the first ATLAS data at the LHC.* ATLAS-CONF-2011-030.

[164] ATLAS Collaboration. *In-situ pseudorapidity intercalibration for evaluation of jet energy scale uncertainty using dijet events in proton–proton collisions at* $\sqrt{s} = 7$ *TeV.* ATLAS-CONF-2011-014.

[165] ATLAS Collaboration. *Jet Energy Resolution and Selection Efficiency Relative to Track Jets from In-situ Techniques with the ATLAS Detector Using Proton–Proton Collisions at a Center of Mass Energy* $\sqrt{s} = 7$ *TeV.* ATLAS-CONF-2010-054.

[166] ATLAS Collaboration. *In-situ pseudorapidity intercalibration to evaluate jet energy scale uncertainty and calorimeter performance in the forward region.* ATLAS-CONF-2010-055.

[167] ATLAS Collaboration. *JES Uncertainty – Public Results.* https://twiki.cern.ch/twiki/bin/view/AtlasPublic/JetEtmissApproved2013JESUncertainty (visited on 02/26/2017).

[168] S. Frixione et al. "Single-top hadroproduction in association with a W boson". *JHEP* 07 (2008), 029.

[169] J. A. Aguilar-Saavedra. "Single top quark production at LHC with anomalous Wtb couplings". *Nucl. Phys.* B804 (2008), 160.

[170] M. Botje et al. "The PDF4LHC Working Group Interim Recommendations" (2011). arXiv: 1101.0538 [hep-ph].

[171] M. R. Whalley, D. Bourilkov, and R. C. Group. "The Les Houches accord PDFs (LHAPDF) and LHAGLUE". *HERA and the LHC: A Workshop on the implications of HERA for LHC physics. Proceedings, Part B.* 2005, 575. arXiv: hep-ph/0508110 [hep-ph].

[172] C. Zhang and S. Willenbrock. "Effective-Field-Theory Approach to Top-Quark Production and Decay". *Phys. Rev.* D83 (2011), 034006.

[173] W. Buchmüller and D. Wyler. "Effective Lagrangian Analysis of New Interactions and Flavor Conservation". *Nucl. Phys.* B268 (1986), 621.

[174] F. Bach and T. Ohl. "Anomalous Top Couplings at Hadron Colliders Revisited". *Phys. Rev.* D86 (2012), 114026.

[175] N. Castro et al. "EFTfitter—A tool for interpreting measurements in the context of effective field theories". *Eur. Phys. J.* C76.8 (2016), 432.

[176] ATLAS Collaboration. "Search for anomalous couplings in the Wtb vertex from the measurement of double differential angular decay rates of single top quarks produced in the t-channel with the ATLAS detector". *JHEP* 04 (2016), 023.

[177] CMS Collaboration, V. Khachatryan, et al. "Measurement of the t-channel single-top-quark production cross section and of the $| V_{tb} |$ CKM matrix element in pp collisions at $\sqrt{s}$= 8 TeV". *JHEP* 06 (2014), 090.

[178] ATLAS Collaboration. "Comprehensive measurements of t-channel single top-quark production cross sections at $\sqrt{s} = 7$ TeV with the ATLAS detector". *Phys. Rev. D* 90 (2014), 112006.

[179] B. Grzadkowski and M. Misiak. "Anomalous Wtb coupling effects in the weak radiative B-meson decay". *Phys. Rev.* D78 (2008), 077501.

[180] ATLAS Collaboration. *Top Public Results*. https://atlas.web.cern.ch/Atlas/GROUPS/PHYSICS/CombinedSummaryPlots/TOP (visited on 02/26/2017).

[181] R. D. Field and R. P. Feynman. "A Parametrization of the Properties of Quark Jets". *Nucl. Phys.* B136 (1978), 1.

[182] M. Mjahed. "Identification of the quark jet charge in $e^+e^- \to W^+W^-$ using neural networks and discriminant analysis methods". *Nucl. Instrum. Meth.* A449 (2000), 602.

[183] ATLAS Collaboration. "Measurement of the top quark charge in pp collisions at $\sqrt{s} = 7$ TeV with the ATLAS detector". *JHEP* 11 (2013), 031.

[184] CMS Collaboration. *Constraints on the Top-Quark Charge from Top-Pair Events*. CMS-PAS-TOP-11-031. 2012.

List of Abbreviations

BSM Beyond Standard Model

CERN Conseil Européen pour la Recherche Nucléaire

DB Direct Balance

ECal Electromagnetic Calorimeter

EM Electro-Magnetic

HCal Hadronic Calorimeter

ID Inner Detector

LAr Liquid-Argon

LHC Large Hadron Collider

LO Leading Order

MC Monte Carlo

MPF Missing Projection Fraction

MSSM Minimal Supersymmetric Standard Model

MS Muon Spectrometer

NLO Next-to-Leading-Order

NNLL Next-to-Next-to-Leading-Logarithmic

NNLO Next-to-Next-to-Leading-Order

PDF Parton Distribution Functions

PSB Proton-Synchrotron Booster

PS Proton-Syncrotron

QCD Quantum Chromodynamics

QED Quantum Electrodynamics

QFT Quantum Field Theory

SCT Semi-Conductor Tracker

SM Standard Model

SPS Super-Proton-Syncrotron

SUSY Supersymmetry

TDAQ Trigger and Data Acquisition

TRT Transition Radiation Tracker

List of Figures

List of Tables